Strål säkerhets myndigheten
Swedish Radiation Safety Authority

Author: A. R. Massih
Quantum Technologies AB

Research

2018:25

UO2 fuel oxidation and fission gas release

Report number: 2018:25 ISSN: 2000-0456
Available at www.stralsakerhetsmyndigheten.se

SSM perspective

Background

The Swedish Radiation Safety Authority (SSM) follows the research on fuel performance closely. One aspect that has been the main question of several research projects is the fragmentation of fuel pellets during abnormal heat up. In this project the oxidation of UO2 is scrutinized and its effect on pellet fragmentation, fission gas release and damage of fuel rods has been investigated.

Many phenomena that affect a fuel rod are described mathematically in analysis tools (computer codes) like FRAPCON and FRAPTRAN, but fuel oxidation is not commonly included in such tools. Current analysis tools usually have an empirical description of the state of fuel pellets where the oxidation of UO2 would be a part of a rough model of porosity and heat transfer of the pellet. Better descriptions of essential phenomena in fuel analysis tools will lead to more accurate analysis of fuel behaviour.

Objective

Knowledge of what is happening in a fuel rod during an event and how it is implemented in analytical tools is essential to SSM for our supervision of nuclear power plants. This project has contributed to the development of knowledge at SSM regarding the phenomena of fuel oxidation and how it affects the risks and consequences of fuel damage. It is has also provided an insight into how phenomena like fuel oxidation can be included in analysis tools.

Results

In this project the understanding of how to describe fuel oxidation during normal and abnormal conditions has been investigated. Starting from current knowledge of fuel oxidation a model has been suggested that can be implemented in FRAPTRAN for further analysis of fuel behaviour. In this project, which includes a first evaluation of the model, the results indicate that fuel oxidation has a large impact on fission gas release.

Need for further research

What happens in high burn-up fuel during a heat up transient is a complex situation with several effects acting simultaneously; for example temperature, pressure, material structure and available isotopes. The state of fuel is not sufficiently known today and research is ongoing with tests of separate effects and integral tests of fuel rod segments. Alongside the tests development of models for simulations and analysis of fuel behaviour is also being pursued. With respect to fuel oxidation the next step is to implement the suggested model and verify it in comparison with the tests.

Project information

Contact person SSM: Sanna Rejnlander
Reference: SSM2016-3944 / 7030147-00

Strål
säkerhets
myndigheten
Swedish Radiation Safety Authority

Author: A. R. Massih
Quantum Technologies AB

2018:25

UO2 fuel oxidation and fission gas release

Date: January 2018
Report number: 2018:25 **ISSN:** 2000-0456
Available at www.stralsakerhetsmyndigheten.se

This report concerns a study which has been conducted for the Swedish Radiation Safety Authority, SSM. The conclusions and viewpoints presented in the report are those of the author/authors and do not necessarily coincide with those of the SSM.

UO_2 fuel oxidation and fission gas release

A. R. Massih

12 November 2018

Quantum Technologies AB
Uppsala Science Park
SE-751 83 Uppsala, Sweden

UO_2 fuel oxidation and fission gas release

A. R. Massih

Quantum Technologies AB
Uppsala Science Park
SE-751 83 Uppsala, Sweden

Quantum Technologies Report: TR17-004v4
Project # - SSM2016-3944

Abstract

Oxidation of UO_2 fuel under off-normal and normal reactor conditions occurs when fuel cladding fails, thereby letting steam/water to enter the fuel rod. The steam/water will react with the fuel to produce UO_{2+x} releasing hydrogen. In this report, oxidation of UO_2 fuel and its consequence to fuel behavior especially fission product gas migration and release in and from the fuel are discussed. Existing experimental data and models in the literature are selectively assessed. We also discuss the applicability of the data and models to light water reactors under both off-normal and normal conditions. Moreover, oxygen redistribution in UO_{2+x} fuel pellet, where a temperature gradient prevails, is modeled. This effect (Soret effect) is also relevant during normal operation for intact fuel rods, where a positive shift to hyperstoichiometry may occur in UO_2.

Contents

1 Introduction

During a hypothetical water-cooled reactor accident, for example due to a loss of reactor coolant, upon the breach of fuel cladding, steam rapidly enters the fuel rod via the opening. The steam replaces the existing gases or may mix with the gases in the free volume of the rod. It reacts with the UO_2 fuel and hence oxidize it, while releasing hydrogen into the free volume of the rod. As a result, the fuel stoichiometry will increase (from UO_2 to UO_{2+x}), changing its thermal and material properties. The crystal structure of UO_2 remains cubic on oxidation with a reduction in the space group symmetry from $Fm\bar{3}m$ (UO_2) to $I\bar{4}3d$ (U_4O_9) and with an increase in the size of unit cell to 21.8 Å for U_4O_9, which is about four times the cell size of UO_2. Further oxidation leads to the orthorhombic α-U_3O_8 but at high temperatures it is described by a simpler hexagonal unit cell with the space group symmetry $P\bar{6}2m$ and unit cell sizes $a = 6.72$ Å , $b = 11.96$ Å and $c = 4.15$ Å [1, 2, 3, 4].[1]
At the same time, the oxidation reaction between steam and the zirconium alloy cladding produces hydrogen in the fuel-cladding gap. Hydrogen production may be drastically enhanced by fission fragment recoil from the fuel into the gap and collisions of the fission fragments with water/steam molecules (radiolysis). The steam molecules are decomposed into H_2 and oxidizing species, such as H_2O_2 or O_2 [6, 7]. The radiolysis brings in more hydrogen into the gap, and thereby increases the hydrogen uptake of the cladding. Moreover, the oxidizing radiolysis products can enhance fuel oxidation, increasing fission product release from the hyperstoichiometric UO_{2+x} while generating even more hydrogen.
In a defective fuel rod, the steam-hydrogen mixture fills in not only the gap volume, but also penetrates the fuel pellet cracks. The cracks are produced during normal operation by thermal stresses, which are generated by the radial temperature gradient in the pellet. They provide a communication channel between the colder periphery of the pellet and the hot center. Figure 1(a) schematically depicts the transport processes in a cross-section of a fuel rod and Fig. 1(b) illustrates the interacting chemical processes and the sources of hydrogen in a defective fuel rod.
It has been understood that at sufficiently high ratios of hydrogen to steam in the gap, hydrogen will either break down or cross the thin oxide (ZrO_2) layer on the cladding wall, reacting rapidly with zirconium forming zirconium hydride [8]. Excessive hydriding of the cladding can lead to extensive secondary failure, either in the form of long axial splits or circumferential breaks [9]. Additionally, opening of a sufficiently long axial crack admits large amount of steam straight into the rod and may lead to wash out of UO_2 fuel fragments from the rod into the already disrupted coolant.
In a loss-of-coolant accident (LOCA) when the reactor is tripped or shut down due to voiding of the coolant, the fuel average temperature may rapidly rise up to about 1600 K (from about 900 - 1000 K) enhancing the mobility of fission products, in particular gases xenon and krypton together with fluid cesium, in the fuel lattice [10]. In addition, experiments have shown substantial releases of fission gases and other volatile fission products, when UO_2 fuel is oxidized to U_3O_8 above 1000 K [11].
Having said that, knowledge of the oxidation of uranium dioxide is very important for light water reactor (LWR) fuel safety assessments. In this report, we review the experimental work that has been carried out in this area and summarize the course of current models that appertains to this process. Methods for computing three interacting developments, namely, fuel oxidation kinetics, fuel heat conduction (temperature) and fission gas

[1] Space group notation is explained, *e.g.* in [5], or online in `Wikepedia` *List of space groups*.

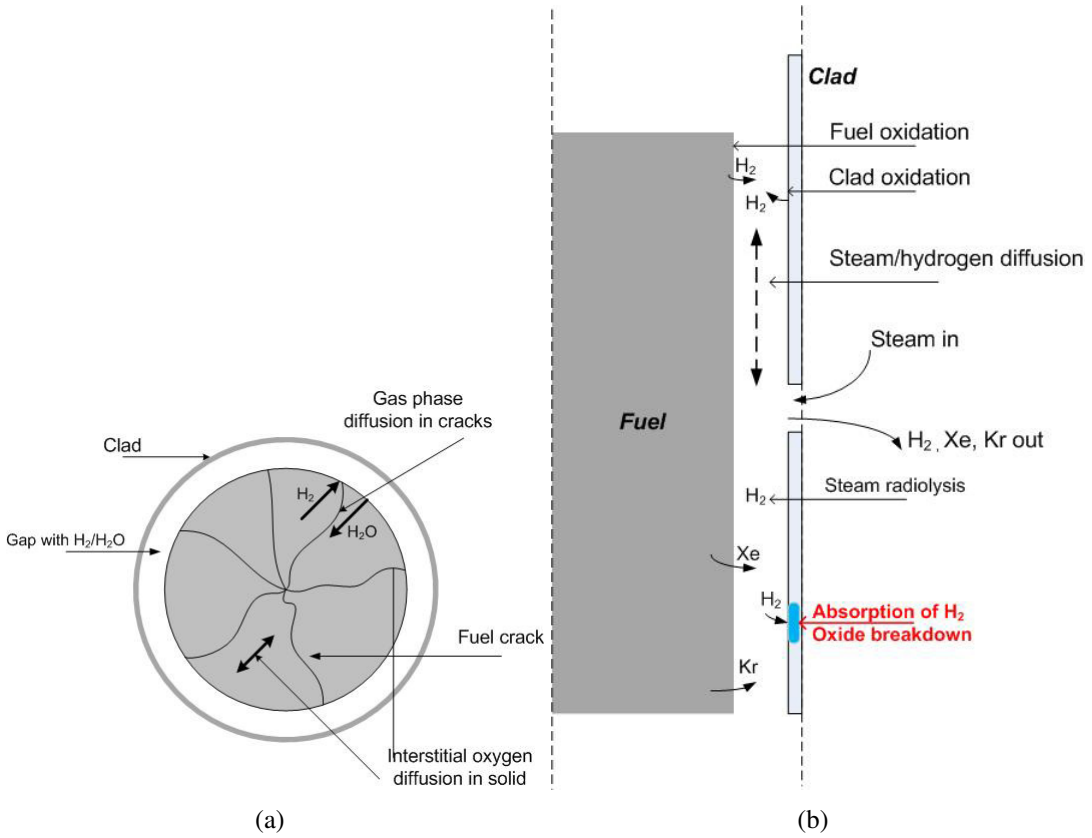

Figure 1: A schematic view of various phenomena in a failed fuel rod.

release from fuel, Fig. 2, are discussed in detail; the latter under annealing and quenching relevant to LOCA conditions. We assess the models to identify the suitable ones for further improvement and implementation in the fuel performance computer program package FRAPCON/FRAPTRAN-QT [12]. Furthermore, the topics covered in this report are also relevant for assessments of UO_2 fuel during spent fuel pool accidents [13].

The remainder of this report will proceed as follows. In Sec. 2, we will survey both experimental and theoretical studies of fuel oxidation. In addition, some comparisons between model calculations and measured data will be made. Oxygen thermal diffusion in UO_{2+x} fuel pellet, where a temperature gradient prevails will be discussed in Sec. 3. This effect (the so called Soret effect) is also relevant during normal operation, where a positive shift to hyperstoichiometry (x) can occur in UO_2. Here, solution methods to oxygen thermodiffusion equation are presented and the surplus oxygen (x) across fuel pellet is calculated in steady states and the relaxation times during transients as a function of temperature are evaluated. Section 4 will discuss the effect of fuel oxidation on fission product gas release, through its impact on the fission gas diffusion coefficient. Prototype computations are made to evaluate the impact of x on gas release from UO_{2+x} fuel during a thermal annealing trial. Finally, Sec. 5 will present a summary and conclusions. Appendices provide supporting materials for the main text, namely, methods for computing the oxygen potentials in the fuel and the fuel-cladding gap, a detailed method for evaluating the transient oxygen thermodiffusion equation, and correlations for thermal conductivity of oxidized UO_2.

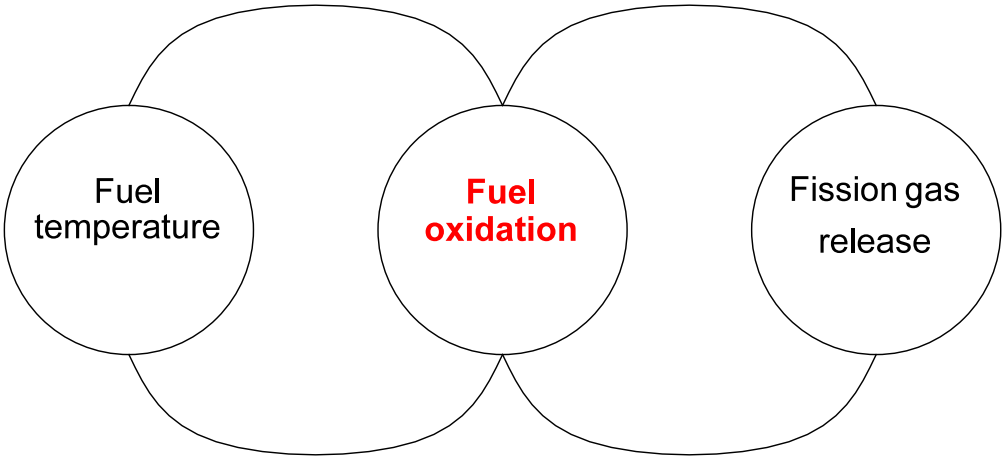

Figure 2: Feedback loop: Fuel oxidation elevates fuel temperature by lowering the thermal conductivity in the heat equation and it increases fission gas release by enhancing the gas diffusion coefficient in the diffusion equation.

2 UO_2 oxidation process

The kinetics of UO_2 oxidation in steam has been primarily investigated at temperatures greater than 1000 K, mainly at 1 atm pressure, with the aim to characterize the severe-accident performance of the fuel [14, 15, 16, 17, 18]. These studies indicated clearly that the oxidation rate is controlled by the surface reaction where water molecules are decomposed to produce oxygen atoms that enter the solid and hydrogen that returns to the gas [14].
In particular, Cox *et al.* [14] showed that the oxidation kinetics could adequately be described by an empirical rate law originally mapped out by Carter and Lay [19] for oxidation of UO_2 in CO/CO_2 environment. Indeed, based on the activation energies of surface reaction (≈ 200 kJ/mol) and oxygen chemical diffusion (≈ 50 kJ/mol), one may anticipate that the solid-state oxygen diffusion controls the kinetics in steam/hydrogen gases only for temperatures greater than 2000 K [20].
Upon cladding failure, steam/water rapidly enters the puncture and replaces the inert gases occupying the free volume of the fuel rod with superheated steam. It causes oxidation of UO_2 fuel with an overall reaction [7]:

$$\mathrm{UO_2} + x\mathrm{H_2O} \rightleftharpoons \mathrm{UO_{2+x}} + x\mathrm{H_2}, \tag{1}$$

which leads to hyperstoichiometric fuel UO_{2+x} and release of hydrogen gas. Fuel oxidation lowers fuel thermal conductivity, enhances fission product gas release and provides an additional source of hydrogen, which would further deteriorate the integrity of cladding through massive hydriding.
Olander and coworkers, however, have argued that steam-hydrogen mixtures are expected to be present in the fuel-cladding gap upon entry prior to fuel oxidation [7]. Moreover, they point out that the much lower oxygen partial pressures in steam-hydrogen mixtures hardly changes UO_2 to UO_{2+x} at moderate fuel temperatures (<1000 K). For example, they note that in steam containing 10 mol% H_2 at about 800 K, the equilibrium stoichiometry deviation amounts to $x_{eq} \approx 1.0 \times 10^{-6}$ which is virtually an undetectable value [21]. However, x_{eq} is a strong function of temperature and also the steam-to-hydrogen ratio, see appendix Sec. A.1. Post-irradiation examination (PIE) of failed fuel rods (during normal operation) has shown that fuel oxidation is more significant than that described by the kinetics and thermodynamic arguments given in [7]. For example, Une *et al.* [16] measurements on defective BWR fuel rods showed that the fuel oxidation highly depends on the defect size and distance from the primary defect. The pellet volume-averaged O/M ratios at various axial locations were in the range of $2.02 - 2.06$ for the irradiated fuel.
In this section, some key experimental studies reported in the literature are reviewed. They are out-of-reactor investigations mainly conducted in atmospheric pressure. The results of these studies form the basis for some of the existing models discussed in the subsequent sections.

2.1 Experimental investigations

2.1.1 Unirradiated fuels

Carter-Lay experiment [19] In an early experiment, Carter and Lay at General Electric (Schenectady, New York) measured the oxidation and reduction rates of UO_2 in CO/CO_2 mixtures between 900 and 1400°C and the O/U ratios of 2.01 and 2.14. They found that the oxidation rates are proportional to the surface-to-volume ratio of the specimens and to

the (CO_2+CO) partial pressure in a (CO_2+CO+inert gas) environment.
The specimens tested comprised polycrystalline uranium dioxide with 15 μm grain size and a relative theoretical density (TD) of 0.97. The specimens where long right square parallelepiped ($2a = 2b \ll 2c$) with thicknesses $2a = 1.62$ mm, 5.46 mm and 5.6 mm. Throughout the experiment, the stoichiometry of the UO_2 was controlled by continuously flowing the appropriate CO/CO_2 mixture over the samples.
The researchers studied the equilibrium stoichiometry as a function of CO/CO_2 gas flow rate and sample size. The electrical resistivity of the samples was measured to examine the extent of oxidation of the samples. Moreover, the half-times of oxidation (the time for 50% oxidation) were determined. For example, at 1200°C, a flow of 200 ml/min and oxidation O/U=2.01 to 2.14, they found that $t_{1/2} = 20$ h.
The Carter-Lay experiment showed that the kinetics of the oxidation reaction may be described by a rate expression of the form

$$\frac{dx}{dt} = \alpha(S/V)[x_{eq} - x], \tag{2}$$

where α is called the surface exchange coefficient (or reaction rate) of oxygen, (S/V) is the surface-to-volume ratio of the fuel specimen and x_{eq} is the equilibrium stoichiometry deviation as governed by the oxygen potential (Gibbs energy) of the O-U system. It is the equilibrium stoichiometry deviation as defined by the oxygen potential of the gas in the surrounding. Eq. (2) can be solved to give

$$x = x_{eq}\Big(1 - \exp[-\alpha(S/V)t]\Big), \tag{3}$$

where it has been assumed that α is time-independent (isothermal) and the fuel is initially stoichiometric $x(0) = 0$. The correlation should be valid for $-0.14 < x < 0.25$.

Chalk River, Canada, experiments Experiments on UO_2 in steam at 1273-1923 K in atmospheric pressure were conducted by the Chalk River Laboratories (CRL) workers Cox *et al.* [14] to determine the rate constant of reaction (surface exchange coefficient). The tests were performed in a furnace using an alumina reaction tube (57 mm diameter) and the steam was produced by flash evaporation of inflowing water by means of a steam generator connected to the furnace. Specimens of UO_2 (cylinders 12.15 mm diameter and 15.6 mm length) were placed in the furnace and were weighed before and after testing. An installed thermocouple monitored the specimen temperature during the test. The steam flow was maintained at 5.7 ml/s for the duration of steam exposure. Post-test O/U ratios were calculated from the weight increases after oxidizing segments of the specimen to U_3O_8 in air. Other segments of the sample were examined by scanning electron microscopy (SEM) and optical microscopy.
We have plotted Cox *et al.*'s data on oxide weight gain and the O/U ratio versus time at 1273 K in Figs. 3(a) and 3(b), respectively. It is seen that an equilibrium in composition (O/U ratio) is attained with steam after 320 h, beyond which no further change in oxidation was observed. As can be seen from Fig. 3(a), the location of the data point at 450 h implies weight loss at constant composition. This kind of behavior was also observed by Cox *et al.* at higher temperatures, at which the observed weight losses became more rapid with increasing temperature. Cox *et al.* attributed this behavior to volatilization of UO_2.
The data obtained by the experimenters are consistent with the Carter-Lay relation (2), for

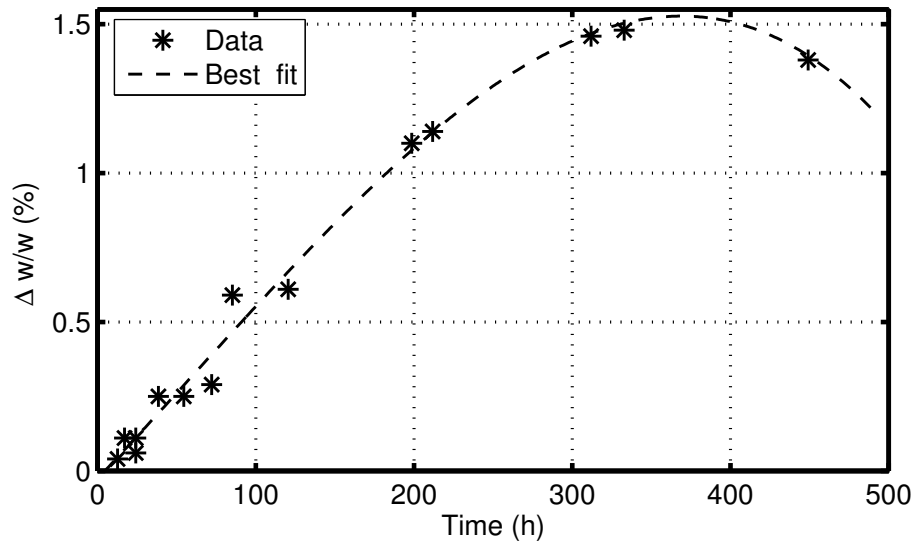

(a)

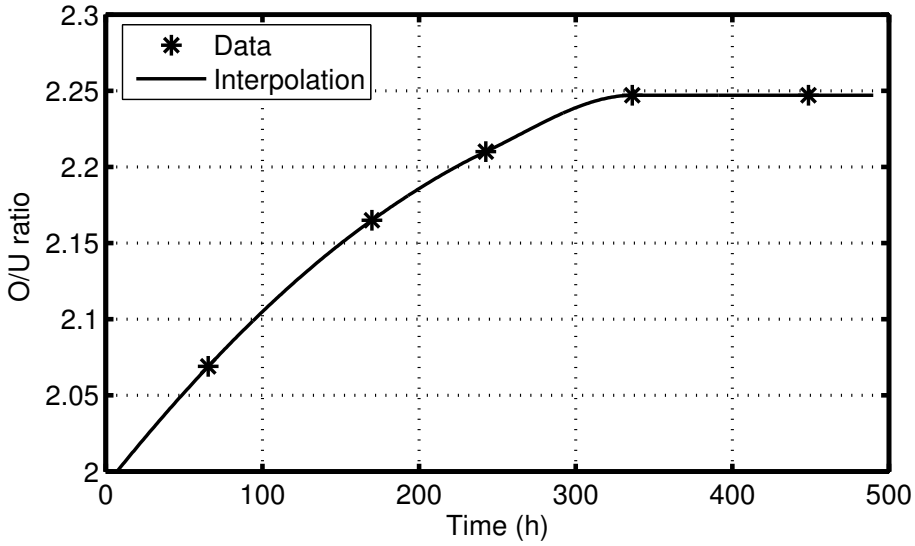

(b)

Figure 3: Oxidation of UO_2 in steam at 1273 K and 0.1 MPa; from Cox *et al.*'s experiment [14]. (a) Oxide weight gain ratio $\Delta w/w$ versus time. (b) Oxygen to uranium ratio versus time.

which the temperature dependence of the rate constant was obtained by fitting the data to an Arrhenius type relation: $\alpha = A\exp(-Q/T)$. Table 1 shows Cox *et al.*'s parameters compared with that of an earlier study by Bittel, Sjodahl and White at General Electric, Cincinnati [22] and later studies discussed in the succeeding subsections. In Fig. 4, we have depicted the time evolution of O/U ($\equiv 2 + x$) using Eq. (3) and α's listed in Table 1 from various authors for pure steam at 1273 K with $x_{eq} = 0.25$. In these computations, we have utilized the geometric $S/V = 457$ m^{-1} as computed from the aforementioned UO_2 pellet dimensions. Comparing the measured data displayed in Fig. 3(b) with the prediction of Eq. (3) and α from Cox *et al.*, we note that the agreement is fair. However, the large deviations of Cox *et al.* and Imamura-Une's from the other two are somewhat unexpected.

Table 1: The surface exchange coefficient for unirradiated UO_2 oxidation obtained by experiments, expressed as $\alpha = A\exp(-Q/T)$.

Data	Environment	A	Q	T-range	Source
...	...	m/s	K	K	...
Cox et al.	Pure steam	0.365	23500	1273-1923	[14]
Bittel et al.	Pure steam	0.0697	19900	1158-2108	[22]
Abrefah et al.	Pure steam	0.456	22080	1273-1623	[15]
Abrefah et al.	Steam/Ar/H_2	0.166	20000	1273-1623	[15]
Imamura-Une	Pure steam	0.000341	15876	1073-1473	[17]
Imamura-Une	10vol%H_2O_2/H_2O	0.0456	18763	1073-1473	[17]

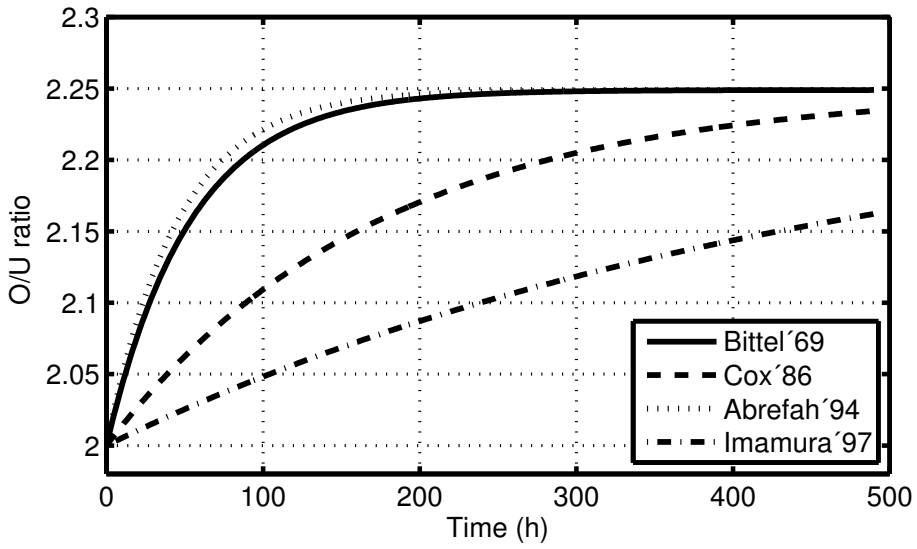

Figure 4: Calculated oxidation of UO_2 in pure steam at 1273 K for $S/V = 457$ m^{-1} using Eq. (3) and the surface exchange coefficients from various authors listed in Table 1, *cf.* figure 3(b).

The CRL experimenters also studied fuel oxidation in air. The oxidation of UO_2 in air at 500°C (773 K) proceeded by grain boundary reaction, producing subgrain sized fragments of U_3O_8. Their oxidation tests at 900 -1200°C produced large columnar grains of U_3O_8 and the kinetics exhibited that the "breakaway" oxidation was controlled by solid state (chemical) diffusion of oxygen [14].

UC Berkeley experiments Olander's group, Abrefah *et al.* [15], at the University of California Berkeley (UC Berkeley), experimentally studied the oxidation of UO_2 in pure steam and in $H_2O/Ar/H_2$ mixtures in the temperature range $1273 - 1623$ K at atmospheric pressure. Thin disk-shaped samples cut from depleted UO_2 pellet of 94% theoretical density were used. The samples were 10 mm in diameter and $0.5 - 1$ mm thick. Both single crystal and polycrystal UO_2 were used. The tests were conducted in a continuously recording thermogravimetric apparatus, where the weight change of the specimen due to oxidation was recorded by microbalance. The details of the experimental set up are described in [15]. The experimenters monitored the mass gain Δw_{ox} until no further change was observed or until (at high temperatures) a constant mass loss due to volatilization of urania was obtained. The mass gain at this stage Δw_{eq} corresponds to the state of equilibrium of the sample stoichiometry.
The O/U ratio is related to the specimen weight gain by

$$c = \left(\frac{\mathrm{O}}{\mathrm{U}}\right) = \frac{\Delta w_{ox}}{w_0}\frac{270}{16} + 2, \tag{4}$$

where w_0 is the initial specimen mass measured before the start of the experiment. Similarly, the mass gain at equilibrium measured by the microbalance for each test yields the equilibrium oxide stoichiometry

$$c_{eq} = \left(\frac{\mathrm{O}}{\mathrm{U}}\right)_{eq} = \frac{\Delta w_{eq}}{w_0}\frac{270}{16} + 2. \tag{5}$$

In terms of the deviation from stoichiometry, namely $x = \mathrm{O/U} - 2$, we write

$$\frac{x}{x_{eq}} = \frac{\Delta w_{ox}}{\Delta w_{eq}}. \tag{6}$$

The effect of the temperature (in the range 1273-1623 K) on the rate of oxidation of UO_2 was clearly observed by Olander's group, which showed the higher the temperature, the higher is the oxidation rate and the faster the saturation is attained. For example, at 1273 K, saturation was attained after about 1083 min while at 1423 K after around 100 min. The equilibrium O/U ratio data as a function of temperature are depicted in Fig. 5 and the data versus time at 1673 K are shown in Fig. 6. The latter figure also shows fittings of the data to the equation of the form (3), *i.e.*, $x = x_{eq}(1 - \exp(-t/\tau))$, where τ is a relaxation time constant obtained by Abrefah *et al.* [15]. The relaxation time constant, as can be inspected from Eq. (3), is related to reaction rate α and sample surface-to-volume ratio in the manner $\alpha = (V/S)/\tau$. As can be seen, the result of the fit for oxidation in pure steam, at 1623 K, is unsatisfactory. Hence, this type of empirical modeling does not describe the data for pure steam properly. However, for the $H_2O/Ar/H_2$ mixture, as has been pointed out in [15], the empirical approach works reasonably well.
The experimenters [15] further investigated the effect of partial pressure of hydrogen ($P_{\mathrm{H_2}}$) in the H_2O/H_2 ratio of the mixture on the reaction rate of oxygen α at different temperatures. Figure 7 shows this dependence at 1473 K for two different sample sizes. It is seen that as the pressure is increased, the oxidation rate increases in a nearly parabolic fashion. The temperature dependence of α in pure steam and steam/Ar/H_2 is given in Table 1. There is no effect of the H_2O/H_2 ratio of steam/Ar/H_2 mixture. The rate constant obtained from oxidation experiments in Ar/H_2O mixture indicates that α depends on the square root of

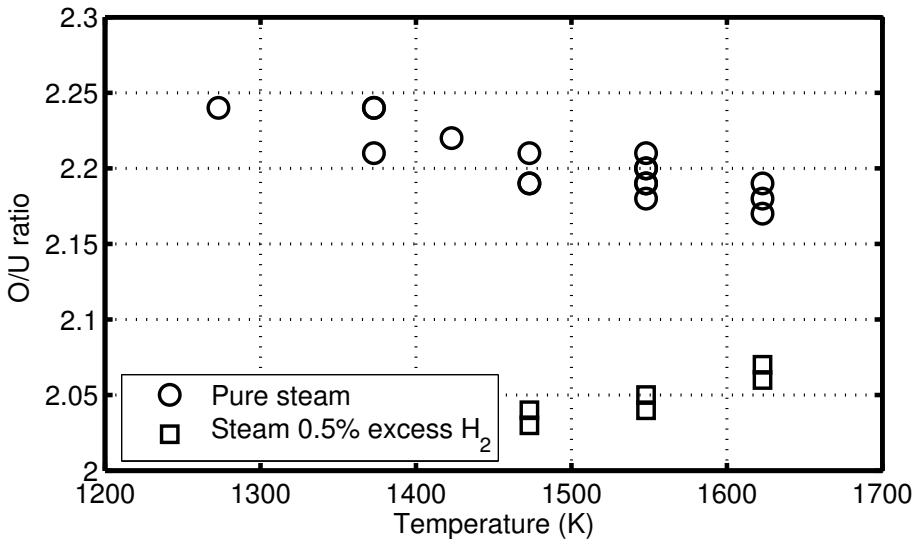

Figure 5: Equilibrium O/U ratio on polycrystalline samples at various temperatures; H_2 partial pressure in steam/hydrogen mixture is 0.005 atm (500 Pa), after Abrefah *et al.* [15].

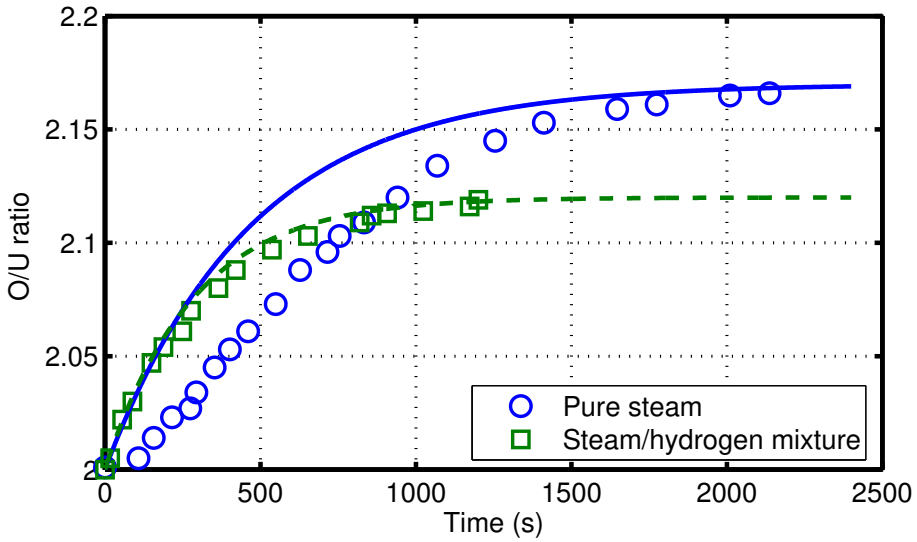

Figure 6: Evolution of O/U ratio on polycrystalline samples at 1623 K. H_2 partial pressure in steam/hydrogen mixture is about 500 Pa [15].

steam pressure (parabolic law). Abrefah *et al.* [15] also observed volatilization of UO_2 in

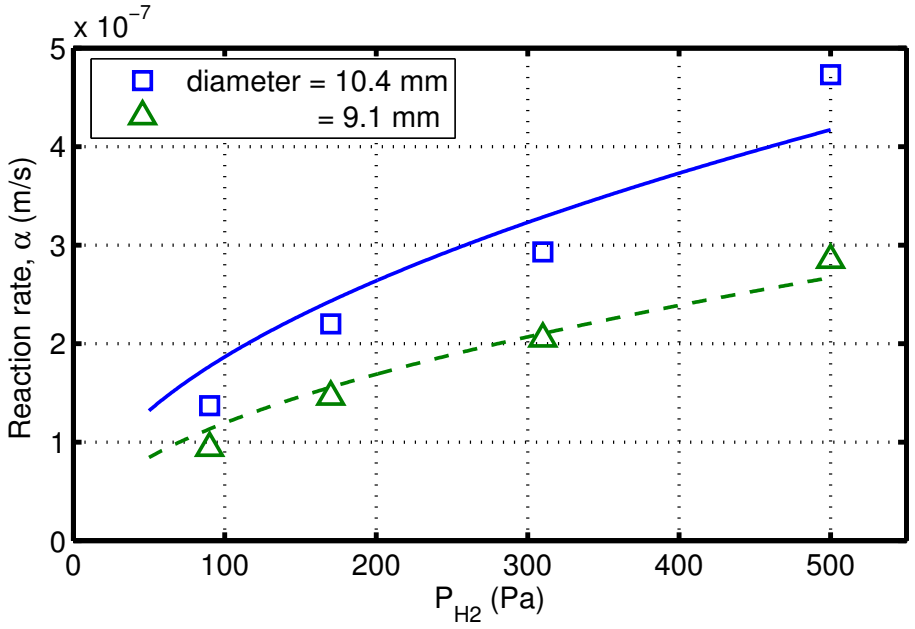

Figure 7: Dependence of the oxidation reaction rate on hydrogen partial pressure in the steam/hydrogen mixture environment at 1473 K [15]. The lines are parabolic fits to the data for two different sample sizes.

steam and H_2O/Ar/H_2 mixtures. This effect occurred at high temperatures and also at temperatures as low as 1273 K. The rate of volatilization of their polycrystalline samples was higher than that of single crystal samples, implying the grain boundaries are the preferred sites for urania vaporization in steam.

CEA experiments Fuel oxidation experiments have been conducted using a thermogravimetry technique by researchers at the Commissariat à l'Energie Atomique (CEA Grenoble and CEA Fontenary aux Roses) [23]. Sample UO_2 fuel pellets were cut into slices with a weight of 0.7 g and a diameter of 8 mm. The specimens were then put into a crucible in which gaseous flow, He-3% H_2O (5 l/h at STP), was introduced. The specimen temperature was kept at 1473 K. Two sets of measurements, one for sintered UO_2 specimens containing no open porosity, another with 3% open porosity, were reported in [23]. The surface to volume ratio for sintered pellets was $S/V = 700$ m^{-1}, whereas that for 3% open porosity specimen was estimated to be about 1.6 to 2.3 times larger. The results are displayed in Fig. 8. As can be seen, the oxidation rate is a bit higher for the fuel specimen with 3% open porosity. Moreover, using Eq. (3) and the surface exchange coefficients from Cox *et al.* in Table 1 at $T = 1473$ K, and $S/V = 700$ m^{-1}, $x_{eq} = 0.16$, we have computed the time evolution of x for this experiment. As can be seen from Fig. 8 the measured data (closed porosity) are duly captured by the dashed line.
The experimenters also examined the effect of steam pressure on the surface-exchange coefficient α, *i.e.* $\alpha(P_{\mathrm{H_2O}})^m$, by repeating the experiment at several values of $P_{\mathrm{H_2O}}$. They found that the oxidation rate depends on the square-root of the steam pressure ($m = 1/2$) in the domain of 0.01 to 1 atm.

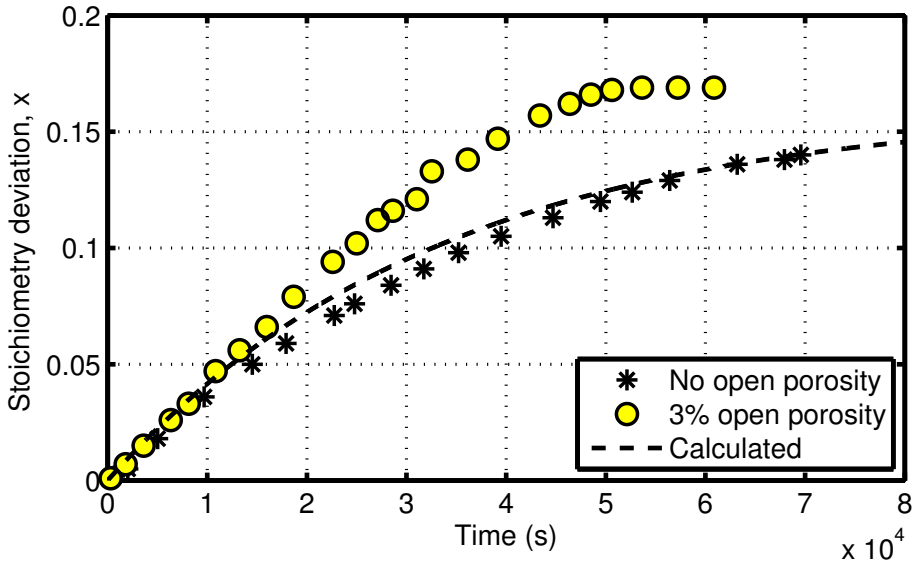

Figure 8: Stoichiometry deviation of UO_2 in steam-He mixture from CEA-experiments on unirradiated samples under a total pressure of 0.1 MPa, steam pressure of 0.0033 MPa and temperature of 1473 K [23]. The dashed line is calculated as explained in the main text

UC Berkeley experiments The aforementioned experiments, discussed in the preceding paragraphs, examined the kinetics of UO_2 oxidation in steam at temperatures greater than 1000 K and at atmospheric pressure and below. These studies were primarily directed toward characterizing severe-accident behavior of oxide fuel. They showed unequivocally that the oxidation rate is controlled by the surface reaction, in which water molecules are decomposed to produce oxygen atoms that enter the solid and hydrogen that returns to the gas. Olander and coworkers have measured the oxidation kinetics of UO_2 at pressures of 0.7 and 7 MPa (7 and 70 atm) and temperatures of 773 and 873 K [7]. They conducted experiments in a high-pressure thermobalance described in [7]. Unirradiated UO_2 samples (disks about 1 mm thick and 10 mm in diameter) were used in the experiment. To investigate the oxidation behavior in pure steam, they injected pure steam from the bottom of their apparatus.

The experimenters conducted only one test in a H_2/H_2O gas mixture. In this test, no weight gain was observed after one week of exposure in 4 mol%H_2 in steam at 7 MPa and 873 K. They note that in order to allow for significant oxidation of UO_2, meaning that the O/U ratio reaching the upper boundary of the fluorite phase of uranium dioxide, the H_2 concentration would have to be reduced to a few ppm at 773-873 K. This low concentration of hydrogen in steam is very difficult to achieve experimentally, and besides, this condition is atypical of the gas in the pellet-cladding gap of defected fuel rod.

Other tests were conducted in pure steam with two objectives: (i) to compare the low-temperature oxidation kinetic data with the ample high temperature data, (ii) to determine how the steam pressure influences oxidation kinetics. All the tests exhibited a constant rate of weight gain, indicating linear oxidation kinetics. In tests of two weeks duration, the oxide weight gain for initially stoichiometric specimens corresponded, at most, to $UO_{2.02}$. Furthermore, post-test examination of specimens by SEM and optical microscopy showed that fuel microstructure was essentially identical to that of the unexposed UO_2.

The measured mass gain rates were converted to oxidation rates per unit area to allow

comparison with the high-temperature data, as depicted in Fig. 9. The results of the 7 MPa tests are displayed as triangles in this figure. They show, at the two measured temperatures (773, 873 K), a reduced activation energy of 19055 K, which is not too far from the value for the high temperature data (18054 K). Nonetheless, the 7 MPa data at the two temperatures lie clearly above the extrapolation of high-temperature data, showing a measurable steam-pressure effect on the oxidation kinetics. On the other hand, the 0.7 MPa data at 873 K falls fairly well with the 0.1 MPa (1 atm) high temperature test lines of Cox *et al.* [14] and Imamura and Une [17]. Olander *et al.*'s experiments [7] show that the oxidation rates at 7 MPa and 0.7 MPa differ by a factor of about 3, thus confirming the $\sqrt{P}$ dependence of the oxidation rate.

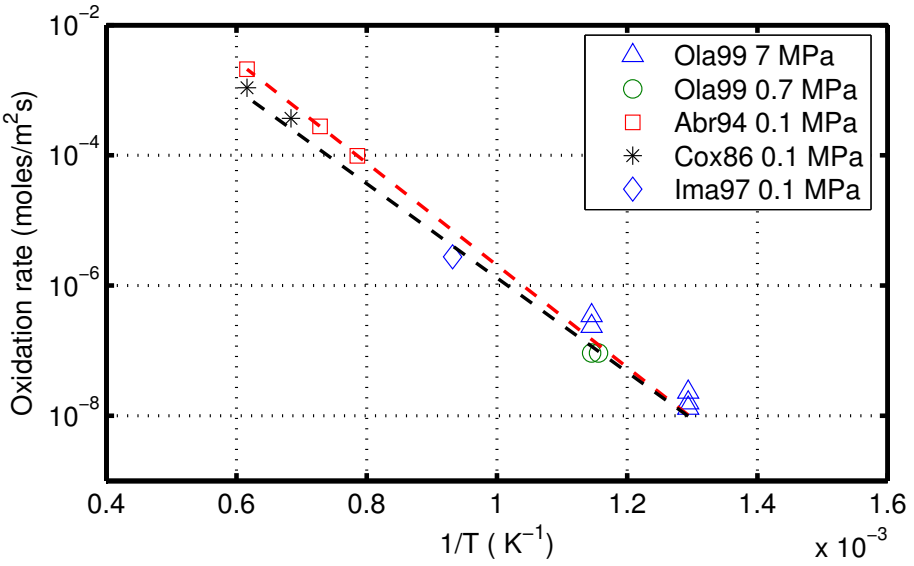

Figure 9: Initial oxidation rates of UO_2 in pure steam. The dashed lines are fit to the high temperature data. Legend refers to: Ola99 [7], Abr94 [15] Cox86 [14] and Ima97 [17].

2.1.2 Irradiated fuels

Chalk River experiments A number of post-irradiation annealing tests were conducted at the CRL, for temperatures ranging from 1600 to 1900 K. The tests included both bare UO_2 samples and short-length test rods (mini-pins) with Zircaloy-4 cladding [23, 24]. All fuel samples were obtained by cutting a section of a spent single fuel rod of a CANDU-type design. The mini-pins also contained loose-fitting Zircaloy end plugs. A number of samples from these experiments, for which sufficient input data for impending modeling were given, are summarized in Table 2.

Each fuel sample was introduced into a flowing mixture of argon/2% H_2 (400 ml/min at STP) and ramped (0.9 K/s) to a given temperature plateau of: 1623 K (CF2 and CM2), 1773 (CF3 and CM6). After the temperature plateau had been reached, the fuel was immediately exposed to an oxidizing mixture of steam (60 g/h) and argon (100 ml/min at STP). The oxygen partial pressure of the atmospheric composition was monitored with oxygen sensors [25]; and fission products released from the fuel specimens were swept away such that the installed gamma-ray spectrometer monitored the fission product release. In the mini-pins,

Table 2: Summary of annealing experiments at Chalk River on UO_2 fuel samples with a discharge linear power density of 32.1 kW/m and burnup of 457.2 MWh/kgU. Atmospheric conditions for temperature ramp: argon/2% H_2 at 400 ml/min Ar; after Lewis *et al.* [23].

	Bare fuel(UO_2 chips)		Mini-pin (UO_2/Zry-4)	
	HCE2-CF2	HCE2-CF3	HCE2-CM2	HCE2-CM6
U-235 wt% in U	1.38	1.38	1.38	1.38
Sample weight (g)	0.566	0.534	14.70	16.89
S/V ratio (m^{-1})	2.07×10^4	2.11×10^4	1.65×10^3	1.53×10^3
Grain size (μm)	3.5	3.5	6.5	6.5
Temperature (K)	1626	1777	1628	1768
Temp. ramp (K/s)	0.9	0.9	0.9	0.9
Hold steam time (h)	2	1.5	2.5	2.5
End-state x	0.18	0.16	0.18	0.16

hydrogen production from Zircaloy-steam reaction will reduce the oxygen potential of the atmosphere, thereby hampering fuel oxidation and fission product release.
Figure 10(a) shows data on the average fuel stoichiometry deviation obtained from the oxygen partial pressure measurements as a function of time for CF2 and CF3 samples extracted from figure 1 in [23]. Their corresponding measured end-state x values are given in Table 2. The mini-pin tests (CM2 and CM6) were conducted under the same conditions of temperature and steam as the bare UO_2 samples, except that they were clad in Zircaloy-4 (with end plugs). Due to this addition, the oxygen potential was continually changing as a result of Zr-steam reaction at high temperature. Therefore, Lewis and coworkers could not measure the fuel oxidation kinetics of CM2 and CM6 samples instantaneously during the tests. Nevertheless, since all Zr in Zircaloy-4 was converted into zirconium dioxide by the end of each test, they could estimate the final mass gain for the fuel from the oxygen pressure measurements. The experimental end-state x values for CM2 and CM6 are given in Table 2. The corresponding data on measured fractional release of ^{134}Cs are depicted in Figure 10(b). These and other measurements reported in [23] offer a valuable database for model benchmarking as made by the authors themselves.

NFD experiments Imamura and Une [17] of the Nippon Nuclear Fuel development Co. (NFD) conducted steam oxidation of UO_2 at temperatures 1073 and 1273 K for both unirradiated and irradiated samples. The unirradiated samples were 1.00±0.01 mm cubes cut from sintered UO_2 fuel pellets with 97% of the theoretical density. Three-dimensional mean grain size was 16 μm. The O/U ratio of the unirradiated specimens was 2.005. The surface-to-volume ratio (S/V) of samples, as measured by the BET method,[2] was 210.5 cm^{-1} (21050 m^{-1}). The irradiated samples were prepared from UO_2 fuel pellets irradiated in a commercial BWR to a burnup of 27 MWd/kgU. The fuel samples, roughly 1 mm cubes, were taken from the outer region of the irradiated pellets.
The steam oxidation device used by the NFD experimenters consisted of a microbalance, a steam generator, an electric furnace and a steam condenser. The weight change of the sample as a function of time was measured by the microbalance. The UO_2 fuel samples were heated to a preset temperature in various atmospheres, namely H_2O, H_2/H_2O and

[2] After S. Brunauer, P. H. Emmett and E. Teller, *J. Am. Chem. Soc.* 60 (1938) 309.

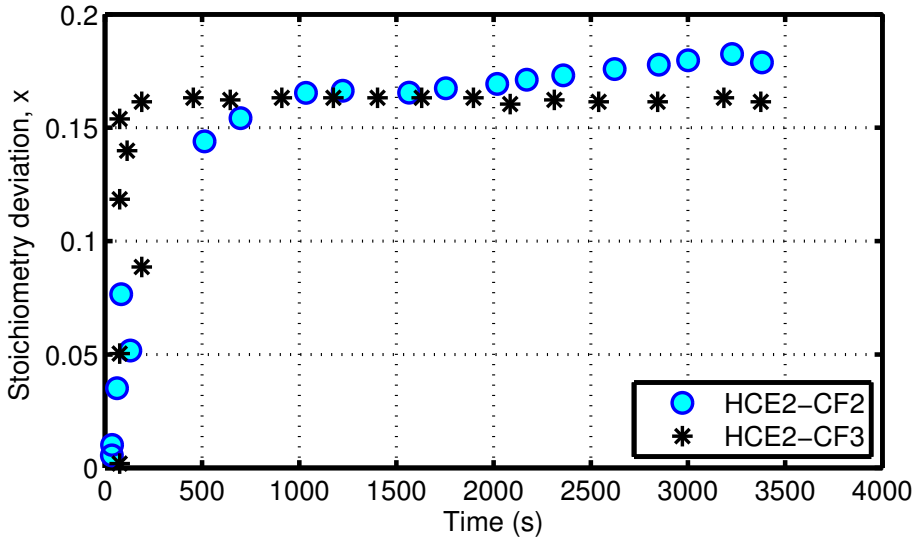

(a)

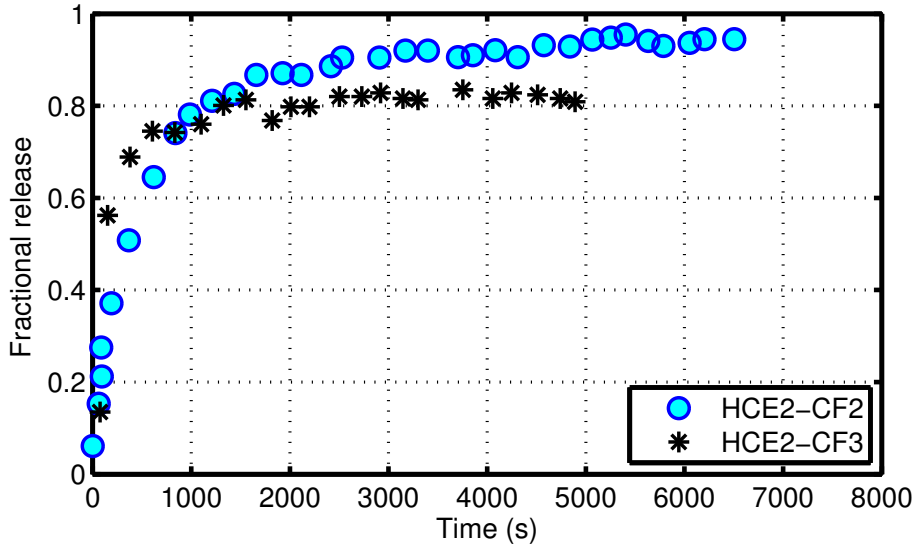

(b)

Figure 10: Temperature ramp experiments at Chalk River on UO_2 fuel samples in steam-Ar mixture HCE2-CF2/CF3 tests with fuel burnup of $\approx$ 19 MWd/kgU, total pressure of 0.1 MPa and steam pressure of 0.0899 MPa, *cf.* table 2. (a) Stoichiometry deviation of UO_2 vs. time. (b) Fractional release of ^{134}Cs vs. time; after Lewis *et al.* [23]

H_2O_2/H_2O. Steam was generated by a boiler connected to the furnace. The average steam flow rate was about 400 cm^3/min, which was controlled by a flow meter. After the steam oxidation tests, the fuel oxidation (O/U ratio) at local sites, on a micron scale, was examined by electron probe micro analyzer (EPMA). The error in evaluating the local O/U ratio was reported to be ± 0.005.

In failed fuel rods, hydrogen that is produced by the reaction of steam with fuel and the inner wall of the cladding and radiolysis of compounds, such as hydrogen peroxide, coexists with steam. The NFD experimenters used Ar-0.2%H_2 gas (Ar as a carrier gas) to examine the influence of released hydrogen on steam oxidation. In order to study the effect of hydrogen peroxide on the steam oxidation, steam containing various amounts of hydrogen peroxide was used. More specifically, the concentrations of hydrogen peroxide were 1, 5, 10 and 30 vol%. The H/O ratios were 1.9978, 1.9888, 1.9767 and 1.9158, respectively. They showed that the oxygen potential increases with the concentration of hydrogen peroxide. For example at 1273 K, the oxygen potentials in 1, 5, 10 and 30 vol% H_2O_2/H_2O were evaluated to be $-100, -83.3, -73.8$ and -59.3 kJ/mol, respectively. Their figure 2 in [17] depicts the oxygen potential as a function of temperature and the O/U ratio; see appendix A.3. This effect has a large impact on the oxidation rate of UO_2. The larger is the H_2O_2/H_2O ratio the higher will be the oxidation rate [17].

After the steam oxidation test, the EPMA showed that the local O/U ratio in the outermost region of the sample was 2.25 corresponding to the single phase of U_4O_9. However, the profiles of the O/U ratio in the inner region of fuel samples were almost flat with values equal to the O/U ratio after the oxidation tests (*e.g.* 2.06 at 1273 K, *cf.* figure 4 in [17]). The EPMA results showed that the oxidation process is controlled by a reaction taking place at the solid/gas interface. The measured O/U ratios versus time at 1073 and 1273 K for unirradiated samples are shown in Fig. 11(a). The higher temperature gives a higher oxidation rate. Similarly, irradiation enhances the oxidation rate, see Fig. 11(b).

The Imamura-Une oxidation rate parameters for unirradiated UO_2, are presented in Table 1. Figure 12 compares the temperature dependence of the different correlations, listed in Table 1, for pure steam oxidation. As can be seen from this figure, the Imamura-Une data show about an order of magnitude below than the other workers' data at high temperatures. The authors offer two reasons for this disparity, namely (i) a difference in the S/V ratio between the samples, (ii) a difference in steam partial pressure. Imamura and Une used the BET-method to determine the S/V ratio, while the former investigators used nominal design surface-to-volume ratios. In addition, the Imamura-Une steam partial pressure was 0.12 atm, whereas Cox *et al.* [14] and Abrefah *et al.* [15] utilized 1 atm for the steam pressure. Since α is proportional to the square root of the steam partial pressure, the values of α from the Imamura-Une experiments at $P_{H_2O} = 1$ atm become 2.89 ($= \sqrt{1/0.12}$) larger, which become closer to the values obtained by other workers.

Regarding irradiated fuel, Fig. 11b shows that the O/U ratio for pellets in pure steam at 1273 K develops faster than in unirradiated fuel. However, Imamura-Une's analysis indicates that the steam oxidation of irradiated UO_2, as in unirradiated fuel, is controlled by a reaction at the solid/gas interface. Moreover, they posit that the reaction rate α of irradiated fuel is equal to that of the unirradiated fuel. Further, they evaluated the surface-to-volume ratio (specific surface area) from the relation $S/V = (\alpha\tau)^{-1}$ and found that for irradiated samples, taken from the pellet outer region, $S/V = 55500$ m^{-1}, *i.e.* about 2.6 times that of the unirradiated UO_2 samples.

They also examined the effect of liberated hydrogen by performing steam oxidation tests in Ar-0.2%H_2 mixed gas at 1473 K using unirradiated samples. They determined the ox-

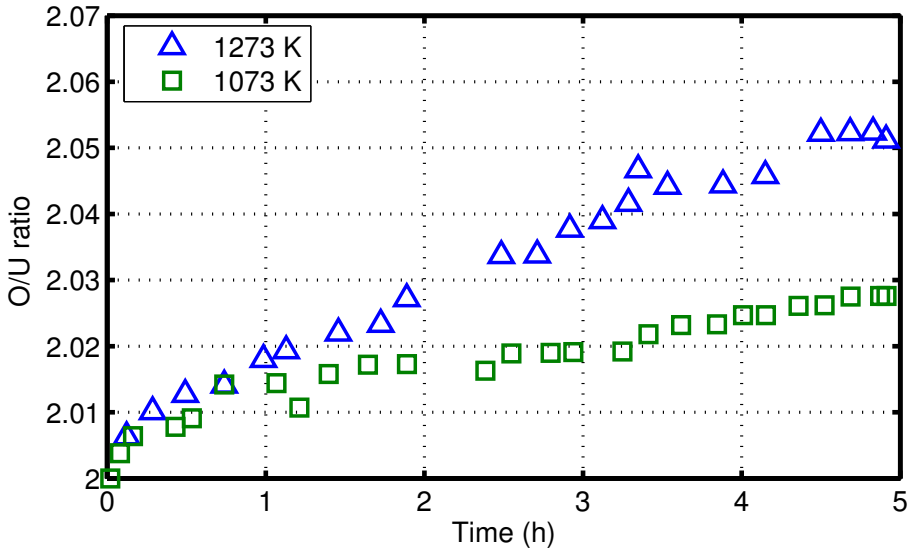

(a)

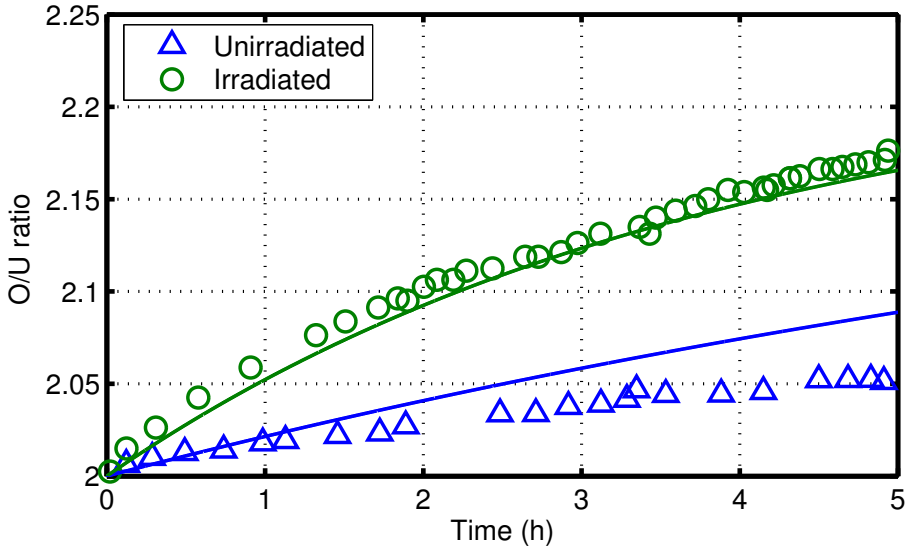

(b)

Figure 11: Oxidation of UO_2 in steam from Imamura and Une [17]; (a) unirradiated samples, (b) at 1273 K. The lines are fit according to the Carter-Lay description, equation (3).

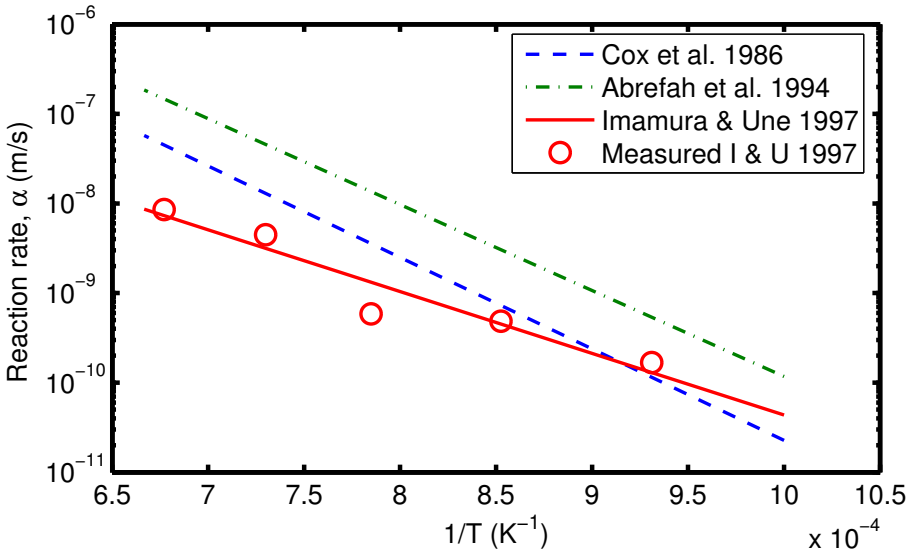

Figure 12: Arrhenius plots for the oxidation reaction rate of unirradiated UO_2 in pure steam obtained by various workers; see table 1.

idation reaction rate constant to be $\alpha = 7.94 \times 10^{-9}$ m/s in 0.2%H_2/H_2O versus $\alpha = 7.11 \times 10^{-9}$ m/s in pure steam. This means that the liberated hydrogen has a negligible effect on the steam oxidation rate constant. Our calculations show that in pure steam at 1473 K and 0.12 atm, $(O/U)_{eq} = 2.182$, whereas $(O/U)_{eq} = 2.087$ in 2%H_2/H_2O.
Finally, they examined the influence of hydrogen peroxide on oxidation of unirradiated UO_2 in Ar/H_2O/H_2O_2 gas mixture at 1273 K. The concentrations of H_2O_2 used in the furnace were 1, 5, 10 and 30 vol%, and the duration of the tests was 5 h. The oxidation rate became higher as the concentration of H_2O_2 was increased, Fig. 13(a). For example, in the case of 10 vol% H_2O_2, the O/U ratio reached its equilibrium value in less than 2 h, $(O/U)_{eq} = 2.615$. At 1273 K, the reaction rate (surface exchange coefficient) was $\alpha = 1.81 \times 10^{-8}$ m/s for 10 vol% H_2O_2 compared to $\alpha = 1.31 \times 10^{-9}$ m/s in pure steam, *i.e.* more than an order of magnitude larger. Figure 13(b) depicts the oxygen potential $\Delta\bar{G}_{O_2}$ for the H_2O_2/H_2O mixtures as a function of temperature. In Appendix A.3 the oxygen potential is defined and its dependence on the O/U and H_2/H_2O ratios as a function of temperature are evaluated. Figure 14 shows plots of the correlations deduced in [17] for the oxidation reaction rate of UO_2. It is argued that during oxidation, the H_2O_2 molecules accelerate the decomposition of steam and therefore the α value gets larger [17].

2.2 Fuel oxidation modeling

2.2.1 Langmuir based approach

In section 2.1, we outlined the empirical approach of Carter and Lay for treating oxidation of UO_2 fuel. The Carter-Lay description, as it stands, does not account for the pressure dependence of oxidation. Neither it regards the effect of gas mixture, *e.g.* the concentration of hydrogen, in the oxidation process. Dobrov *et al.* [26] introduced the Langmuir theory of adsorption in the kinetics of UO_2 oxidation, reaction (1), which was extended and used subsequently [20, 27]. Using the Langmuir theory, the kinetics of oxidation reaction is

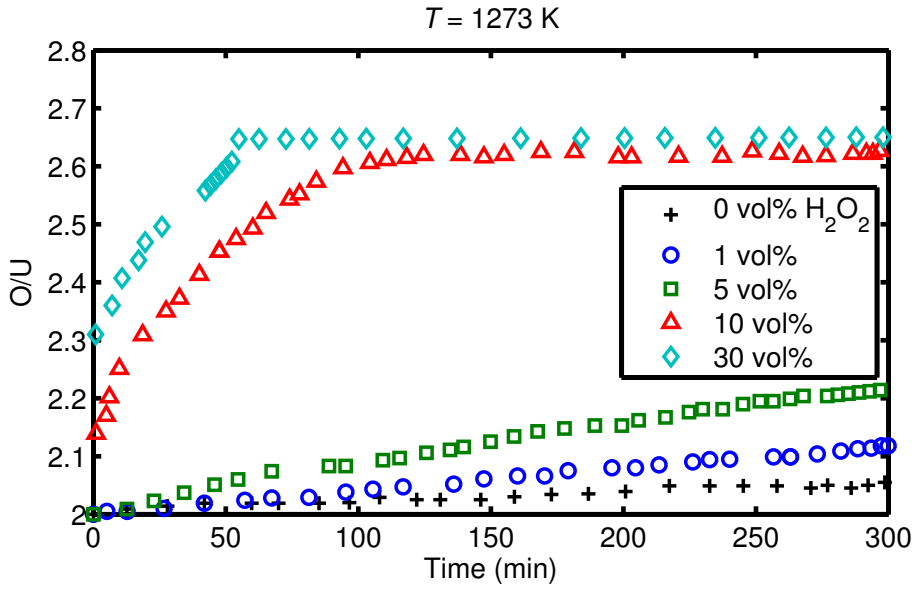

(a)

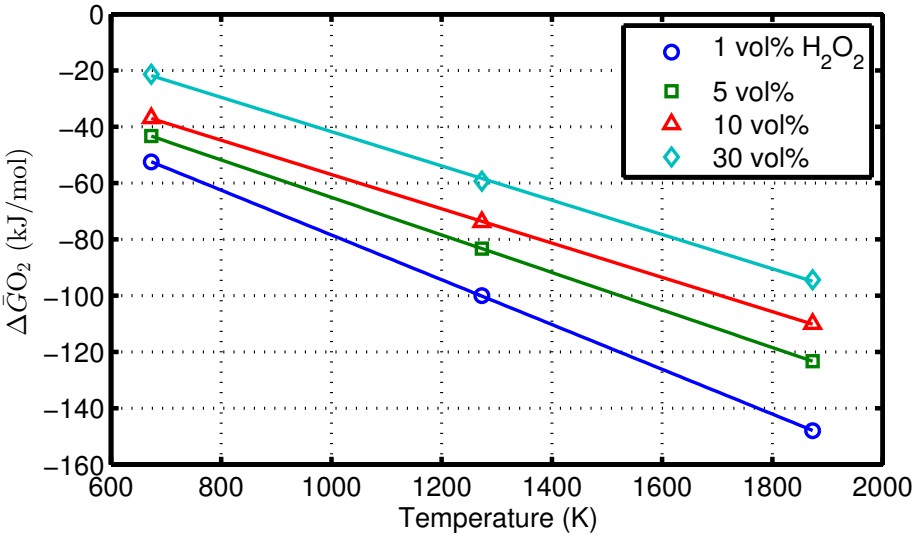

(b)

Figure 13: Effect of hydrogen peroxide in steam (H_2O_2/H_2O mixture) on oxidation of unirradiated UO_2 from Imamura and Une [17]: (a) Measured time evolution of UO_{2+x} stoichiometry at 1273 K, adapted from figure 8 of Imamura and Une [17] at 1273 K. (b) Evaluated oxygen potential $\Delta\bar{G}_{O_2}$ versus temperature.

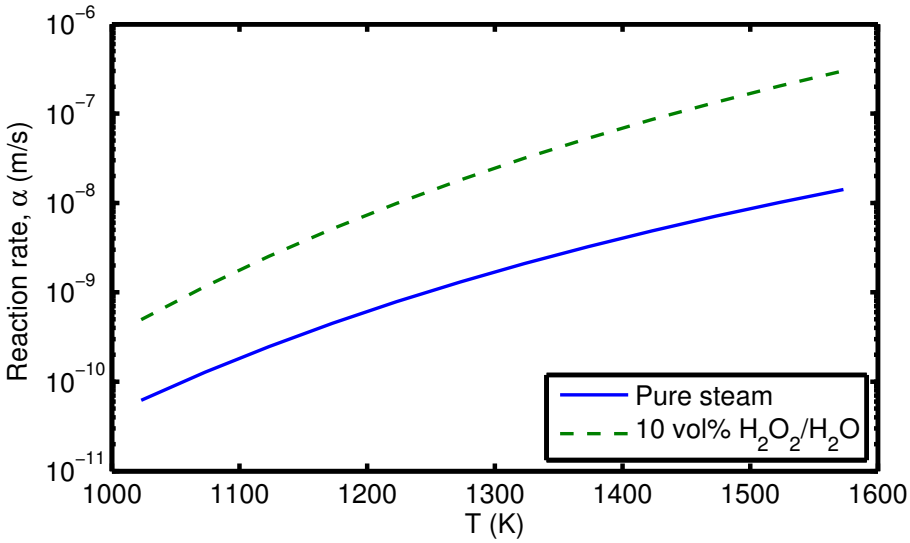

Figure 14: Effect of hydrogen peroxide on the oxidation reaction rate of unirradiated UO_2; from Imamura and Une [17].

expressed by [26]

$$\frac{dx}{dt} = \frac{\Theta(T, P_{\mathrm{H_2O}})}{\tau_c}\Big[1 - \frac{q(x)}{P_{\mathrm{H_2O}}/P_{\mathrm{H_2}}}\Big], \tag{7}$$

where τ_c is a characteristic time for oxidation

$$\frac{1}{\tau_c} = \frac{n_s k'_a}{\rho_U}\Big(\frac{S}{V}\Big) \equiv \alpha\frac{S}{V}. \tag{8}$$

Here, $n_s = 1.66 \times 10^{-6}$ mol m^{-2} is the density of adsorption sites assuming a monolayer coverage of 10^{18} molecules m^{-2} [27], k'_a is the steam dissociation rate constant (to be specified), and ρ_U the molar density of uranium, which is $\rho_U = 4 \times 10^4$ mol of uranium m^{-3}. In Eq. (7), Θ is the surface coverage term from the Langmuir adsorption theory, expressed as

$$\Theta(T, P) = \frac{A(T)P_{\mathrm{H_2O}}}{1 + A(T)P_{\mathrm{H_2O}}}, \tag{9}$$

with

$$A(T) = 1.0135 \times 10^5 \frac{B_{\mathrm{H_2O}}}{n_s k_a}, \tag{10}$$

in unit of (atm^{-1}), k_a the desorption rate constant, $B_{\mathrm{H_2O}} = s/\sqrt{2\pi RTM_{\mathrm{H_2O}}}$, s the sticking probability, $R = 8.314$ Jmol^{-1}K^{-1}, and $M_{\mathrm{H_2O}} = 0.018$ kg mol^{-1}. In Eq. (7), the oxygen activity $q(x)$ for gas-solid equilibrium is defined as [27]

$$q(x) = \frac{\sqrt{P_{\mathrm{O_2}}(x)}}{K_{\mathrm{H_2O}}}. \tag{11}$$

where $P_{\mathrm{O_2}}(x)$ is the oxygen partial pressure in the fuel (in atm).

For the H_2O decomposition reaction

$$H_2O \rightleftharpoons H_2 + \frac{1}{2}O_2, \tag{12}$$

the mass action constant K_{H_2O} is calculated according to relationship [28]

$$K_{H_2O} = \frac{P_{H_2}\sqrt{P_{O_2}}}{P_{H_2O}} \equiv K_0 \exp\Big[-\frac{\Delta G^0_{H_2O}}{RT}\Big] \tag{13}$$

$$= \exp\Big[0.9797 \ln T - 1.1128 - \frac{28827}{T}\Big], \tag{14}$$

where P_{H_2}, P_{H_2O} and P_{O_2} are the partial pressures (in atm) of steam, hydrogen and oxygen in the gap, respectively, and $\Delta G^0_{H_2O}$ is the change in the standard Gibbs energy of reaction (see table E of [28]). The steam-to-hydrogen partial pressure ratio is calculated from the solution of the transport equations in the fuel rod gap [29] and $P_{O_2}(x)$ is evaluated from thermodynamic correlations presented in appendix A; see also the treatment in [30].
The desorption rate constant k_a, the steam dissociation constant k'_a and the sticking probability s are not known from direct measurements. Lewis [27, 31] have obtained them by fitting Eq. (7) (at 1 atm) to experimental data. The parameters resulting from the fitting to the fuel oxidation data in the Chalk River experiments at atmospheric pressure are: $k_a = 10^{13}\exp(-21557/T)$ s^{-1}, $k'_a = 2.48 \times 10^{10}\exp(-28105/T)$ s^{-1}, with T in kelvin and $s = 0.023$ [31].
The equilibrium oxygen content of the fuel $x = x_{eq}$ can be found from Eq. (7) by putting $q(x) = P_{H_2}/P_{H_2O}$ or employing Eq. (11)

$$\sqrt{P_{O_2}(x_{eq})} = K_{H_2O}\Big(\frac{P_{H_2}}{P_{H_2O}}\Big). \tag{15}$$

Using the Lindemer-Besmann relations for $P_{O_2}(x)$, outlined in appendix A.1, and relation (14), we can solve Eq. (15) numerically for x_{eq} at a given temperature and hydrogen-to-steam ratio (P_{H_2}/P_{H_2O}). Figure 15 displays the results of such calculations as a function of temperature for hydrogen-to-steam ratios of 0.01% and 0.1%, respectively.
If an H_2O dissociation value is required to maintain equilibrium, the method described in [27], outlined in appendix A.2, may be used to determine the equilibrium in the presence of a gas mixture in the gap.

2.2.2 Olander model

Olander [20], following the work of Dobrov *et al.* [26], has extended their Langmuir based model (LBM) to include the following set of oxidation and reduction reactions

$$H_2O(g) \rightleftharpoons H_2O(ads) \tag{16}$$

$$H_2O(ads) \rightleftharpoons H_2(g) + O(ads) \tag{17}$$

$$O_2(g) \rightleftharpoons 2O(ads) \tag{18}$$

$$O(ads) \rightleftharpoons O(s) \tag{19}$$

where (g)=gas phase, (s)=solid phase, (ads)=adsorption. When the system is at equilibrium, all steps in the above reactions are individually at equilibrium and obey the principle of

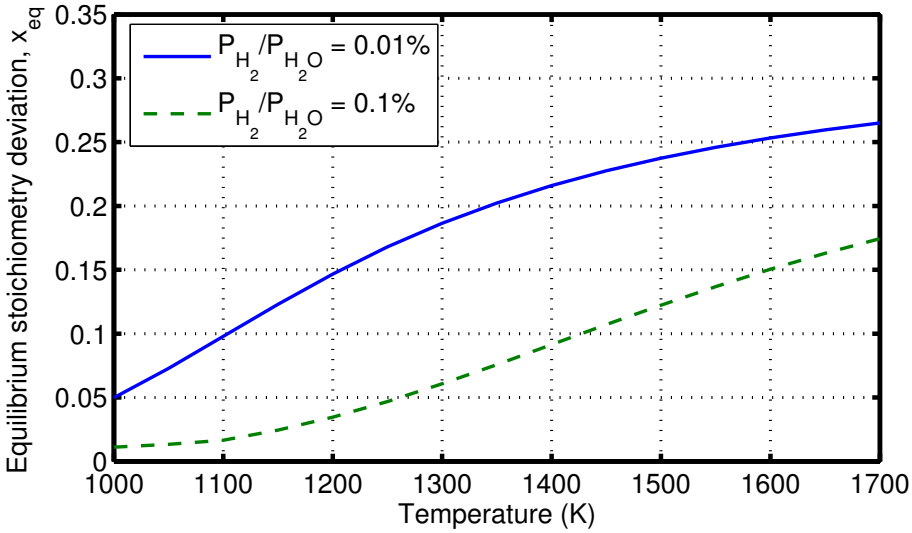

Figure 15: Calculated equilibrium stoichiometry deviation x_{eq} of UO_{2+x} fuel as a function of temperature using the Lindemer-Besmann relations for oxygen partial pressure.

detailed balance. For example, for step (17), we have the balance equation $k''_a\theta_{\mathrm{H_2O}} = kP_{\mathrm{H_2}}\theta_{\mathrm{O}}$ with k being the rate constant for the reverse step of reaction (17), k''_a that for the forward step, and θ_i the fraction of the sites on the surface occupied by species i; see ref. [20] for additional details.

Olander [20] derived an extended version of Eq. (7), expressed as

$$\frac{dx}{dt} = \frac{\theta_{\mathrm{O}}}{\tau_c}\Big[1 - \frac{q(x)}{q_e}\Big], \tag{20}$$

where τ_c was defined earlier through Eq. (8), $q(x)$ by Eq. (11), and the definitions of other parameters are conveniently placed in Box 2.1.

Equation (20) can be solved numerically to obtain x vs. t using an appropriate thermodynamic model for the oxygen activity $q(x)$ and specifying the values for the parameters aP_w and η defined in Box 2.1.

To illustrate the applications of the model, Olander [20] chose arbitrarily the values $aP_w = 0.01$ and $\eta = 0.005$ for a steam pressure of 1 atm at 1623 K. Using these values, Eq. (22) gives $\theta_w = 0.0099$ and Eq. (21) yields $\theta_{\mathrm{O}} = 4.95 \times 10^{-5}$. According to Olander and coworkers [15, 20], at 1623 K, the laboratory experiments show an initial oxidation rate of about 1.2×10^{-4} s^{-1}. At this temperature, $P_w = 5 \times 10^{-9}$ for a steam pressure of 1 atm. The initial oxidation rate when $x \approx 0$ is given by $\dot{x} \approx \theta_{\mathrm{O}}/\tau_c$, since the oxygen activity $q(x)$ is nearly zero; hence in Eq. (20) $\tau_c = 0.38$ s and from Eq. (25), $E = 2.93 \times 10^{-8}$. Furthermore, Eq. (23) gives $q_e = 1710$.

We can calculate x_{eq} as a function of temperature in steam atmosphere (1 atm), based on the equilibrium condition of the reaction (12). Thus, using the expression for $K_{\mathrm{H_2O}}$ given by Olander [21]

$$K_w^{1/2} = \exp\Big[\frac{250800 - 57.8T}{RT}\Big], \tag{27}$$

and Blackburn's expression for the oxygen partial pressure in the fuel, Eq. (A.1) in appendix, at 1623 K, for $q_e = 1710$, we calculate $x_{eq} = 0.177$, which is close to the experi-

$$\theta_{\rm O} = \eta\theta_w \tag{21}$$

$$\theta_w = \frac{aP_w}{1+aP_w(1+\eta)} \tag{22}$$

$$q_e = \frac{\theta_{\rm O}}{E(1-\theta_{\rm O}-\theta_w)} \tag{23}$$

$$\eta = \frac{\gamma}{\delta P_w^{2/3}}; \quad \gamma = \frac{k_a''}{k_a}; \quad a = \frac{2B_{\rm H_2O}}{K_w k_a n_s}; \tag{24}$$

$$\delta = \frac{2k}{K_w k_a}; \quad E = \frac{a\gamma}{\delta}; \quad k_a'' = kP_{\rm H_2}\eta, \tag{25}$$

where P_w is the dimensionless steam pressure

$$P_w = \frac{1}{2}K_w P_{\rm H_2O}; \quad \text{with} \quad K_w = K_{\rm H_2O}^{-2}. \tag{26}$$

Box 2.1: Definition of parameters in Eq. (20).

mentally obtained value at these conditions (pure steam, 1623 K, 1 atm) [15]. We should note that in this computation instead of Eq. (27), we could have chosen Eq. (14), and the results would have virtually been indistinguishable.

The main problem with this model, as it stands, is that we do not know a priori the choice of values for the composite parameters aP_w and η. The choice made in [20] was to fit the experimental data obtained in pure steam at 1623 K and 1 atm to dermine these parameters. To our knowledge, the dependence of these parameters on temperature and partial pressures of the gas mixture has not yet been determined. Hence the model, as it stands, may not be used for reliable prediction of fuel oxidation under various conditions.

2.2.3 Computation of oxidation process

We start our analyses by using the Langmuir based approach or LBM, outlined in section 2.2.1, to calculate the oxidation of urania in pure steam, *i.e.*, we calculate the stoichiometry deviation x vs. time. To do so, we first rewrite Eq. (7) as

$$\frac{dx}{dt} = \frac{\Theta(T, P_{\rm H_2O})}{\tau_c}\Big[1 - \sqrt{\frac{P_{\rm O_2}(x)}{P_{\rm O_2}}}\Big], \tag{28}$$

where we made use of relations (11) and (13). Next, we compute $\Theta(T, P_{\rm H_2O})$ from Eqs. (9) and (10), $P_{\rm O_2}(x)$ from the Lindemer-Besmann relations outlined in appendix A.1, $P_{\rm O_2}$ from Eq. (A.7), and τ_c from Eq. (8) for $S/V = 488.4$ m^{-1}. Then, we solve Eq. (28) numerically (Runge-Kutta algorithm) to obtain x versus t at 1400 K for two initial steam pressures at 0.1 and 7 MPa, respectively. The results are depicted in Fig. 16. It is seen that the pressure dependence of oxidation is rather weak according to this model.

Let us calculate the effect of hydrogen-to-steam ratio on the kinetics of stoichiometry deviation x using the LBM. The results for the hydrogen-to-steam ratios of 0.01% and 0.1% at 1400 K, and input design data listed in Table 3 are shown in Fig. 17. The temperature dependence of oxidation for this input and $P_{\rm H_2}/P_{\rm H_2O} = 0.01\%$ is displayed in Fig. 18,

where a strong dependence on temperature is observed.

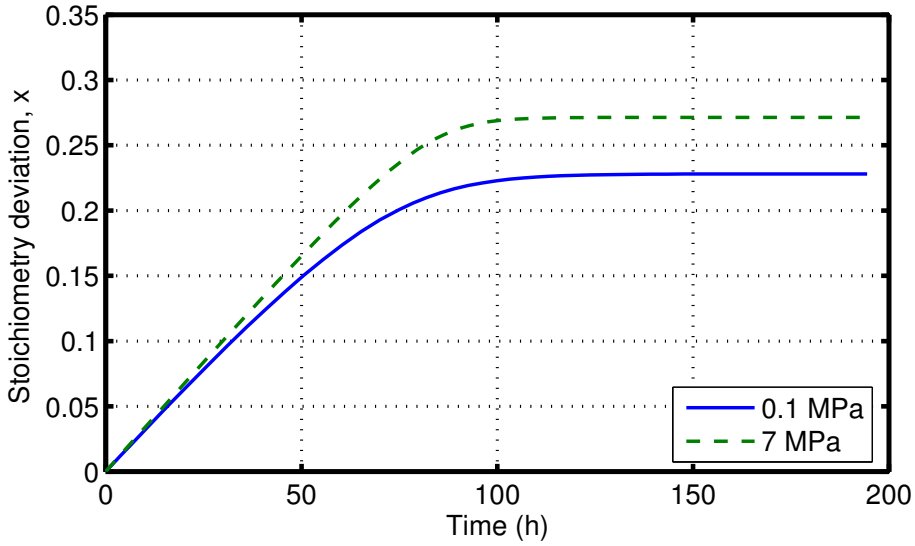

Figure 16: Oxidation of urania in pure steam at 1400 K for $S/V = 488.4$ m^{-1} using the LBM.

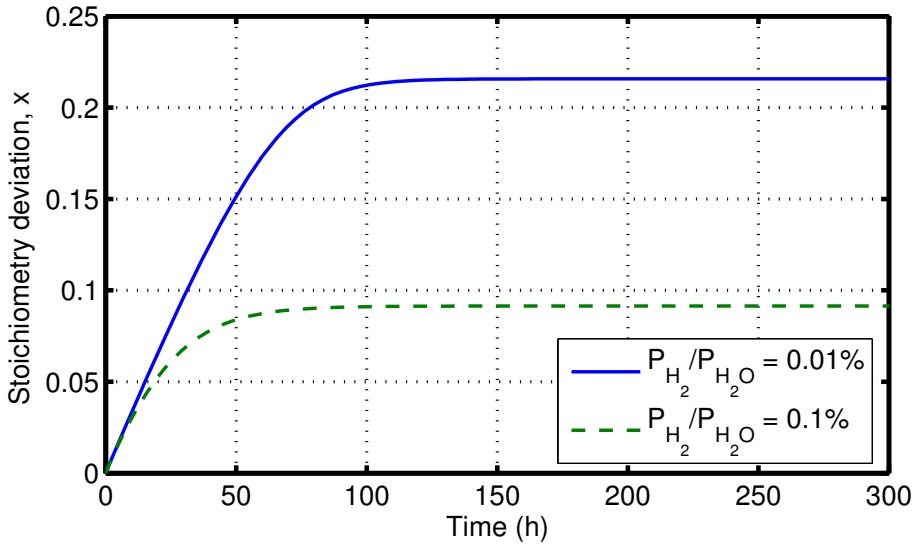

Figure 17: Oxidation of urania at 1400 K using input data in table 3 and the LBM.

A point worth noting is that a steady state, according to Eq. (28), may be reached before an equilibrium state can be attained. Meaning that, the right-hand side of Eq. (28) can become small (≈ 0), depending on temperature and pressure, despite the fact that the condition in Eq. (15) may not have yet been attained. This issue warrants further analysis.
We compare now the results of the model calculations with some experimental data. More specifically, we have selected the data by Cox *et al.* on O/U ratio versus time [14], which were obtained from tests conducted in pure steam of 1 atm at 1273 and 1473 K. The fuel surface-to-volume ratio (geometric) in these experiments was $S/V = 457$ m^{-1}. Figure 19 shows the data and model calculations at 1273 K. It is seen that, for this case, the empirical

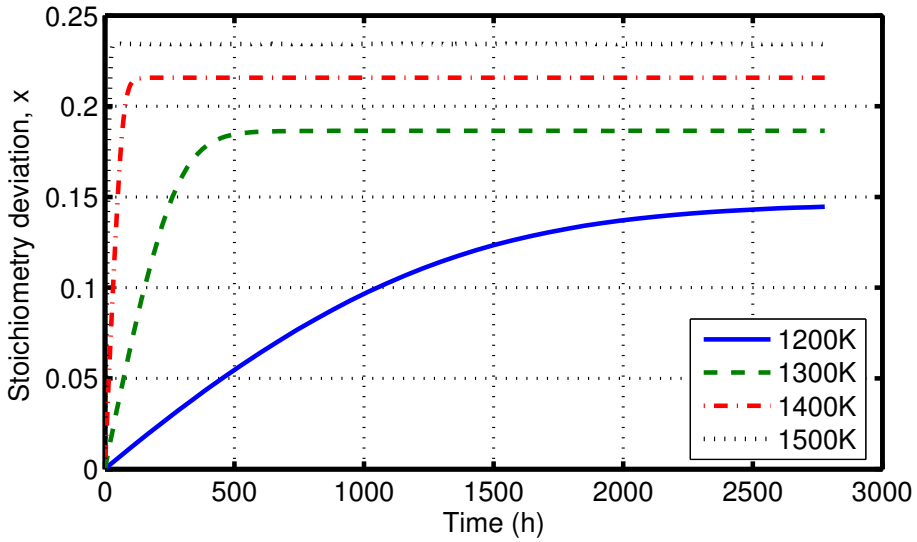

Figure 18: Oxidation of urania for $P_{\mathrm{H_2}}/P_{\mathrm{H_2O}} = 0.01\%$ using input data in table 3 and LBM.

Carter-Lay model results are much closer to the data than the results obtained from the LBM, which are way off. It is worthwhile to remark that $x_{eq} = 0.28$ for Carter-Lay, $x_{eq} = 0.25$ for LBM and $x_{eq} = 0.25$ from the experiment. However, the corresponding times are roughly 1000 h, 1000 h and 400 h, respectively. Figure 20 displays the data and model calculations at 1473 K. At this temperature, the retrodictions of both models are satisfactory, and the time to reach equilibrium is around 50 h.

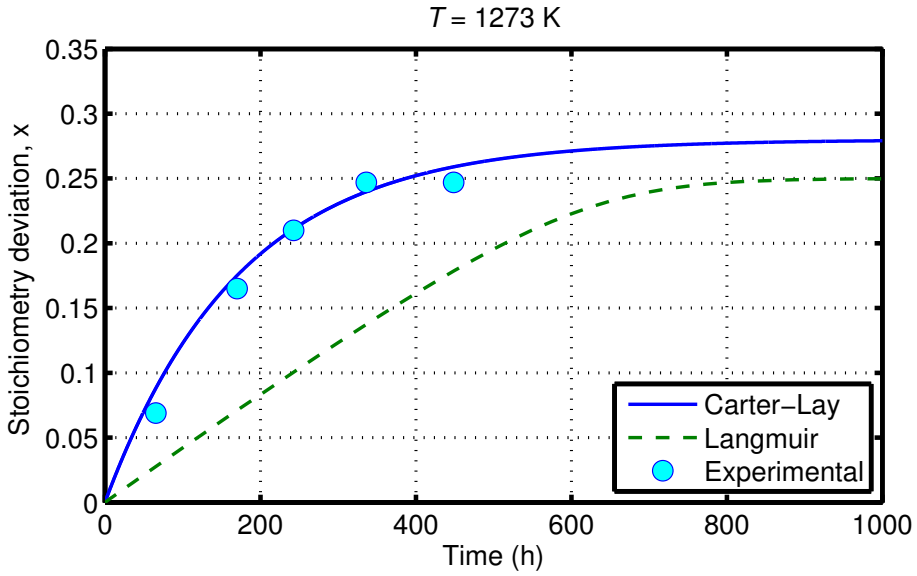

Figure 19: Oxidation of urania in steam at 1273 K, 0.1 MPa for $S/V = 457\ \mathrm{m}^{-1}$. Experimental data are from Cox *et al.* [14].

We finally examine the attributes of Olander's extended model (cf. section 2.2.2) against experimental data. Since Olander adjusted the three unknown parameters of the model to fit the experimental data of Abrefah *et al.* [15] for oxidation of UO_2 fuel in pure steam

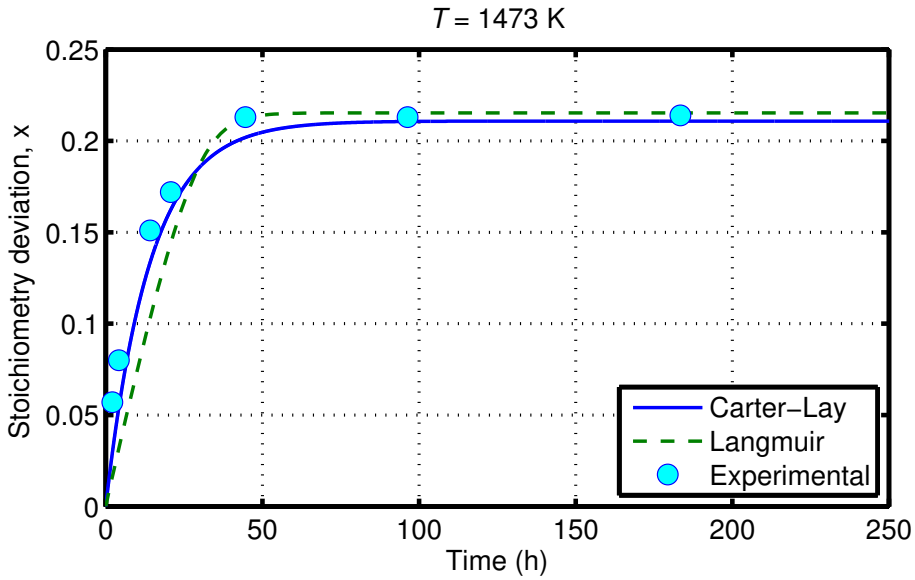

Figure 20: Oxidation of urania in steam at 1473 K, 0.1 MPa for $S/V = 457$ m^{-1}. Experimental data are from Cox *et al.* [14].

at 1623 K and atmospheric pressure, we restrict our comparison only to this case. The fuel surface-to-volume ratio in these experiments was $S/V = 3302.5$ m^{-1}. The results are presented in Fig. 21. As expected, Olander's model performs better against experimental data than the Carter-Lay model, because it is adjusted to do so. The Abrefah *et al.*'s curve is a fitting of data to a formula like Eq. (3).

The Olander model of fuel oxidation, presented in section 2.2.2, essentially contains three parameters, namely, a, k_s and the ratio γ/δ. As has been pointed out by Olander [20], there can be many combinations of these parameters that produce fits to the data as shown in Fig. 21. From the available database, the guidance for selecting the parameters is a correct calculation of the steam-pressure effect on the oxidation rate. Large values of aP_w and $\gamma/\delta P_w^{2/3}$ result in high surface coverage (θ_w, $\theta_{\rm O}$) and insensitivity of the oxidation rate to steam pressure. On the contrary, small values of these parameters lead to low coverage and prominent pressure effect. More comparisons of modeling outcomes with data and considerations to other approaches are needed to select the most suitable model for fuel oxidation.

2.3 Hydrogen production

The hydrogen production rate from fuel oxidation can be calculated by considering the overall oxidation reaction in Eq. (1). The atomic number density of oxygen in the fuel before oxidation is $N_{\rm O}^b = 2\rho_{\rm UO_2} N_A / M_{\rm UO_2}$ and after oxidation $N_{\rm O}^a = (2+x)\rho_{\rm UO_{2+x}} N_A / M_{\rm UO_{2+x}}$, where $\rho_{\rm UO_2}$ is density of fuel (kg/m^3), M the molecular weight (kg/mol) and N_A Avogadro's constant ($= 6.022 \times 10^{23}$ atom/mol). If the number of moles of the hyperstoichiometric fuel is equal to that of the uranium dioxide fuel, *i.e.*, $(\rho V/M)_{\rm UO_{2+x}} = (\rho V/M)_{\rm UO_2}$, where V is the volume of the fuel, the number of oxygen atoms consumed during fuel oxidation is given by

$$N_{\rm O}^{con} = x \frac{\rho_{\rm UO_2} V}{M_{\rm UO_2}} N_A. \tag{29}$$

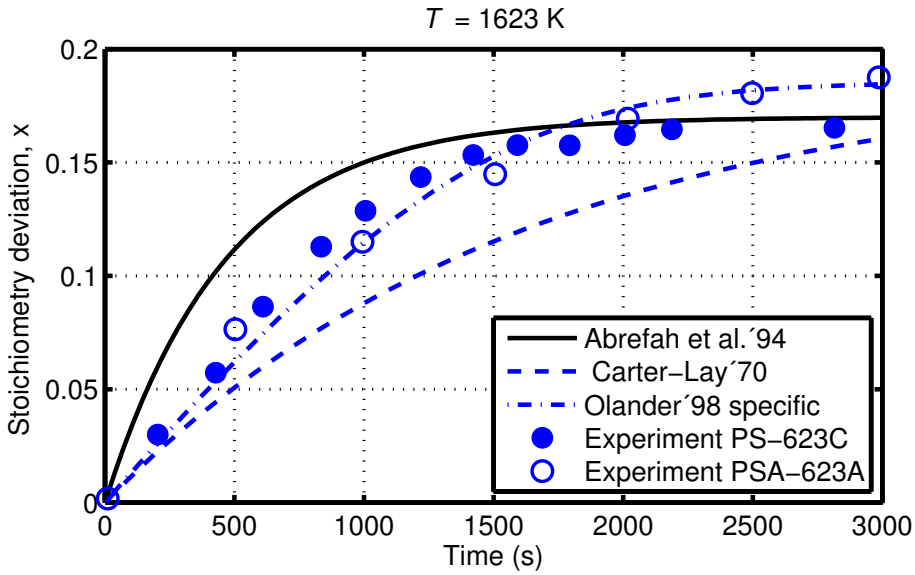

Figure 21: Oxidation of urania in steam at 1623 K, 0.1 MPa for $S/V = 3302.5$ m^{-1}. Experimental data are from Abrefah *et al.* [15].

Hence, the production rate of molecular hydrogen is

$$\mathscr{R}_{\mathrm{H_2}} = \Big(\frac{dx}{dt}\Big)\frac{\rho_{\mathrm{UO_2}} V}{M_{\mathrm{UO_2}}} N_A. \tag{30}$$

Finally, choosing an oxidation model for fuel (dx/dt), *e.g.*, the LBM kinetic Eq. (7), we write

$$\mathscr{R}_{\mathrm{H_2}} = \varrho S n_s k_a' \Theta\big[1 - \beta q(x)\big], \tag{31}$$

where $\beta = P_{\mathrm{H_2}}/P_{\mathrm{H_2O}}$ and $\varrho = \rho_{\mathrm{UO_2}} N_A/(\rho_{\mathrm{U}} M_{\mathrm{UO_2}})$. In Fig. 22 we have plotted $\mathscr{R}_{\mathrm{H_2}}/S$, assuming the design data for fuel rod listed in Table 3 at a fuel temperature of 1400 K. These calculations are shown for the hydrogen-to-steam ratios of $\beta = 0.0001$ and $\beta = 0.001$, respectively. Moreover, the equilibrium stoichiometry deviations x_{eq} are calculated according to the method described in section 2.2.1.

Table 3: Fuel rod (Zircaloy clad UO_2) design data.

Entity	unit	value
Fuel pellet diameter	mm	8.19
Fuel column length	mm	1200
Fuel surface-to-volume ratio	m^{-1}	488
Fuel density	kg/m^3	10500
Clad outer diameter	mm	9.62
Clad wall thickness	mm	0.63
Hot fuel-clad gap size	μm	13-25
Hot gas gap pressure	MPa	7.0

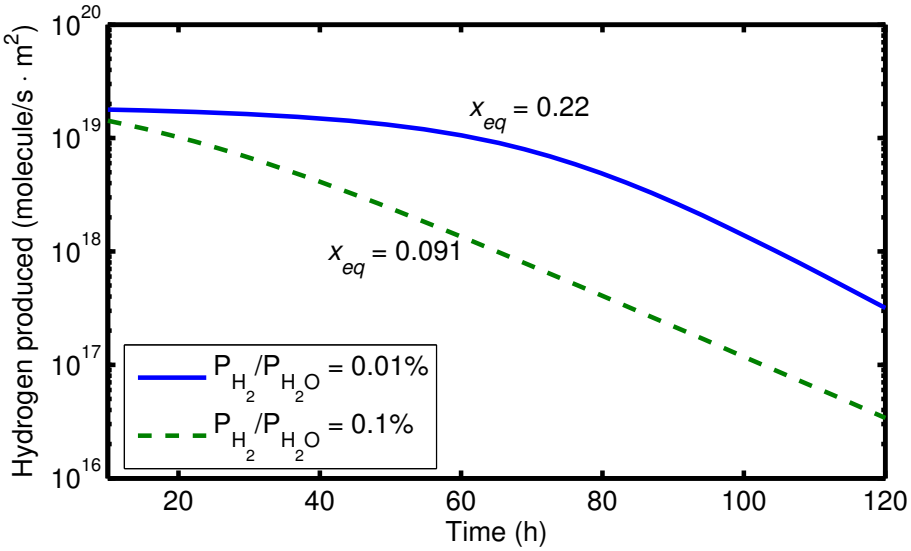

Figure 22: Calculated hydrogen production rate per unit area of fuel surface at 1400 K using the LBM and input data in table 3.

2.4 Remarks on oxidation kinetics

To recapitulate the concepts of this section, we recall that the rate of fuel oxidation is governed by the sum of the reaction rates of oxidation by steam and hydrogen peroxide and reduction by hydrogen. The thermodynamic models discussed in the foregoing subsections account for the contributions of steam and hydrogen reaction rates in the presence of a gas mixture of steam and hydrogen. The oxidation process levels off when the O/U ratio reaches equilibrium. The balance equation for oxygen in the fuel, cf. Eq. (7), may be re-expressed in the form

$$\frac{dx}{dt} = \frac{1}{\rho_{\mathrm{U}}}\frac{S}{V}\Big[R_{\mathrm{H_2O}} - R_{\mathrm{H_2}}\Big], \tag{32}$$

where

$$R_{\mathrm{H_2O}} - R_{\mathrm{H_2}} = f(T, P_{\mathrm{H_2O}})\left[1 - \sqrt{\frac{P_{\mathrm{O_2}}(x)}{P_{\mathrm{O_2}}}}\right], \tag{33}$$

and $f(T, P_{\mathrm{H_2O}})$ depends on the choice of adsorption isotherm. For example, in the LBM

$$f(T, P_{\mathrm{H_2O}}) = n_s k'_a \Theta(T, P_{\mathrm{H_2O}}) \tag{34}$$

with $k'_a = 2.48 \times 10^{10} \exp[-28105/T]$ s^{-1}, $n_s = 1.66 \times 10^{-6}$ mol m^{-2} and $\Theta(T, P_{\mathrm{H_2O}})$ (Langmuir isotherm) defined by Eq. (9).

Lewis *et al.* [32] have modified the Carter-Lay model (section 2.1) to explain high-pressure (> 1 atm) fuel oxidation data. They have introduced a Freundlich type adsorption isotherm [33] in Eq. (2) or Eq. (32)

$$R_{\mathrm{H_2O}} - R_{\mathrm{H_2}} = f(T, P_{\mathrm{H_2O}})\Big[1 - \frac{x}{x_{eq}}\Big], \tag{35}$$

$$f(T, P_{\mathrm{H_2O}}) = \rho_{\mathrm{U}} x_{eq} \alpha \sqrt{p_{\mathrm{H_2O}}}, \tag{36}$$

where ρ_{U}, x_{eq} and α were defined earlier and $p_{\mathrm{H_2O}}$ is the relative pressure of the steam with respect to the atmospheric pressure. We call this approach the CLF method after Carter, Lay and Freundlich.

Let us employ Eqs. (32), (35) and (36) to calculate fuel oxidation as a function of time in pure steam environment at atmospheric pressure (0.1 MPa) and 70 atm (7 MPa). For the reaction rate parameter α, we use Cox *et al.*'s relation (table 1); and we calculate x_{eq} by the method outlined in appendix A.2 and the Lindemer-Besmann partial pressure relation (appendix A.1). This gives $x_{eq} = 0.228$ and $x_{eq} = 0.271$ for $p_{\mathrm{H_2O}} = 1$ and $p_{\mathrm{H_2O}} = 70$, respectively. The results of our calculations for a fuel sample with $S/V = 488.4$ m^{-1} are displayed in Fig. 23. This figure can be compared with the outcome of our earlier calculations with the Langmuir approach depicted in Fig. 16. It is seen that the CLF method predicts a much stronger pressure dependence than the Langmuir based model at 1400 K.

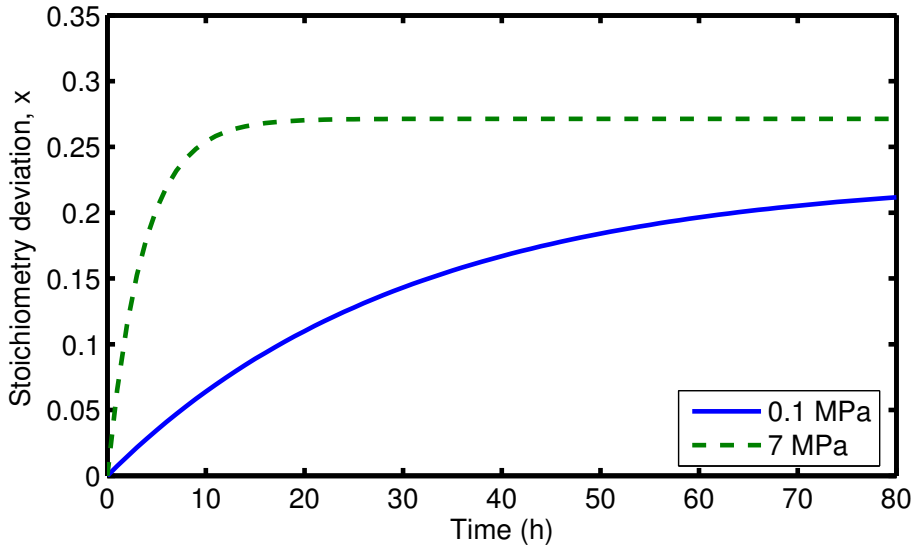

Figure 23: Oxidation of urania in steam at 1400 K for $S/V = 488.4$ m^{-1} using the CLF method.

As may have noted from the preceding sections, an important parameter characterizing the oxidation kinetics of UO_2 is the characteristic time or relaxation time of oxidation. It indicates the time needed for the O/U ratio to reach its equilibrium value during the oxidation process. This parameter is a strong function of temperature but also depends on the surface-to-volume of specimen and the surrounding gaseous environment. The relaxation time may be expressed in terms of the surface-exchange coefficient α as

$$\tau_c = \frac{1}{\alpha(T)}\left(\frac{V}{S}\right). \tag{37}$$

Imamura and Une [17] have determined, through measurements, the activation energy and the pre-exponential factor for α (unirradiated UO_2) in both pure steam and in 10 vol% H_2O_2/H_2O atmosphere; see Table 1. Figure 24 shows plots of τ_c as a function of temperature for three values of S/V: 500, 5000, and 50 000 m^{-1} using Imamura-Une's α values for the 10 vol% H_2O_2/H_2O atmosphere. For example for $S/V = 5000$ m^{-1}, $\tau_c = 1493$ s at 1473 K and $\tau_c = 460$ s at 1623 K.

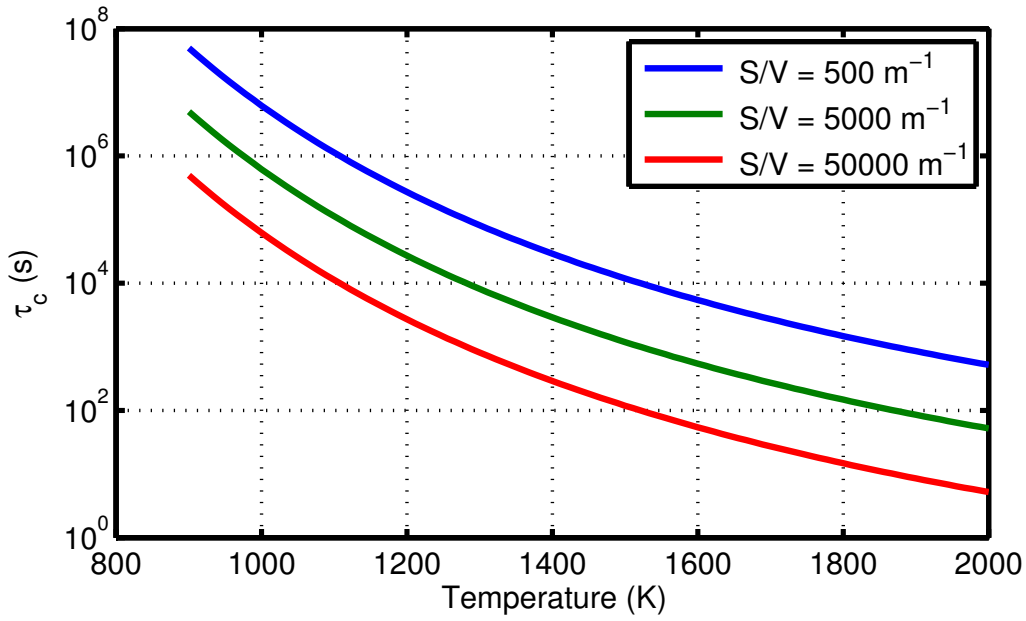

Figure 24: Calculated characteristic time τ_c for UO_2 oxidation in 10 vol% H_2O_2/H_2O atmosphere as a function of temperature for several surface-to-volume (S/V) ratios.

During reactor operation (steady-state or transient condition), the urania pellet in a fuel rod is under temperature gradient. Excess oxygen ions, x in UO_{2+x}, thereby experience both concentration and thermal gradients, *i.e.*, they will be subject to thermal diffusion. Thus extending and combining Eqs. (32), (35) and (36), one may describe the time evolution of oxygen concentration $x = x(\mathbf{r}, t)$ in dilute solid solution across fuel pellet by

$$\frac{\partial x}{\partial t} = \nabla \cdot \Big[D_x \Big(\nabla - \frac{\nabla T}{\eta} \Big) \Big] x, \tag{38}$$

where D_x the diffusivity of oxygen, $\eta = k_B T^2 / Q(x)$, and $Q(x)$ is the oxygen heat of transport. A Neumann type boundary condition is imposed at the center of the pellet ($r = 0$) due to symmetry, namely

$$\frac{\partial x(r,t)}{\partial r} \Big|_{r=0} = 0, \quad t > 0. \tag{39}$$

At the surface of the pellet, the stoichiometry $x(r = a)$ is put equal to the value of x which is established due to an equilibrium between the solid fuel and the gap atmosphere, where a solution of Eq. (32) is [cf. Eq. (3)]

$$x = x_{eq} \Big(1 - \exp[-\alpha \sqrt{p_{\mathrm{H_2O}}} (S/V) t] \Big), \quad r = a,\ t > 0. \tag{40}$$

Indeed, because of the lower temperature at the fuel pellet surface, the fuel may remain stoichiometric at that location, *i.e.*, $x \approx 0$ at $r = a$, $t > 0$. Thermal diffusion of oxygen in fuel pellet is further discussed in section 3.

From our review, we note that the various models of UO_2 oxidation predict different kinetic behaviors and also yield different equilibrium stoichiometry deviations. Nevertheless, it

seems that the Carter-Lay-Freundlich approach is promising and can be considered for code implementation after more verifications with the aforementioned experimental data.

2.5 Remarks on the U-O system phase diagram

The stable phase of uranium dioxide for all temperatures up to around the melting point ($T_m = 3120$ K) possesses the fluorite crystal structure. UO_2 in the solid state consists of U^{4+} and O^{2-} ions. The oxygen ions are arranged on a simple cubic lattice and the U^{4+} ions form an fcc sublattice as confirmed by X-ray diffraction data [1]. To be more specific, between 30 K and ≈ 3000 K UO_2 has the space group symmetry $Fm\bar{3}m$; however see [34]. When UO_2 is oxidized, no extra lines are observed in X-ray powder diffraction pattern until the composition U_4O_9 is reached [1]. Up to that point UO_{2+x} consists of a solid solution of excess oxygen atoms in the fluorite matrix of UO_2. It exists as a single phase at low values of x for temperatures above 300°C. As the oxygen content increases the temperature at the phase boundary rises towards 1200°C, Fig. 25. According to Willis [1] there is no evidence for the formation of uranium vacancies upon oxidation, *i.e.* uranium sublattice remains intact between UO_2 and U_4O_9, and oxidation proceeds by the merger of additional oxygen atoms at the interstitial sites in the fluorite lattice. Oxidation of UO_2 and the development of UO_{2+x}, U_4O_{9-y}, U_3O_7, and U_3O_8 have been recently measured by neutron diffraction [3, 4] and evaluated by means of density functional theory [35].

In more detail, the crystal structure of UO_2 (up to $UO_{2.25}$) consists of three interpenetrating fcc lattices, a uranium ion being at the origin and the oxygen ions at $(1/4, 1/4, 1/4)a$ and $(3/4, 3/4, 3/4)a$, where a is the cubic lattice constant with the fcc space group symmetry $Fm\bar{3}m$ [1, 36]. In contrast for α-U_4O_9, X-ray, neutron and electron diffraction studies have led to the conclusion that this compound has the bcc space group symmetry $I\bar{4}3d$ with a lattice parameter nearly four times that of UO_2 [1, 37]. Further oxidation of U_4O_9 leads to U_3O_8. This compound, α-U_3O_8, is orthorhombic with the space group symmetry *C2mm*, but at high temperatures ($T \geq 623$ K) is described by a simpler hexagonal unit cell with the space group symmetry $P\bar{6}2m$ and unit cell sizes $a = 6.72$ Å , $b = 11.96$ Å and $c = 4.15$ Å [3, 4, 38, 39]. For space group notations, see *e.g.* [5] or the online `Wikepedia` *List of space groups*.

The phase diagram of the U-O system has been a subject of numerous past and recent studies, *e.g.* [40, 41, 42, 43, 44, 45, 30]. Figure 25 shows a U-O phase diagram with superimposed curves of constant oxygen pressure from the thermodynamic evaluation of Naito and Kamegashira [41]. Our calculations in the foregoing subsections show that for pure steam at 1400 K and 1 atm pressure, the equilibrium O/M ≈ 2.2 (cf. Fig. 16); which according to Fig. 25, the fuel is in the single-phase UO_{2+x} region. On cooling to low temperature, say ≤ 600 K, the high-temperature single-phase decomposes to a mixed UO_{2+x}+ U_4O_{9-y} phase. On the other hand, for pure steam at 1400 K and 70 atm pressure, the equilibrium O/M ≈ 2.6. In this condition the fuel is in the two-phase UO_{2+x}+U_3O_{8-z} region. If cooled from this point (O/M=2.6, 1400 K), the low temperature fuel structure should lie in the U_3O_7+U_5O_{13} border region.

We should mention that in the Chalk River in-reactor steam oxidation tests (at 1063 K, 10.5 MPa) the higher oxide phase U_3O_8 has been observed in cracks near the periphery of fuel pellets along the grain boundaries according to Lewis [46, 47]. As can be checked from a binary phase diagram of the uranium-oxygen system, Fig. 25, this corresponds to an equilibrium oxygen-to-uranium ratio somewhere between 2.6 and 2.7.

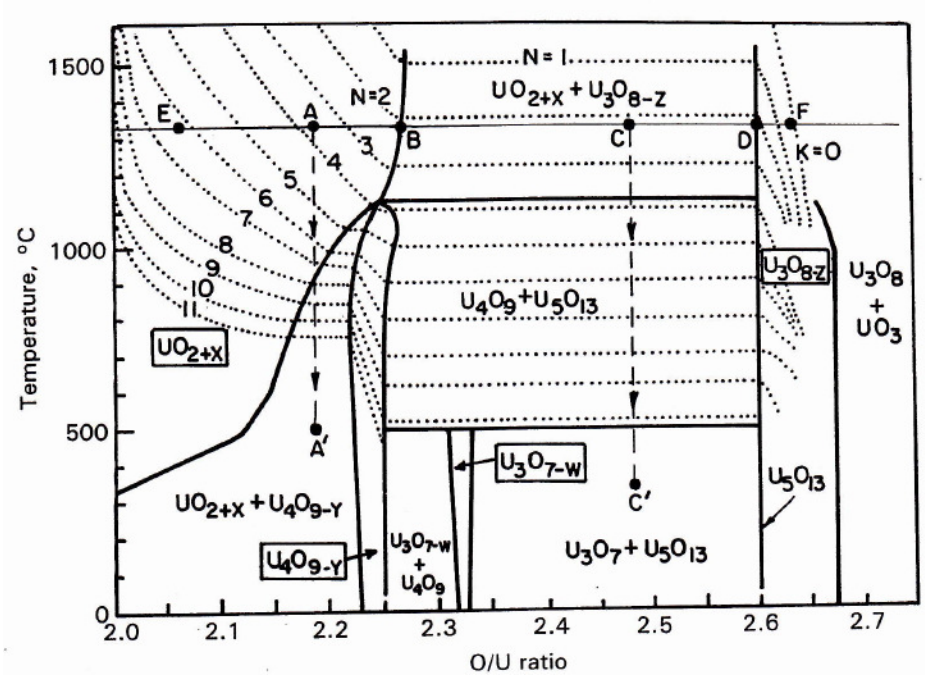

Figure 25: A portion of the binary phase diagram of the U-O system with oxygen pressure isobars superimposed. The isobars are shown by the index N in $P_{O_2} = 10^{-N}$ where P_{O_2} is in atm; from [41].

3 Oxygen thermal diffusion in UO_{2+x} fuel pellet

3.1 Observational and phenomenology

During reactor operation, fission process in UO_2 produces oxygen among other elements. Some of the produced oxygen can combine with metallic fission products (Zr, Nb, Y, rare earths, etc.) to form oxides. However, not all fission products take up oxygen. The excess oxygen dissolves in the fuel matrix whereupon it elevates the valence of the uranium. Hence, the net effect of burnup is to make the UO_2 fuel more hyperstoichiometric than the fresh fuel and to elevate the oxygen potential of the fuel [48].

For example, when a trivalent ion (fission product) such as La^{3+} enters "substitutionally" UO_2, after replacement of U^{4+} ions by cations of valence 3^+, to maintain the local charge balance, an oxygen ion may be removed from the lattice, thereby producing an anion (oxygen) vacancy in the lattice. Alternatively, electrical neutrality of the crystal is preserved without removal of an oxygen ion by the oxidation of two uranium ions from U^{4+} to U^{5+} or by oxidation of one U^{4+} to U^{6+}. The choice between the routes depends on the operating oxygen potential of the environment. The latter route can occur when the oxygen potential is sufficiently large [48].

The stoichiometry of urania in LWR fuel rods, which had experienced relatively high powers during their irradiation histories, has been estimated by Kleykamp [49]. The shift in the pellet average oxygen/metal ratio was found to be $\overline{\chi}_0 \equiv \Delta(\mathrm{O/M}) \approx 1.4{\times}10^{-4}$/(MWd/kgU) according to Kleykamp's assessment [49]. For example, at a pellet average burnup of about 43 MWd/kgU, $\Delta(\mathrm{O/M}) \approx 0.006$. Kleykamp, however, points out that in high-powered rods this excess oxygen may be released from the fuel and completely absorbed by Zircaloy cladding, thereby resulting in $\mathrm{O/M} \approx 2.00$ during irradiation [49].

In a post-irradiation examination of a test fuel rod (fuel stack length, 827 mm) with a burnup of about 43 MWd/kgU, which was subjected to a power transient in the Risø test reactor (Denmark) after a base-irradiation in a BWR, Walker and Mogensen [50] determined the stoichiometry of a fuel pellet from lattice constant using X-ray diffraction. They observed oxygen redistribution across the pellet, namely at radial positions $r/a = 0.96$ and $r/a = 0.27$ (a being pellet radius), the oxygen-to-uranium ratios were found to be $\mathrm{O/U} = 2.00 - 2.01$ and $\mathrm{O/U} = 2.20 \pm 0.05$, respectively.

A more recent evaluation of oxygen stoichiometry shift of high burnup LWR fuels, mainly from the available galvanic (electromotive force) method data by Spino and Peerani [51], clearly indicates that the aforementioned Kleykamp's relation holds, provided there is no internal oxidation of Zr-alloy cladding. So for a fuel with a burnup of 100 MWd/kgU, $\Delta(\mathrm{O/M}) \approx 0.014$ in the absence of any Zr-alloy oxidation. They conclude, however, that even in the presence of internal cladding oxidation, at burnups around 80 MWd/kgM and beyond, the fuel tends to become progressively slightly hyperstoichiometric and the maximum O/M ratios reached at a burnup of 100 MWd/kgM would be $\approx 2.001 - 2.002$. They attribute this to the stagnation of the oxygen uptake by the cladding and that of the fission product Mo.

The aforementioned studies [49, 50, 51] dealt with the oxidation of fuel of an intact rod as a result of fission process, not due to the breach of the cladding and/or the inflow of water/steam into the rod as discussed in the preceding section. Despite the thorough evaluations carried out in [49, 51], the number of fuel rods examined were quite limited, considering a plethora of situations and scenarios that LWR fuel rods may experience during reactor service or under upset conditions.

Early experiments on oxygen redistribution on hypostoichiometric MOX (mixed oxide) fuels, *i.e.* (U,Pu)O_{2-x}, made by Evans, Aitken and Craig [52], confirmed that oxygen was transported to the fuel regions with lower temperatures. ln these experiments, solid state thermal diffusion and gas phase transport of oxygen, via the carrier gases H_2O and CO_2, occur simultaneously in the solid matrix and in the surrounding gap of the MOX fuel pellets. Aitken [53] developed a model of oxygen thermal transport, specially applicable to pellets with cracks and channels of interconnected porosity. Sari and Schumacher (Transuranium Institute, Karlsruhe) conducted out-of-reactor tests to study the oxygen redistribution in MOX fuel pellets exposed to a thermal gradient [54]. They showed that in hyperstoichiometric fuel, oxygen migrates towards the high temperature region of the pellet whereas in hypostoichiometric fuel, oxygen migrates in the opposite direction. The oxygen transport was explained based on solid-state thermal diffusion that takes place via vacancies and interstitials. They determined the heats of oxygen transport, which for hyperstoichiometric oxides is a function of uranium valence and temperature.
In this section, we assess the existing models for the excess oxygen redistribution in hyperstoichiometric urania pellet, *i.e.* UO_{2+x} due to thermal diffusion by disregarding the so-called oxygen "gettering" effect of Zr-alloy cladding. The phenomenon of oxygen redistribution is important technologically due to its possible impact on fuel behavior, which yields a measurable increase in the diffusivity of fission product gases and a reduction in fuel thermal conductivity, thereby a tangible increase of fission gas release of hyperstoichiometric urania fuel as compared to stoichiometric fuel. Early modeling efforts include [55, 56, 57] and more recent computations in [30, 58, 59, 60].

3.2 Mass transfer along temperature gradient

Thermal diffusion of oxygen interstitials in the hyperstoichiometric mixed oxides, can be described using flux equations obtained from the thermodynamics of irreversible processes. Classical treatises describe the well-known process [61, 62]. A detailed account of the basic phenomenological equations in a temperature gradient can be found in [63]. We consider the surplus oxygen ions in the UO_2 lattice as interstitials with their flux expressed by

$$J = L_i X_i + L_q X_q. \tag{41}$$

Here, X_i is the thermodynamic force acting on the oxygen interstitial, X_q is the thermodynamic force arising from the temperature gradient and the coefficients L_i and L_q are related to the diffusion coefficient and the heat of transport, respectively, as will be delineated below.
The thermodynamic force acting on the oxygen interstitial is simply proportional to the gradient of the chemical potential or the concentration of the diffusing species, namely

$$X_i = -N_{\mathrm{O}} \nabla c_i, \tag{42}$$

where N_{O} is the total number of oxygen atoms per unit volume and c_i is the atomic fraction of interstitial atoms, which is related to the deviation from stoichiometry. For a hyperstoichiometric UO_{2+x} fuel, $c_i = x \equiv \mathrm{O/U} - 2$. Moreover, the coefficient $L_i = D_x$ is the diffusion coefficient of the oxygen in the UO_2 matrix. The thermodynamic force X_q in Eq.

(41) may be written as

$$X_q = -N_{\mathrm{O}} \frac{\nabla T}{T}, \tag{43}$$

and the corresponding coefficient

$$L_q = D_x \, x \Big(1 + \frac{\partial \ln \gamma}{\partial \ln x}\Big)^{-1} \frac{Q}{k_B T}, \tag{44}$$

where Q is the heat of transport and γ denotes the activity coefficient. In dilute solid solution limit Eq. (44) is simplified to (see, *e.g.* [54, 63])

$$L_q \approx D_x \, x \frac{Q}{k_B T}. \tag{45}$$

Substituting Eqs. (42) to (45) into Eq. (41), we obtain

$$J = -N_{\mathrm{O}} D_x \Big(\nabla x + x \frac{Q}{k_B T^2} \nabla T\Big). \tag{46}$$

Invoking the law of conservation of mass, we write

$$N_{\mathrm{O}} \frac{\partial x}{\partial t} = -\nabla \cdot J, \tag{47}$$

where the variable $x = (r, t)$ can be evaluated as a function of the time t and the radial coordinate r. Solution to Eq. (47) yields the time dependent concentration profile for oxygen interstitials, provided the radial temperature gradient is known, which needs to be determined from the heat equation.
In the section that follows, we give solutions to Eq. (47), assuming axial symmetry, from which the oxygen profile across fuel pellet is calculated for given temperature profiles, which were computed separately.

3.3 Oxygen redistribution

In this section, a method and an application of oxygen redistribution during steady states and transient power changes will be discussed. The source for this approach, which I follow closely, is a paper presented in an IAEA conference in 1994 [57]. A numerical treatment of the problem was presented earlier by Lassmann in 1987 [56].
Assuming axial invariance and neglecting the axial temperature variation in the fuel, Eq. (47) in radially symmetric cylindrical coordinates becomes

$$\frac{\partial \chi}{\partial t} = \frac{1}{r} \frac{\partial}{\partial r} \Big[r D_x \Big(\frac{\partial}{\partial r} - Q(\chi) \frac{\partial \beta}{\partial r} \Big) \Big] \chi, \tag{48}$$

where $\beta \equiv (k_B T)^{-1}$ is the inverse temperature and $\chi(r, t) \equiv x(r, t)$. This equation is the same as Eq. (38), conferred in the foregoing section, in the radial direction.
Equation (48) is accompanied with a Neumann type boundary condition, which implies that the flux of oxygen interstitials is prescribed at the boundaries of the fuel pellet. Supposing a quasi-equilibrium situation, the flux of the oxygen interstitials can be set to a constant

value or zero at the boundaries, namely

$$\frac{\partial \chi}{\partial r} = \frac{\partial \beta}{\partial r} Q(\chi)\chi, \quad \text{at} \quad r = a, r = b, \tag{49}$$

where $r = a$ and $r = b$ are the outer and the inner hollow cylinder radii, respectively, and in case of a solid cylinder where $b = 0$, $\partial\chi/\partial r = 0$.

3.3.1 Steady-state solution

Let us first evaluate a steady-state solution of Eq. (48), denoting by $\chi(r,t) = \tilde{\chi}_0$ corresponding to $t \to \infty$. We write using Eq. (49)

$$\frac{\partial \tilde{\chi}_0}{\partial r} = Q(\tilde{\chi}_0)\tilde{\chi}_0 \frac{\partial \beta}{\partial r}, \quad \text{at} \quad r = a, r = b. \tag{50}$$

The heat of transport of oxygen, for the problem under consideration, has an exponential form $Q(\tilde{\chi}_0) = Q_0 \exp(-c_0\tilde{\chi}_0)$ according to [54], where Q_0 and c_0 are material dependent constants, see Table 4. The exact steady-state solution of Eq. (50) for this form of $Q(\tilde{\chi}_0)$ can be expressed in terms of the exponential integral, viz.

$$\mathrm{Ei}[c_0\tilde{\chi}_0(r)] = a_0 + Q_0\beta(r), \tag{51}$$

where $\mathrm{Ei}[x] = -\int_{-x}^{\infty} \frac{e^{-t}}{t} dt$ and

$$a_0 = \mathrm{Ei}[c_0\tilde{\chi}_0(0)] - Q_0\beta(0). \tag{52}$$

The transcendental Eq. (51) only provides an implicit expression for $\tilde{\chi}_0$, which needs to be solved numerically. In [57] several approximations to $Q(\tilde{\chi}_0)$ were examined. The best explicit approximation was a Padé approximant [64], which offered a close form solution and matched the exact solution unequivocally, namely

$$Q(\tilde{\chi}_0) \approx Q_0 \frac{1 - c_0\tilde{\chi}_0/2}{1 + c_0\tilde{\chi}_0/2}. \tag{53}$$

The solution in this case reads

$$\tilde{\chi}_0(r) = \frac{2}{c_0}\Big[1 - \frac{2}{1 + \sqrt{1 + a_2 \exp[\beta(r)Q_0]}}\Big], \tag{54}$$

where a_2 is a constant given as

$$a_2 = \frac{2c_0\ \tilde{\chi}_0(0) e^{-\beta(0)Q_0}}{[1 - c_0\tilde{\chi}_0(0)/2]^2}. \tag{55}$$

Numerical computations Here we present sample computations of $\tilde{\chi}_0(r)$, *i.e.* the excess oxygen to metal ratio (O/M), across a cylindrical solid pellet using Eq. (54). To this end, we need information on temperature distribution across the pellet, which can be calculated by a fuel rod modeling code, and the excess O/M ratio at the pellet center $\tilde{\chi}_0(0)$. Using the data specified in [57] and shown in Table 5. *i.e.* the fuel central temperature

Table 4: Material property formulae with dependence on temperature T (K) and/or stoichiometry x. The range of applicability of x and T is also indicated.

Property/parameter	Units	Source
$Q = -3.5 \times 10^{34} \exp(-17 V_{\rm U})$	$\rm Jmol^{-1}$	[54]
$V_{\rm U} = 4 + 2x$	-	-
$D_x = 1.39 \times 10^{-6} \exp(-9128.5/T)$	$\rm m^2 s^{-1}$	[56]
$D_x = 2.50 \times 10^{-4} \exp(-16400/T)$	$\rm m^2 s^{-1}$	[65]
$10^{-5} \leq x \leq 0.1$	$700 \leq T \leq 1800$ K	[65]
$N_A = 6.022 \times 10^{23}$	$\rm mol^{-1}$	Avogadro #

and surface temperature, corresponding to different irradiation times (fuel burnups) for a given fuel rod power history and the pellet-average shift in oxygen concentration, the latter is estimated from $\overline{\chi}_0 \equiv \Delta(\rm O/M) \approx 1.4 \times 10^{-4}$/(MWd/kgU) according to [66]. Fuel temperatures computed at two burnups are fitted to a parabolic equation as a function of pellet radius: $T(r) = T(0) + (r/a)^2\big[T(a) - T(0)\big]$, see Fig 26(a). This relation and the data in Table 5 are used as input to Eq. (54) in order to compute $\tilde{\chi}_0$ across pellet.

Table 5: Fuel pellet temperature data and average excess oxygen [57].

Fuel burnup	LHGR	$T(r=0)$	$T(r=a)$	$\Delta(\rm O/M)$
MWdkgU	kW/m	K	K	-
20	21	1194	732	0.0028
40	16	1012	695	0.0056

LHGR = linear heat generation rate.

The foregoing formula derived for the computation of $\tilde{\chi}_0(r)$ requires as input $\tilde{\chi}_0(0)$ not $\overline{\chi}_0$. However, these two quantities are related through

$$\overline{\chi}_0 = \frac{2}{a^2} \int_0^a \tilde{\chi}_0(r) r dr, \tag{56}$$

where the integration can be carried out numerically.
Using the Padé approximant solution and the data in Tables 4 and 5, we have computed $\tilde{\chi}_0(r)$ as a function of r/a at the two considered burnups, see Fig. 26(b). It is seen that the deviation in stoichiometry peaks at the center where the fuel pellet is hottest. At the fuel surface the fuel is nearly stoichiometric, *i.e.* $\tilde{\chi}_0(a) \approx 0$.
We should note that in the temperature profile computations depicted in Fig. 26(a) the effect of stoichiometry deviation was not taken into account, since fuel thermal conductivity in the heat equation was assumed to be independent of the O/U ratio, *i.e.* the expression for O/U = 2.00 was used. Accounting for this dependence can rise the fuel central temperature considerably at higher values of O/U ($\geq$ 2.03); see *e.g.* [67]. The thermal conductivity of hyperstoichiometric UO_{2+x} and its dependence on $x = \rm O/U - 2.00$ are detailed in Appendix C.

3.3.2 Transient solution

By transient condition, we mean the case where both fuel temperature and oxygen concentration are under rapid time variation, *i.e.* shorter than their respective time constants. Let

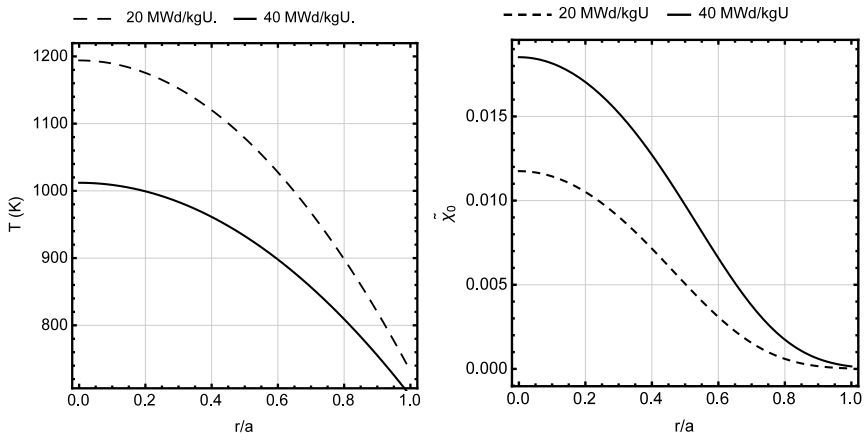

(a) (b)

Figure 26: (a) Radial temperature profiles across fuel pellet at two different burnups. (b) Radial distribution of the deviation from stoichiometry for UO_2, $\tilde{\chi}_0(r/a)$, as a function of normalized pellet radius, r/a.

us rewrite Eqs. (48) and (49) in temperature explicit forms

$$\frac{\partial \chi}{\partial t} = \frac{1}{r}\frac{\partial}{\partial r}\Big[rD_x\Big(\frac{\partial}{\partial r} + \frac{Q(\chi)}{k_B T^2}\frac{\partial T}{\partial r}\Big)\Big]\chi, \tag{57}$$

$$\frac{\partial \chi}{\partial r} + \frac{Q(\chi)\chi}{k_B T^2}\frac{\partial T}{\partial r} = 0, \quad \text{at} \quad r = a, r = b, \tag{58}$$

where the temperature $T(r,t)$ is determined from the heat equation

$$\rho C_p \frac{\partial T}{\partial t} = \frac{1}{r}\frac{\partial}{\partial r}\Big(r\kappa_{\rm th}(T,\chi)\frac{\partial T}{\partial r}\Big) + \mathscr{Q}(r,t). \tag{59}$$

Here as usual, ρ is the mass density, C_p the constant pressure heat capacity, $\kappa_{\rm th}$ (function of T and χ) is the thermal conductivity and $\mathscr{Q}(r,t)$ is the heat generation rate per unit volume. Equation (59) is followed by an appropriate boundary condition $\partial T/\partial r = 0$ at $r = 0$ and T_s at $r = a$, where T_s is the fuel surface temperature. A polynomial type expression for temperature and non-stoichiometry dependence of C_p is provided in [30]. Models for $\kappa_{\rm th}$ of UO_{2+x} are outlined in Appendix C.

Lassmann [56] has argued that the solution to this complicated transient problem, *i.e.* Eqs. (57) - (58), can be approximated by

$$\chi(r,t) = \tilde{\chi}_0(r) + \big[\chi(r,t_0) - \tilde{\chi}_0(r)\big]e^{-(t-t_0)/\tau} \tag{60}$$

where $\chi(r,t_0)$ is solution at the start-time of transient t_0, $\tilde{\chi}_0(r)$ is the steady-state solution, *e.g.* Eq. (54), and τ is the diffusive time constant. Furthermore, Lassmann [55, 56] estimated that τ is limited by

$$\frac{r_{\rm eq}^2}{31 D_x} \le \tau \le \frac{r_{\rm eq}^2}{5.8 D_x} \tag{61}$$

where $r_{\rm eq} = \sqrt{a^2 - b^2}$ or in case of solid fuel pellet $r_{\rm eq} = a$. The average value of τ is given by $\tau_{\rm av} = r_{\rm eq}^2/17.2 D_{\rm av}$, where $D_{\rm av} \equiv D_x(T_{\rm av})$ and $T_{\rm av} = (T(a) + T(b))/2$.

Solutions (60)-(61) are flawed, or at best crudely simplistic, since τ does not account for

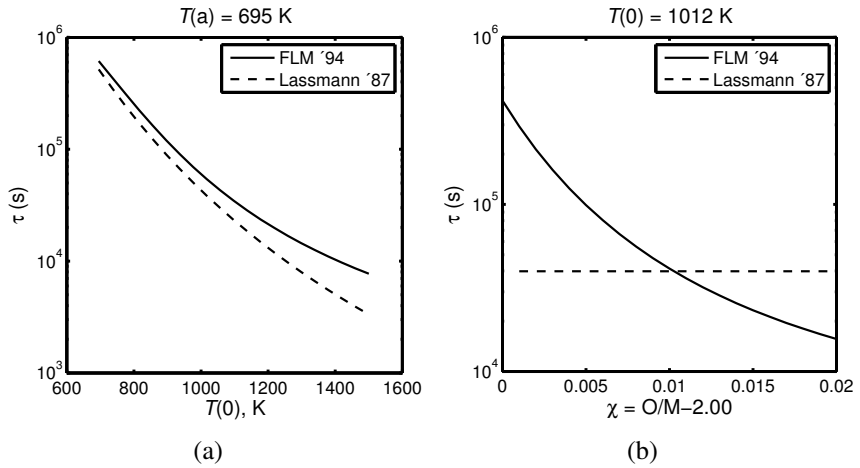

Figure 27: Computations of thermal diffusion time constant by methods of FLM [57] and Lassmann [56] versus: (a) Central fuel temperature at a const. surface temperature 695 K. (b) oxygen concentration at a fixed central temperature of 1012 K and $\overline{\chi}_0 = 0.0056$.

the heat of transport Q, which is a function of χ (in principle sets it to zero), and thereby Eq. (60) does not satisfy the conservation of mass for χ. In [57] a more appropriate approximate solution is provided, which accounts for the dependence of the time constant on Q, but still allows us to use equation of type (60) as an asymptotic solution. The method converts Eqs. (57)-(58) to a Sturm-Liouville eigenvalue problem and determines the smallest eigenvalue numerically, which yields the leading term for the time constant τ. This method is presented in Appendix B.

Figure 27 depicts the time constant as calculated by the method in [57], designated here as FLM'94, vs. that used by Lassmann [56]. The diffusion coefficient used for oxygen is as in [56] given in Table 4. It is seen that as the temperature is increased, the deviations between the two methods is increased, where the FLM method predicts a larger time constant. Moreover, the FLM time constant is oxygen concentration dependent. As can be seen, for the case under study, the time constant will be an order of a few hours at the central fuel temperature of ≈ 1500 K (≈ 1200°C). However, as fuel temperature increases beyond 1600 K, the time constant can reach orders of tens of minutes. More computations under different pertinent conditions are needed to provide better estimations. In addition, benchmarks with full numerical solution of Eq. (57) is necessary.

3.4 Remarks on oxygen diffusion coefficient

In our computation, we have used the oxygen diffusion coefficient attributed to Matzke as stated in [56]; see Table 4. However, the underlying background for this relation is not given in [56]. Meachen in 1989 made a good literature review of oxygen diffusion in uranium dioxide [65] and came out with an expression, which we have also listed in Table 4. Figure 28 compares the Matzke versus Meachen oxygen diffusion coefficient as a function of temperature. It is seen that Matzke's expression predicts higher diffusivites for temperatures below 1400 K than Meachen's and vice versa for $T > 1400$ K.

Fifteen years later in 2004, Ruello and coworkers [68] reported oxygen diffusivity data on UO_{2+x} using electrical conductivity measurements. Analysis of their data indicates that the activation energy for diffusion depended on the range of x, namely 0.85 eV for

$x \leq 0.03$, while 1.08 eV for $0.07 \leq x \leq 0.17$ in the temperature range $1273 - 1673$ K, which they extrapolated to 2000 K. That is, they found that the oxygen diffusion coefficient is a decreasing function of the departure from stoichiometry, while the data reported in the literature is an increasing function in the same range of departure from stoichiometry. Ruello et al. attributed this behavior for $x < 0.07$ to the presence of the singly ionized Willis clusters, while for $x \geq 0.07$ to more complex defect aggregates,[3] however with no concrete evidence; for the details see [68].
From the diffusivity data presented in figure 4 of [68] one can extract two diffusion coefficients depending on the deviation from stoichiometry. These we have plotted in Fig. 28 below. As can be seen, Ruello et al's diffusion coefficient for $0.07 \leq x \leq 0.17$ is more than an order of magnitude lower than the values for $x \leq 0.03$ and those recommended by Matzke and Meachen. There is, however, a gap in Ruello et al's data between $x = 0.03$ and $x = 0.07$. It is not clear where and how this transition would occur between the two drastically different levels of oxygen diffusivity.

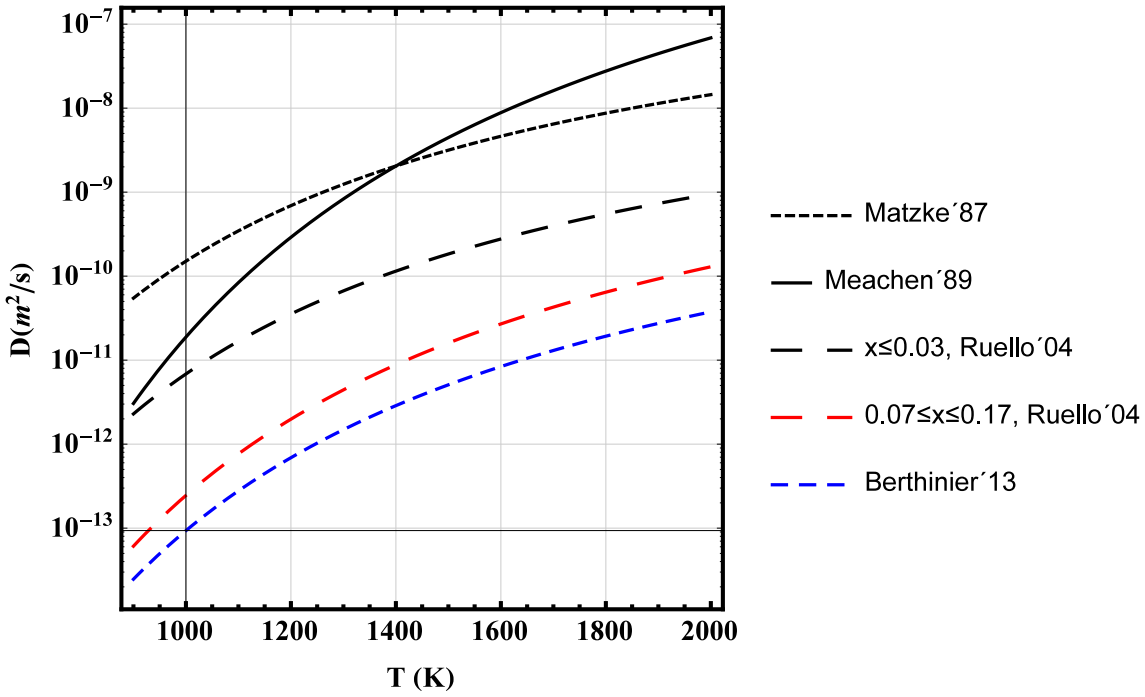

Figure 28: Oxygen diffusion coefficients versus temperature recommended in UO_{2+x} by various authors: Matzke'87 [56] and Meachen'89 [65], Ruello'04 [68], and Berthinier'13 [70].

Recently, Berthinier et al. [70] have made a comprehensive assessment and analysis of experimental data on oxygen diffusion in UO_{2+x} and have proposed the following relation for oxygen diffusion coefficient ($x > 0$):

$$D_x[\frac{\mathrm{m}^2}{\mathrm{s}}] = (1.51 \pm 0.15) \times 10^{-8} \exp\Big(-\frac{99700 \pm 600}{8.3145\,T}\Big). \tag{62}$$

This relation is also plotted in Fig. 28. Certainly, more diffusivity measurements under

[3] In UO_{2+x}, the so-called Willis type cluster has the (2:2:2) configuration and consists of two oxygen interstitial atoms along <110> identified as $0'$, two oxygen interstitial atoms along <111> identified as $0''$, and two vacancies in the oxygen sublattice [1]; for a recent assessment see [69].

strict oxygen potentials are needed to establish the above mentioned results, since many of the underlying measurements were performed under not so well-defined oxygen partial pressures. Our present judgement is to use Meachen's diffusivity, given in Table 4, until the dust settles.

4 Fission gas release from UO_{2+x} fuel

When the fuel cladding ruptures, ingress of steam into the rod oxidizes UO_2 to UO_{2+x}, affecting the chemical potential of oxygen in the fuel thereby fuel behavior [66]. Fission gas (Xe, Kr) diffusivity in hyperstoichiometric fuel is higher than in stoichiometric fuel prior to oxidation [71]. Further oxidation of UO_{2+x} leads to formation of U_4O_9 compound with three types of octahedral phases [1]. Oxidation proceeds by advance of U_4O_9/UO_2 interfaces from the grain boundaries into the UO_2 grains, and U_4O_9 formation causes grain boundary cracking [72]. If more oxygen is added to the fuel the compound U_3O_8 with orthorhombic crystal structure is stabilized [73], which has different physical characteristics compared to UO_2. For example, there is an expansion during the phase transformation that may cause microcracking of fuel, leading to additional release of fluid fission products.
Post-irradiation thermal annealing tests, heated from 800 to 1600 K in about 2 h, made on boiling water reactor (BWR) fuel that was irradiated to 65 MWd/kgU, show that the UO_2 oxidized to U_3O_8 releases up to 70% Xe compared to 10% in normal fuel at 1500 K [11]. Moreover, fission product gas release data from oxidized and normal fuel obtained from post-irradiation annealing experiments clearly indicate that the release of xenon and cesium occurs at much lower temperatures than for unoxidized fuel [74, 75].
Fission gas release (FGR) during post-irradiation thermal annealing depends also on the level of fuel burnup during base irradiation. The data clearly show that with increasing burnup the threshold temperature for release decreases unfavorably during the thermal transient [74]. In fact, the extent of fission gas release depends on relationships between temperature, burnup and fuel microstructure. The periphery of the fuel pellet, which has a higher local burnup and much lower temperature during a base irradiation (for a fuel average burnup of 50 MWd/kgU and higher), acquires a different microstructure. That is, the original grains with a size between 5 and 10 μm restructure to submicrometre sizes (100-300 nm) and the porosity increases significantly. This event is referred to as pellet rim effect or more precisely the high burnup structure (HBS); see *e.g.* [76]. During LOCA type thermal transients, the temperature in the HBS region can rapidly rise beyond 1000 K, leading to an easy and quick gas release. This is due to a very high grain boundary density, a much smaller grain size, and possibly the microcracking of grain boundaries, the latter as a results of swelling or burst of gas bubbles or pores. The data presented in [74] clearly indicate that the onset temperature for gas release during the transient as a function of local burnup is related to different regions of fuel pellet. Hence, fuel oxidation is expected to lower the threshold release temperature markedly. Analysis of the process entails a model for fuel oxidation kinetics and a relation for fission gas diffusivity which is dependent on excess oxygen concentration.
The equations for FGR from UO_{2+x} are basically the same as those of UO_2. The diffusion coefficient for fission product gases (Xe, Kr) is the variable that will be affected by the deviation from stoichiometry. In this section, we first outline a mathematical model for transient FGR (Sec. 4.1) followed by a summary of relations for gas diffusion coefficient in UO_{2+x} (Sec. 4.2). In Sec. 4.3 we show the results of our sample FGR computations. Our treatment here is for the case of a post-irradiation annealing test where there is no gas production during gas migration and release, *i.e.* applicable to LOCA conditions [77].

4.1 Diffusion model for FGR

We outline a computational model for intragranular FGR for the case of postirradiation annealing, during which no gas production (no fission) takes place in the UO_2 fuel, allowing for nonisothermal situations. Our treatment follows that of our earlier report [77], in which a more embracing model was described. We recapitulate the formalism of the equivalent sphere model formulated in [78, 79] using a somewhat different notation. The diffusion equation for gas atoms in an equivalent spherical grain of radius a_0 is

$$\partial_t u(r,t) = D_a(t)\nabla_r^2 u(r,t), \tag{63}$$

subject to the conditions,

$$\partial_r u(r,t)\Big|_{r=0} = 0, \tag{64}$$

$$u(a_0,t) = 0, \tag{65}$$

where $u(r,t)$ is the bulk gas concentration at position r and time t, and $D_a(t)$ is the coefficient of diffusion of gas atoms in the UO_2 grain, dependent on time through temperature T, $\nabla_r^2 = \partial_r^2 + (2/r)\partial_r$, $\partial_r \equiv \partial/\partial r$, etc. We should note that $D_a(t)$ is an effective diffusion coefficient of the gas in the grain, which we assume to have a general form $D_a[T(t)] = k_0(x)k[T(t)]$, where $k_0(x)$ is a prefactor depending on the deviation from stoichiometry x in UO_{2+x}, $k(T(t)) = \exp[-E_a/T(t)]$, E_a is the activation energy for diffusion scaled with the Boltzmann constant k_B (or put $k_B = 1$ with E_a having a dimension of temperature). $D(t) \equiv D_a[T(t)]$ accounts for the presence of intragranular bubbles which trap the gas atoms and the effect of re-solution that prevents the bubbles to act as permanent sinks [80]. Thus at any time, only a fraction of the gas is situated in the intragranular bubbles, while the rest is in solution and able to escape from the grain.
We introduce a new dimensionless time variable τ as

$$\tau(t) = \frac{k_0}{a_0^2}\int_0^t k(s)ds, \tag{66}$$

then express Eq. (63) in the form

$$\partial_\tau u(\rho,\tau) = \nabla_\rho^2 u(\rho,\tau), \tag{67}$$

$$\text{where} \quad \rho = r/a_0. \tag{68}$$

For the case that the initial concentration of gas in the grain is uniform, $u(\rho,0) = u_0$, the solution of Eq. (67) in the form of a series expansion is well-known [81]

$$u(\rho,\tau) = \frac{2u_0}{\rho}\sum_{n=1}^{\infty}\frac{(-1)^{n+1}}{n}\sin(n\pi\rho)e^{-n^2\pi^2\tau}. \tag{69}$$

The average concentration of $u_{\rm av}$ in the sphere at any time is

$$u_{\rm av}(\tau) = \frac{6u_0}{\pi^2}\sum_{n=1}^{\infty}\frac{1}{n^2}e^{-n^2\pi^2\tau}. \tag{70}$$

Thus the fraction of fission gas that escapes the sphere is

$$F(\tau) \;=\; 1 - \frac{6}{\pi^2}\sum_{n=1}^{\infty}\frac{1}{n^2}e^{-n^2\pi^2\tau}. \tag{71}$$

For short times, *i.e.* $\tau \leq 1/\pi^2$, we have [82]

$$F(\tau) \;=\; 6\Big(\frac{\tau}{\pi}\Big)^{1/2} - 3\tau, \quad \text{for } \tau \leq 1/\pi^2, \tag{72}$$

which is valid for $F < 0.9$. For late times the $n = 1$ is the dominant term and the release fraction may be approximated by

$$F(\tau) \;=\; 1 - \frac{6}{\pi^2}e^{-\pi^2\tau}, \quad \text{for } \tau > 1/\pi^2. \tag{73}$$

Carslaw and Jaeger [81] provide also solutions for $u(r,0) = f(r)$ and the case where $f(r) = b_0 + br + cr^2 + dr^3 + \ldots$ among others. The details of the numerical implementation of the model are given in [77].

4.2 Fission gas diffusion coefficient in UO_{2+x}

Experimental The effect of the O/U ratio in uranium oxide fuel on the diffusion coefficient for fission product gases (Kr, Xe) and its impact on fission gas release has been known since the early works of Lindner and Matzke [83] (Chalmers tekniska högskola, Göteborg) and Miekeley and Felix [71] (Hahn-Meitner Institute, Berlin). Solid state chemistry of diffusion processes in nuclear fuels in general and in UO_{2+x} in particular have been discussed by Matzke in a number of review articles in the past [84, 85, 86]. A nice literature review and assessment of the subject (up to year 2000) has been made by Y.S. Kim [87], information from which, we have utilized here.

Lindner and Matzke measured the diffusion coefficient of ^{133}Xe in UO_{2+x} for $x = \mathrm{O/U} - 2.00$ values in the range 0 to 0.67 and temperatures covering 773 to 1773 K. They found a steady increase of Xe diffusivity with x. For example, at 1673 K the gas diffusivity at $x = 0.12$ was about 40 times higher than diffusivity at $x = 0$. They observed that the activation energy of diffusivity is roughly constant over the stoichiometry range of $\mathrm{O/U} = 2.0 - 2.12$, despite the fact that the gas diffusion coefficient increases linearly with the oxygen content. Miekeley and Felix's later experimental study [71], however, led them to conclude that the diffusion coefficients are independent of composition for the ratios $2.02 \leq \mathrm{O/U} \leq 2.24$, in conflict with Lindner-Matzke's results. In particular, Miekeley and Felix measurements led to the following activation energies for the diffusion of xenon: 6.0 ± 0.1 eV in UO_{2-x}, 3.9 ± 0.4 eV in UO_2, and 1.7 ± 0.4 eV in UO_{2+x}. Within each x-region, the activation energy was insensitive to changes in x, *i.e.* the O/U ratio.

The manifest discrepancy between the Lindner-Matzke and Miekeley-Felix results may be explained by considering the measurements of Shiba [88]. Shiba (JAERI, Japan) measured ^{133}Xe (and ^{131}I) release from preirradiated specimens by annealing in an inert atmosphere. He observed that gas release increases with the oxygen-to-uranium ratio from O/U=2.00 to 2.20 then it sharply decreases from O/U=2.20 to 2.25 exhibiting minima at O/U=2.00 and 2.25, which correspond to UO_2 and U_4O_9, respectively. He asserted that stoichiometric oxides (*i.e.*, UO_2 and U_4O_9) release less fission gas during annealing since those compounds

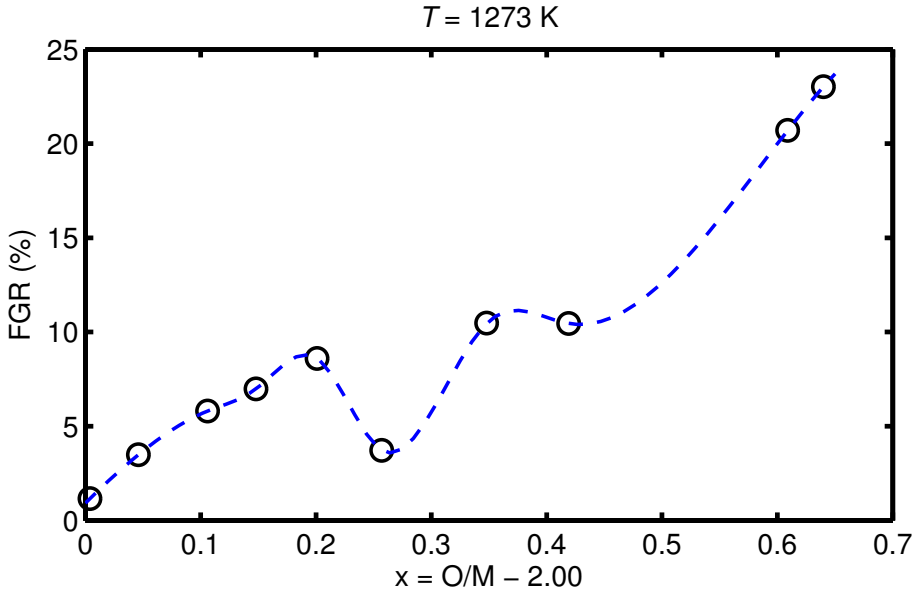

Figure 29: Measured fission gas (^{133}Xe) released at 1273 K versus stoichiometry excess (◯) upon post-irradiation annealing; from figure 11 in [88]. The broken line is a spline interpolation through the data points.

hold less gas. This effect, he argued, is the result of fewer defects in stoichiometric oxides, which are less susceptible to fission fragment damage compared to hyperstoichiometric fuel. He indicated that since defects in the diffusing medium trap fission gases, more defects in the fuel correspond to more gas retention. Therefore, during annealing, fission gas escapes more readily from stoichiometric oxide than hyperstoichiometric. Part of these differences, however, could be due to the changes in the involved energies of fission gases and crystal defects in urania. For example, Ball and Grimes's atomistic computations (Mott-Littleton approximation) show the way the solution energies and migration mechanisms change as a function of the oxygen content of the fuel [89]. Their computations show that the solution energies decrease from UO_{2-x} to UO_{2+x} but increase again on further oxidation to U_4O_9.[4]

Shiba presented data on xenon and iodine release fractions from preirradiated UO_{2+x} samples upon annealing (figure 11 in [88]). The annealing method utilized was a slow heatup of the sample, at a rate 5°C/min, from 50°C for ^{133}Xe (200°C for ^{131}I) in an inert gas environment until the temperature reached 1000°C and held for about 20 min at this temperature. Figure 29 shows the outcome of these experiments for the ^{133}Xe release.

A series of experiments in which release of ^{85}Kr from hyperstoichiometric uranium dioxide was measured during annealing in CO/CO_2 atmospheres have been reported by Killeen and Turnbull [90] (Berkeley Nuclear Laboratories, Gloucestershire, UK). The CO/CO_2 atmosphere oxidizes the UO_2 fuel during annealing as we recall from the Carter-Lay experiment discussed in section 2.1. The fuel samples tested by Killeen and Turnbull were preirradiated to 18 MWd/kgU. They interpreted their data in terms of gas release by atomic diffusion, where a model was proposed relating the diffusion coefficient to the degree of

[4]Ball and Grimes define the solution energy for a gas atom associated with a trap site in the lattice as the sum of the energy required for bringing a gas atom from infinity and putting it at a preexisting trap site plus the energy required to form a trap site [89].

nonstoichiometry.

Modeling In order to analyze their measurements, Killeen and Turnbull developed a composite expression for the diffusion coefficient that consisted of four terms: the intrinsic diffusion coefficient for a high temperature domain by Davies and Long [91], an irradiation-induced athermal diffusion coefficient for a low temperature domain by Matzke [92], a fission-induced vacancy diffusion coefficient for an intermediate temperature domain attributed to J. V. Sharp 1969 (unpublished), and an oxidation effect term due to Lidiard [63]. Hence, the diffusion coefficient (m^2/s) is written as the sum of these four terms:

$$D = D_{\rm DL} + D_{\rm M} + D_{\rm S} + D_{\rm L}. \tag{74}$$

Here, $D_{\rm DL} = 7.6 \times 10^{-10} \exp(-35000/T)$, T (K), $D_{\rm M} = 2 \times 10^{-40}\phi$, ϕ is the fission rate (fission/m^3·s), $D_{\rm S} = s^2 j_v V_i$ and $D_{\rm L} = s^2 j_v V_u$ with s being the atomic jump distance, j_v the vacancy jump rate, V_i the irradiation-induced vacancy concentration and V_u the oxidation-induced uranium vacancy concentration. The expressions for the latter two quantities are listed in Box 4.1.

The combined expression for the diffusion coefficient proposed by Killeen and Turnbull (Box 4.1) although is mechanism-based and fits their experimental data quite well, it is somewhat inconvenient for a fuel rod modeling program due to the complexity of the expressions for V_i and V_u and the presence of many empirical constants and parameters, which may vary from one situation to another. For this reason Kim [87] provided a simplified practical expression for the effective diffusion coefficient of fission gas in oxidized fuel, *i.e.* UO_{2+x} for computer modeling application. It is expressed as

$$\begin{aligned} D_{\rm eff} &= 7.6 \times 10^{-10} e^{-35000/T} f(x) + 2 \times 10^{-40}\phi, \\ f(x) &= 1 + 493x + 32182x^2. \end{aligned} \tag{75}$$

Note that in case of unoxidized UO_2 ($x = 0$) this expression is a combination of the thermal Davies-Long and the athermal Matzke diffusivities. Kim [87] has compared the expression (75) in the hyperstoichiometry range $0.005 \le x \le 0.12$ and temperature range $1000 \le T \le 1600$ K against some measured data [71, 83] for Xe diffusion in UO_{2+x}.

In Fig. 30(a), we have plotted $D_{\rm eff}$ as a function of temperature for several values of x and the fission density $\phi = 10^{19}$ fission/m^3·s. A substantial increase in the diffusion coefficient can be seen for $x \ge 0.01$ at temperatures $T \ge 1400$ K. For example, at 1600 K, the ratio $D_{\rm eff}(x = 0.1)/D_{\rm eff}(x = 0.001) \approx 240$. Also, for $T \ge 1400$ K the contribution of the athermal term ($2 \times 10^{-40}\phi$) is negligible. In Fig. 30(b), we compare the diffusion coefficient of xenon with that of oxygen as a function of temperature in UO_{2+x}.

Finally, we should mention that xenon transport in UO_{2+x} has been evaluated by Andersson and coworkers using a density functional theory computational method [93]. Andersson *et al.*'s work reveals the complexity of the multi-body effects at the microscopic level. The researchers attempt various approaches (assumptions) for the computation of the activation energies of Xe diffusion and compare their results with the scanty experimental data available. For example, their approach A results, which are closest to measurements, manifest activation energies: 7.12 eV in UO_{2-x}, 3.80 eV in UO_2 and 2.97 eV in UO_{2+x}. The corresponding measurements by Miekeley and Felix [71] gave 6.0 ± 0.1 eV, 3.9 ± 0.4 eV and 1.7 ± 0.4 eV, respectively.

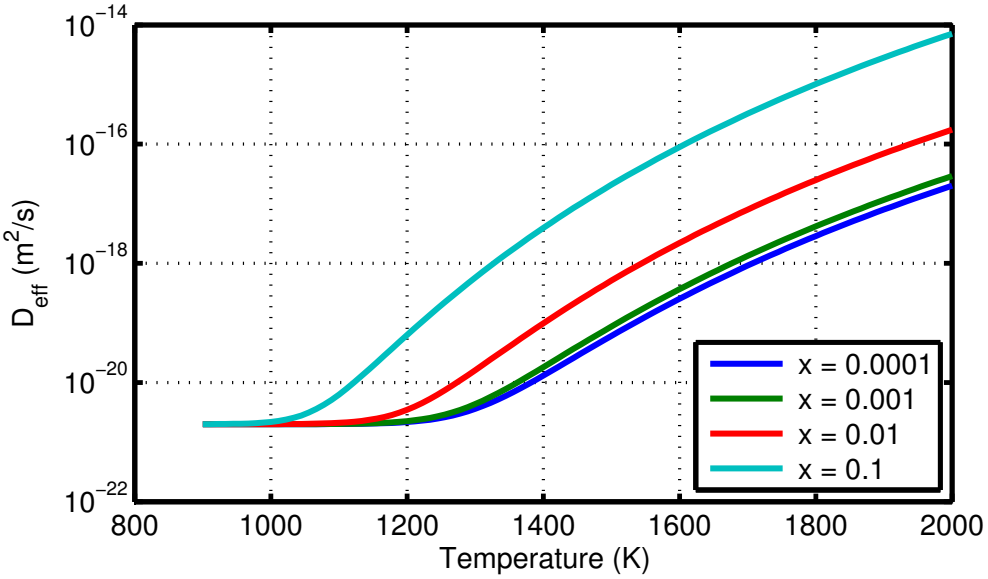

(a)

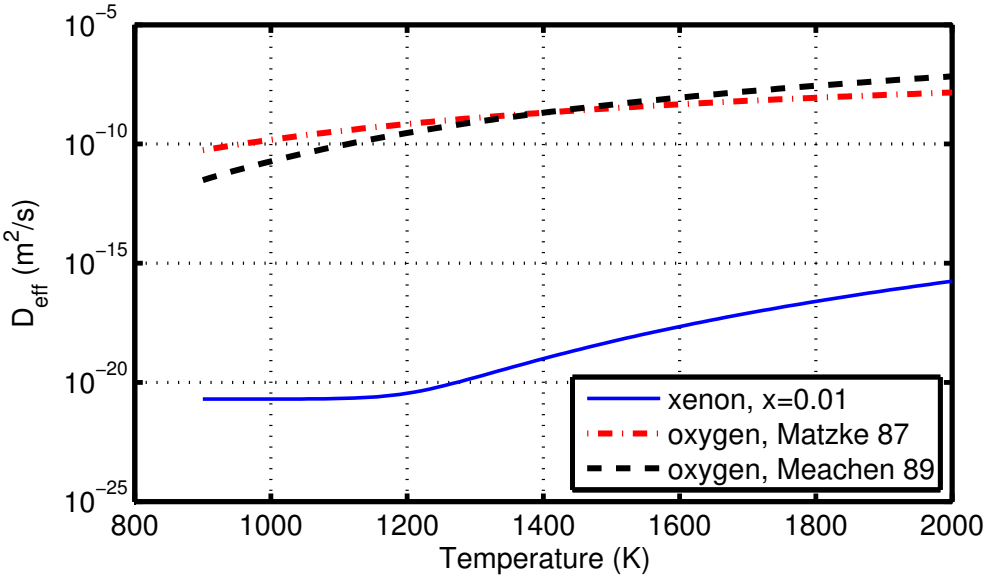

(b)

Figure 30: (a) Effective diffusion coefficient of fission gas (Xe) in UO_{2+x} according to formula (75) for the fission density of $\phi = 10^{19}$ fission/m^3·s. (b) Comparison between the diffusion coefficients of oxygen and Xe with $x = 0.01$, where Matzke 87 [56] and Meachen 89 [65].

KILLEEN-TURNBULL DIFFUSION COEFFICIENT FOR KR IN UO_{2+x}

$$D = D_0 e^{-35000/T} + s^2 j_v (V_i + V_u) + A\phi.$$

Irradiation-induced vacancy concentration:

$$V_i = \frac{(\alpha_s s^2 + Z V_u)}{2Z} \left[\left(1 + \frac{4KZ}{j_v \left(\alpha_s s^2 + Z V_u\right)^2} \right)^{1/2} - 1 \right]$$

Oxidation-induced vacancy concentration:

$$V_u = \frac{S x^2}{G^2} \left[\frac{1}{2} + \frac{G}{x^2} + \frac{1}{2} \left(1 + \frac{4G}{x^2} \right)^{1/2} \right]$$

Here S and G are the Schottky and Frenkel energy barriers:

$$S = \exp(-Q_s/T); \qquad G = \exp(-Q_g/T)$$

- $D_0 = 7.6 \times 10^{-10}$ m^2/s, $A = 2 \times 10^{-40}$ m
- $\alpha_s = 10^{15}$ m^{-2}, fixed sink strength
- $s = 3 \times 10^{-10}$ m, atomic jump distance
- $Z \approx 100$, no. of sites around a point defect for recombination
- $j_v = 10^{13} \exp(-27800/T)$ s^{-1}, vacancy jump rate
- $K = 2 \times 10^{-4}$ defect/atom·s, damage rate
- $Q_s = 74100$ K, $Q_g = 35800$ K

Box 4.1: Killeen-Turnbull diffusion coefficient of fission gas in UO_{2+x}.

4.3 An illustrative example

In this subsection, we use the diffusion-based approach described in section 4.1 to compute fission gas release from UO_{2+x} fuel in an annealing experiment on UO_2 [94]. The considered experiment by Kashibe and Une [94] is fairly well characterized and simple enough to offer an analytical comparison with the considered model.

The experimental procedure was as follows. The UO_2 fuel samples, weighing 10 mg each, with a mean grain size of 15 μm, density 10.71 g/cm^3, the O/U ratio 2.004, were irradiated in evacuated quartz capsules for 6 h at a thermal neutron flux of 5×10^{17} neutrons/(m^{2}s) in the JRR-4 reactor of the Japan Atomic Energy Research Institute (JAERI), resulting in a total irradiation dose of 1.08×10^{23} fissions/m^3 corresponding to a fuel burnup of 4 MWd/tU. After irradiation, the samples were cooled for a duration between 8 and 13 days to allow for decay of the short-lived nuclides [94].

The capsule containing the irradiated fuel sample was then heated first rapidly from room temperature to 1373 K (heating rate 1.7 K/s), then heated step-wise with a temperature step of 100 K and hold time of 1 h to 1873 K. The β-activity of released ^{137}Xe during heating was measured continuously. Afterward, the remaining ^{137}Xe in the sample was determined

by dissolving the fuel in nitric acid [94].
In our computation, we have simplified the annealing temperature history (its step-wise part) as depicted in Fig. 31, which corresponds to that shown in figure 5 in [94], without loss of much accuracy. Using this temperature history, we compute first the parameter τ given by Eq. (66) as shown in Fig. 32(a). To this end, we have used the effective diffusion coefficient according to Eq. (75) for Xe in UO_{2+x} and the equivalent sphere radius $a_0 = 5.0$ μm.[5] We compute τ according to the method described in appendix A of [77] and use the closed form expression Eq. (72) to calculate the release fraction during the annealing test, Fig. 32(b). The end-of-test (400 minutes) gas release fraction measured was 12%; cf. figure 5 in [94]. Our end-of-test computations for FGR give: 11.5% for $x = 0.0005$ and 19% for $x = 0.004$. The reason for computing higher FGRs than the measurements despite employing a larger equivalent sphere radius (than estimated by Kashibe and Une) stems from the difference between Kim's effective diffusivity (which is the Davies-Long for UO_2) and that recommended by Kashibe-Une, which is $D = 1.7 \times 10^{-12} e^{-28264/T}$ $m^2 s^{-1}$. The Davies-Long diffusion coefficient predicts higher diffusivities at temperatures $T > 1200K$ than Kashibe-Une's; see Fig. 33.

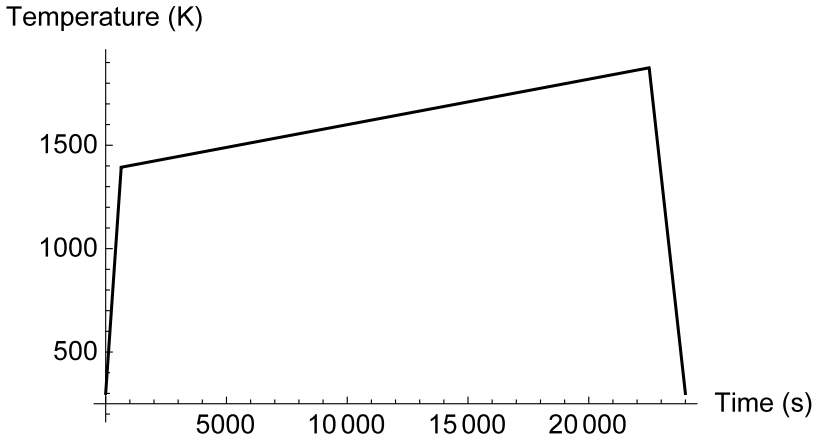

Figure 31: Simplified temperature history in Series I annealing tests in [94].

[5] Actually, a_0 was estimated to be 1.88 μm for the tested $UO_{2.004}$ sample [94].

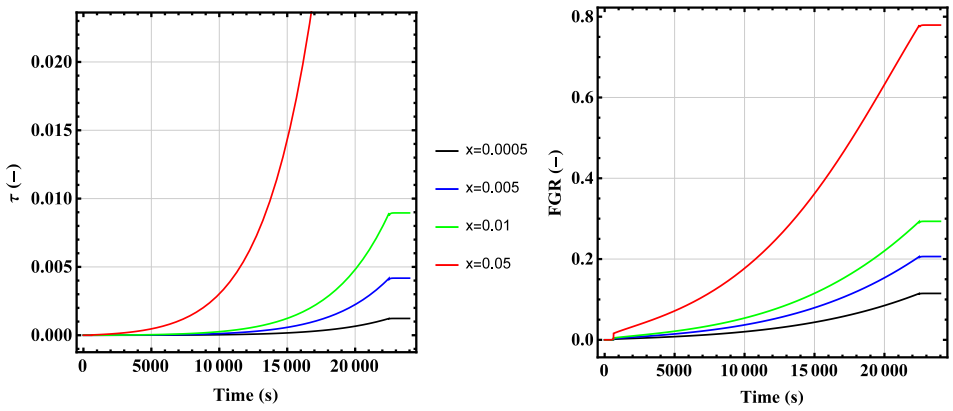

(a) (b)

Figure 32: (a) Computation of the parameter τ, Eq. (66), using the temperature history in figure 31. (b) Computation of the cumulative fractional release of ^{137}Xe gas using the temperature history shown in figure 31 and Eq. (72).

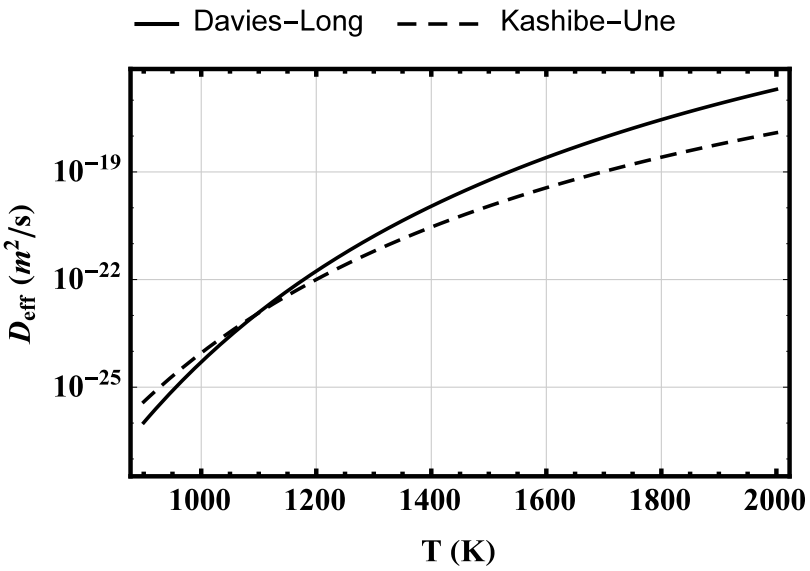

Figure 33: The diffusion coefficient for Xe in UO_2: Davies-Long [91] vs. Kashibe-Une [94].

5 Summary and conclusions

In this report, we have reviewed the investigations that have been carried out regarding the oxidation of UO_2 fuel and its consequence to fuel behavior especially fission product gas migration and release in and from the fuel. We have assessed the existing experimental data and models in this area. Moreover, we have discussed their (data and models) applicability to light water reactors under both reactor faults and during normal operations.

Oxidation of UO_2 fuel under reactor faults occurs when fuel cladding fails, thereby letting steam/water to enter the fuel rod. The steam/water will react with the fuel to produce UO_{2+x} releasing hydrogen. In addition, the fission of uranium nuclei in UO_2 may be viewed as an oxidative process. This is because the generated fission products cannot bind completely the oxygen atoms that are liberated during fission. That is to say, not all the fission products are capable of binding oxygen, *e.g.* Kr and Xe. Notwithstanding, the main elements forming oxides, such as Zr, Y, the rare earths, etc., posses an average valence that is lower than that of the actinides in the fuel, and thereby bind relatively less oxygen. Other fission products that have the potential to oxidize remain virtually as pure metal or as precipitate alloy. This is because the free energy of formation of their oxides is much higher than the oxygen potential in UO_2. As a consequence, there will be a positive shift in the UO_2 stoichiometry with fuel burnup during normal irradiation.

In Sec. 2, fuel oxidation due to fluids reaction with UO_2 was discussed in detail. Experimental investigations carried out in various laboratories on both unirradiated and irradiated UO_2 under diverse conditions were deliberated. The experiments indicate that the evolution of stoichiometry is surface-reaction driven. The rate of the oxidation is proportional to the surface exchange coefficient α, which is highly temperature dependent, and also related to the fuel geometry, namely the surface-to-volume ratio S/V. Hence fuel fragments with high S/V, *e.g.* very small diameter, very porous, or otherwise not compact, oxidize at much higher rates than monolithic fuel, since more surface is available to react. The considered experiments have determined α, which has an Arrhenius temperature dependence and also depends on the oxidizing environment, *e.g.* whether the fuel is oxidized in pure steam or in steam/Ar/H_2 mixture.

Models describing the UO_2 oxidation have also been assessed or discussed by comparing their outcome with experimental data. An important conclusion from our computations is illustrated in Fig. 24, which shows the dependence of the oxidation characteristic time τ_c as a function of temperature for several values of the S/V ratio. It shows that, *e.g.* at a fuel temperature of ≈ 1500 K, τ_c may vary between 100 to 10^4 s depending on the considered S/V values. And this quantity rapidly decreases by increasing the temperature.

Based on our evaluation, a suitable model for UO_2 oxidation kinetics, applicable to steady-states and transients, is suggested. It has been noted that modeling fuel pellet oxidation involves production of oxygen and thermal diffusion of oxygen atoms under concentration and temperature gradients in the fuel. Therefore, an appropriate partial differential equation followed by suitable boundary conditions need to be solved; see Sec. 2.4.

The topic of oxygen redistribution in fuel pellet is detailed in Sec. 3 under both steady states and transient conditions. Both the phenomenology and empirical data are discussed. A mathematical model for computation of the stoichiometry deviation across fuel pellet is presented and then used to compute the evolution of $x = \mathrm{O/U} - 2.00$ at two fuel burnups for a given power history. For transient conditions, *i.e.* the case where the full time-dependent thermodiffusion equation needs to be considered, we only evaluate the relaxation time or time to equilibration. The outcome of the computations depends very much on the oxy-

gen diffusion coefficient utilized, which is an empirical-based quantity with an Arrhenius temperature dependence. The data reported for this quantity vary vastly in the literature, Fig. 28, thereby bringing in a large uncertainty in the computations. The source of this uncertainty stems from the not so precise or well-defined oxygen partial pressures in the experiments. Despite this, a diffusivity coefficient based on the assessment of Meachen [65] is recommended for computations tentatively.

Another source of uncertainty in the evaluation of oxygen redistribution in the pellet is the role of Zircaloy cladding as an oxygen getter. The scarcity of data on this effect hampers us to make a definite conclusion on this issue.

The impact of fuel oxidation on fission product gas release is discussed in Sec. 4, where we have reviewed briefly the literature on the subject. A noted experiment in this connection is an early post-irradiation annealing experiment conducted by Shiba [88], who monitored ^{133}Xe release as a function of $x = \mathrm{O/U} - 2.00$ from UO_{2+x} at 1000°C. He observed that gas release increases from $x \approx 0$ to $x \approx 0.2$, then a dip occurs at $x \approx 0.25$ (corresponding to the formation of $\mathrm{U_4O_9}$) followed by a dramatic increase at $x \approx 0.66$ corresponding to the formation of $\mathrm{U_3O_8}$, see Fig. 29. In this connection, the main quantity affected by fuel oxidation is the effective diffusion coefficient or diffusivity of fission product gases. Fuel oxidation enhances this diffusivity as a function of x in a parabolic fashion for $0.005 \leq x \leq 0.12$ in the temperature range of $1000 \leq T \leq 1600$ K.

In Sec. 4, we have also presented a method for computing transient fission gas release during post-irradiation annealing conditions. We have used the method to evaluate an annealing test and have studied the effect of varying the stoichiometry variable $x \geq 0$ on release fraction. Our end-of-test computation of release fraction yields 11.5% at $x \approx 0$, $\approx 19\%$ at $x \approx 0.004$ and $\approx 30\%$ at $x \approx 0.01$. Thereby demonstrating the large impact of fuel oxidation on fission gas release, see Fig. 32.

There are also three appendices: In Appendix A, the constitutive relations for calculation of oxygen partial pressure and oxygen potential of the fuel are delineated, through which the equilibrium stoichiometry deviation x_{eq} as a function of temperature and the hydrogen-to-steam ratio $P_{\mathrm{H_2}}/P_{\mathrm{H_2O}}$ are evaluated. This appendix also includes a section that describes how to compute the oxygen potential in the fuel-cladding gap. Appendix B provides a mathematical method to treat oxygen thermal diffusion in the fuel pellet under transient conditions. More specifically, it shows how to transform the putative partial differential equation to a Sturm-Liouville eigenvalue problem. The smallest eigenvalue gives the the time constant of the problem. The relations for the UO_{2+x} thermal conductivity are summarized in Appendix C. This quantity appears in the heat equation for fuel pellet which affects fuel temperature. We show how the thermal conductivity is reduced as a function of the stoichiometry deviation.

Acknowledgments It is a pleasure to thank Lars Olof Jernkvist for helpful discussions and comments, and Anna Alvestav for feedback. The work was supported by the Swedish Radiation Safety Authority (SSM) under the contract number SSM2016-3944.

A Oxygen partial pressure in the fuel and gap

A.1 Oxygen partial pressure in the fuel

The oxygen partial pressure in UO_{2+x} fuel as a function of x, i.e., $P_{O_2}(x)$ (in atm) can be calculated either from Blackburn's relation [95]

$$\ln P_{O_2}(x) = 2\ln\frac{x(2+x)}{1-x} + 108x^2 - \frac{32700}{T} + 9.92, \tag{A.1}$$

or from the solid solution correlation of Lindemer and Besmann [96]:

$$P_{O_2} = \min(P_1, P_2) \tag{A.2}$$

where

$$\ln P_1 = 2\ln\frac{x(1-2x)^2}{(1-3x)^3} - \frac{37621}{T} + 15.15 \tag{A.3}$$

$$\ln P_2 = 4\ln\frac{2x(1-2x)}{(1-4x)^2} - \frac{43298}{T} + 25.74. \tag{A.4}$$

These relations are plotted as a function of x and temperature in figure A.1 for the sake of comparison. It is seen that the trend of the deviation between the two relations depends on the oxygen concentration x and temperature.

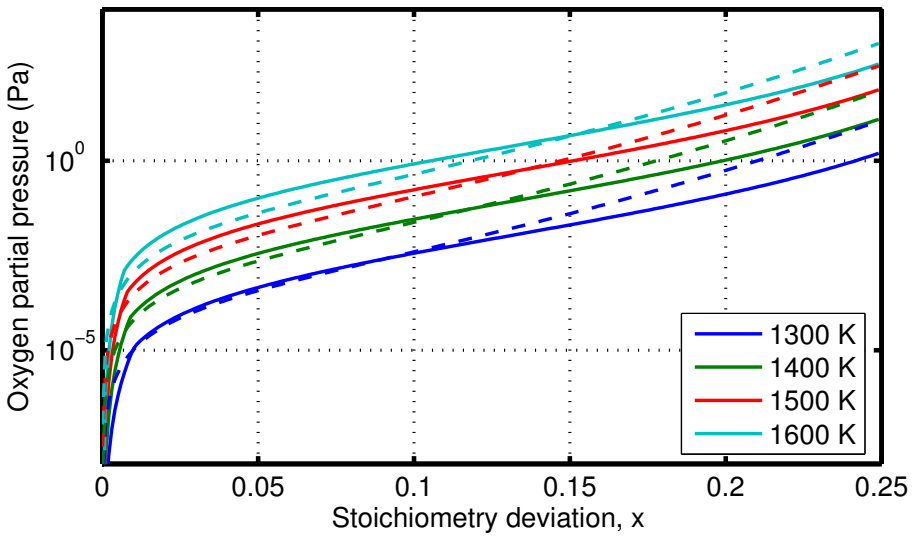

Figure A.1: Oxygen partial pressure in the fuel calculated by the Blackburn (dashed lines) and the Lindemer-Besmann correlations.

Using the aforementioned formulas for the oxygen partial pressure and Eqs. (14)-(15) of the main text, the equilibrium stoichiometry concentration x_{eq} as a function of temperature for given values of the hydrogen-to-steam ratio ($q = P_{H_2}/P_{H_2O}$) can be calculated. Figure A.2 displays the results of such computations.

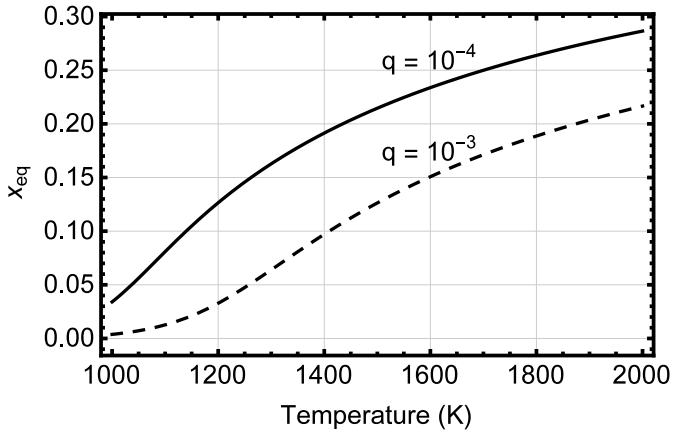

(a)

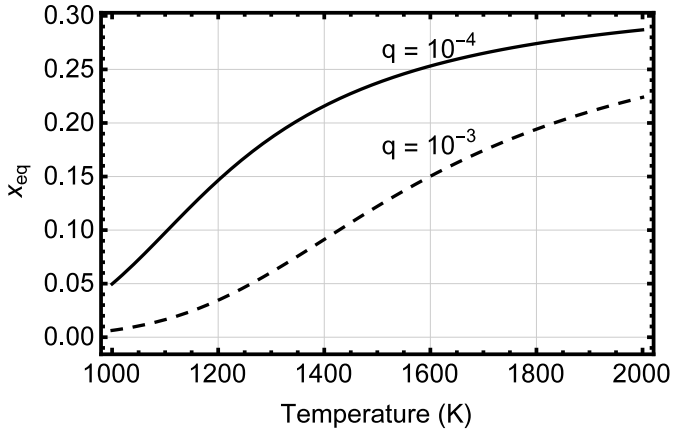

(b)

Figure A.2: The equilibrium stoichiometry deviation x_{eq} vs. temperature for two values of the hydrogen-to-steam ratio $q = P_{\mathrm{H_2}}/P_{\mathrm{H_2O}}$ using the partial oxygen pressure relations according to (a) Blackburn, (b) Lindemer-Besmann.

A.2 Oxygen partial pressure in the fuel-cladding gap

The oxygen potential for an ideal gas mixture in the fuel-pellet gap consisting of Xe, H_2O, H_2 etc. can be evaluated by the method given in [27]. The total pressure is obtained from the partial pressures P_j of each component j: $P_{tot} = \sum_{j=1}^{n} P_j$. For the decomposition of water according to reaction (12), to maintain equilibrium, the partial pressures after decomposition are

$$P_{\mathrm{H_2O}} = P^0_{\mathrm{H_2O}} - \mathfrak{p}, \quad P_{\mathrm{H_2}} = P^0_{\mathrm{H_2}} + \mathfrak{p}, \quad P_{\mathrm{O_2}} = \frac{\mathfrak{p}}{2}, \tag{A.5}$$

where the superscript 0 refers to the initial partial pressure quantities in the gap and $\mathfrak{p}$ is the as-yet unknown partial pressure to maintain equilibrium. The condition for equilibrium is found by combining relations (A.5) and (13)-(14), which yields

$$K_{\mathrm{H_2O}} = \frac{P^0_{\mathrm{H_2}} + \mathfrak{p}}{P^0_{\mathrm{H_2O}} - \mathfrak{p}} \sqrt{\frac{\mathfrak{p}}{2}}. \tag{A.6}$$

Equation (A.6) is solved for $\mathfrak{p}$ by evaluating the equilibrium constant in equation (14) at

a given temperature T and initial partial pressures. For example, in case of pure steam, equation (A.6) reduces to

$$\mathfrak{p}^3 - 2K_{\mathrm{H_2O}}^2(P_{\mathrm{H_2O}}^0 - \mathfrak{p})^2 = 0. \tag{A.7}$$

Solving for $\mathfrak{p} \equiv 2P_{\mathrm{O_2}}$ with $P_{\mathrm{H_2O}}^0 = 1$ atm, the temperature dependence of $P_{\mathrm{O_2}}$ is calculated (figure A.3). For more details see [27].

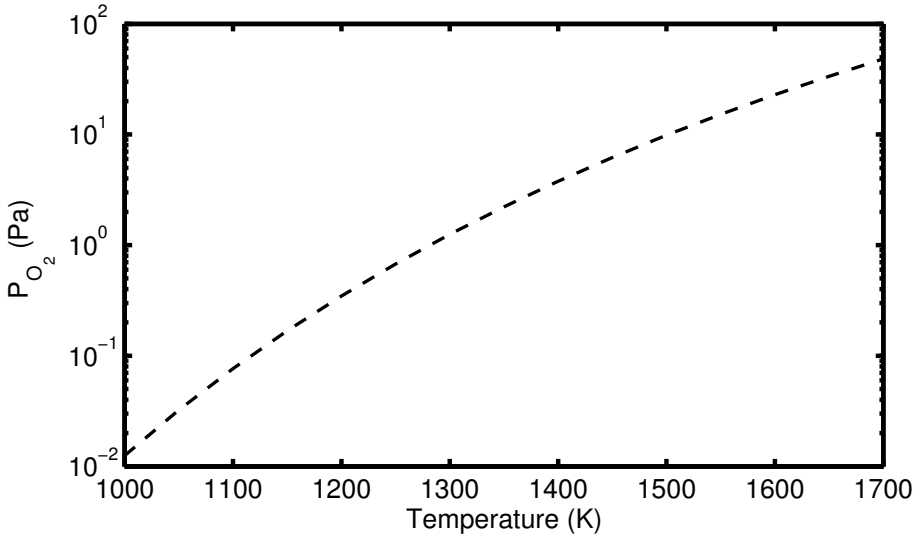

Figure A.3: Calculated oxygen partial pressure in the gap at $P_{\mathrm{H_2O}}^0 = 1$ atm.

A.3 Oxygen potential of UO_{2+x} in various atmospheres

The oxygen potential of the urania fuel determines its oxidation state and thereby many of its chemico-physical properties. The condition or criterion for chemical equilibrium between the gaseous oxygen and the solid oxide is the equality of their chemical potentials [48], namely

$$\frac{1}{2}\mu_{\mathrm{O_2(g)}} = \mu_{\mathrm{O(g)}}, \tag{A.8}$$

$$\mu_{\mathrm{O(g)}} = \mu_{\mathrm{O(ss)}}, \tag{A.9}$$

where μ stands for chemical potential and indices (g) and (ss), distinguish the gaseous state and solid solution respectively. The chemical potential of $\mathrm{O_2(g)}$ is given by [48]

$$\mu_{\mathrm{O_2(g)}} = +G_{\mathrm{O_2}}^0 + RT\ln p_{\mathrm{O_2}}, \tag{A.10}$$

where $G_{\mathrm{O_2}}^0$ is the Gibbs freee energy of pure oxygen gas at temperature T at the standard-state pressure, which is taken to be 1 atm, and $p_{\mathrm{O_2}}$ is the oxygen partial pressure. Combining Eqs. (A.8) and (A.10) gives

$$\Delta\overline{G}_{\mathrm{O_2}} \equiv RT\ln p_{\mathrm{O_2}} = 2\mu_{\mathrm{O(ss)}} - G_{\mathrm{O_2}}^0. \tag{A.11}$$

Here, the quantity $\Delta\overline{G}_{O_2} \equiv RT \ln p_{O_2}$ is the molal Gibbs free energy of oxygen in solid per mole of O_2 or the *oxygen potential* of the solid. It is the difference between the chemical potential of oxygen in the solid and that of pure gaseous oxygen at the same temperature and at 1 atm pressure [48].
Figure A.4 shows calculated oxygen potential of UO_{2+x} as a function of temperature for several values of $x = O/U - 2.00$ (solid lines) using Eqs. (A.2) and (A.11). Furthermore, Une and coworkers [16] have developed a correlation for $\Delta\overline{G}_{O_2}$ as a function of the hydrogen-to-steam ratio $q = P_{H_2}/P_{H_2O}$ and temperature (T), which we have used to plot the dashed lines in this figure. That correlation (J/mol) reads

$$\Delta\overline{G}_{O_2}(g) = -501200 + 111.4T - 2RT \ln\left(\frac{P_{H_2}}{P_{H_2O}}\right) \tag{A.12}$$

with $R = 8.31433$ J/mol·K and T is the temperature in kelvin.

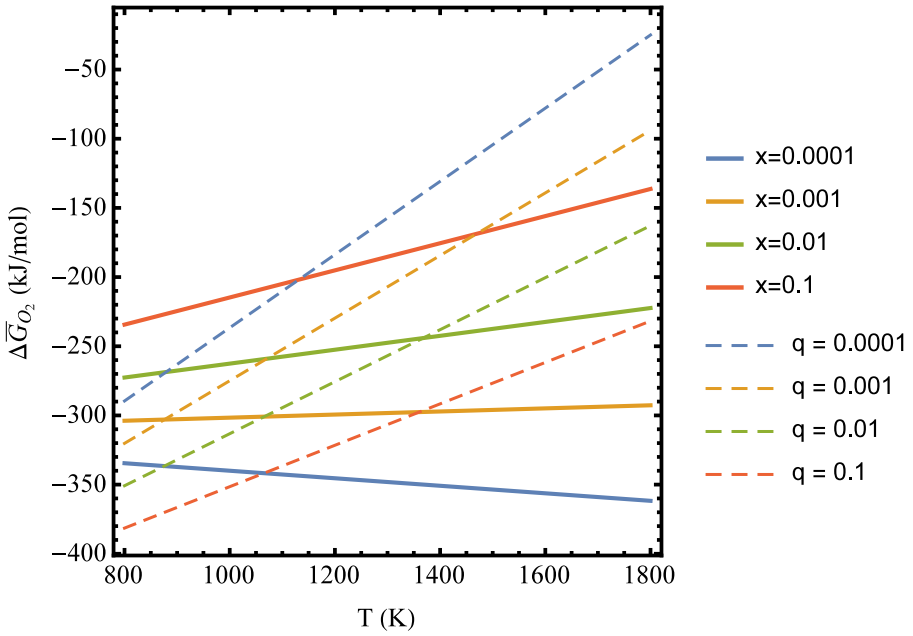

Figure A.4: Oxygen potential of UO_{2+x} as a function of temperature for several values of x and that of H_2/H_2O mixtures with $q = P_{H_2}/P_{H_2O}$ (dashed).

B Oxygen redistribution: Transient solution

In this section, we present the method of the solution of transient thermal diffusion equation as described in [57], i.e. Eq. (48). The solution to this equation is expressed by a perturbative infinite series

$$\chi = \tilde{\chi}_0 + \sum_{i=1}^{\infty} \varepsilon^i \chi_i, \tag{B.1}$$

where ε^i is a perturbation parameter assumed to be small ($\varepsilon^i < 1$). Furthermore, in a quasi-static condition, $\tilde{\chi}_0$ is assumed to be weakly time dependent.
Substituting Eq. (B.1) into Eq. (48) and considering the first term

$$\frac{\partial \tilde{\chi}_0}{\partial t} = -\frac{\partial \chi_1}{\partial t} + \frac{1}{r}\frac{\partial}{\partial r}\Big[rD_x\Big(\frac{\partial}{\partial r} - \tilde{g}\Big)\chi_1\Big], \tag{B.2}$$

$$\text{with} \qquad \tilde{g} = \big[Q(\tilde{\chi}_0) + \tilde{\chi}_0 Q'(\tilde{\chi}_0)\big]\frac{\partial \beta}{\partial r}. \tag{B.3}$$

Here, the approximation $Q(\chi) \approx Q(\tilde{\chi}_0) + \varepsilon\chi_1 Q'$ with $Q' \equiv \partial Q/\partial\chi_1$ was used.
Next, an orthogonal basis expansion ansatz on χ_1 is made

$$\chi_1(r,t) = \sum_{k=0}^{\infty} \alpha_k(t)\tilde{e}_k(r,t), \tag{B.4}$$

where $\tilde{e}_k$ are the orthogonal basis functions and the coefficients α_k obey

$$\frac{\partial \alpha_k(t)}{\partial t} = -\tilde{\lambda}_k \alpha_k(t) - \psi_k(t). \tag{B.5}$$

Substituting Eqs. (B.4) and (B.5) in Eq. (B.2)

$$\frac{\partial \tilde{\chi}_0}{\partial t} - \sum_{k=0}^{\infty} \psi_k \tilde{e}_k = \sum_{k=0}^{\infty} \alpha_k \left\{ \tilde{\lambda}_k \tilde{e}_k + \frac{1}{r}\frac{\partial}{\partial r}\Big[rD_x\Big(\frac{\partial}{\partial r} - \tilde{g}\Big)\tilde{e}_k\Big] \right\}, \tag{B.6}$$

where we tacitly assumed that $\partial\tilde{e}_k/\partial t \approx 0$. If now one equates the left-hand side of Eq. (B.6) to zero and the right-hand side termwise to zero, we obtain

$$\tilde{\lambda}_k r e^{-\mathscr{G}}\tilde{e}_k = -\frac{\partial}{\partial r}\Big(D_x r e^{-\mathscr{G}}\frac{\partial \tilde{e}_k}{\partial r}\Big) + e^{-\mathscr{G}}\tilde{e}_k\frac{\partial (D_x r\tilde{g})}{\partial r}, \tag{B.7}$$

where $d\mathscr{G}/dr = \tilde{g}$. Equation (B.7) can be reduced into an eigenvalue equation, i.e. with eigenvalues $\tilde{\lambda}_k$ and eigenfunctions $\tilde{f}_k \equiv e^{-\mathscr{G}}\tilde{e}_k(r)$, in the form

$$\hat{\mathscr{L}}\tilde{f}_k + \frac{\tilde{\lambda}_k}{D_x} r\tilde{f}_k = 0, \tag{B.8}$$

$$\hat{\mathscr{L}} = r\frac{d^2}{dr^2} + (1 + r\tilde{g})\frac{d}{dr}. \tag{B.9}$$

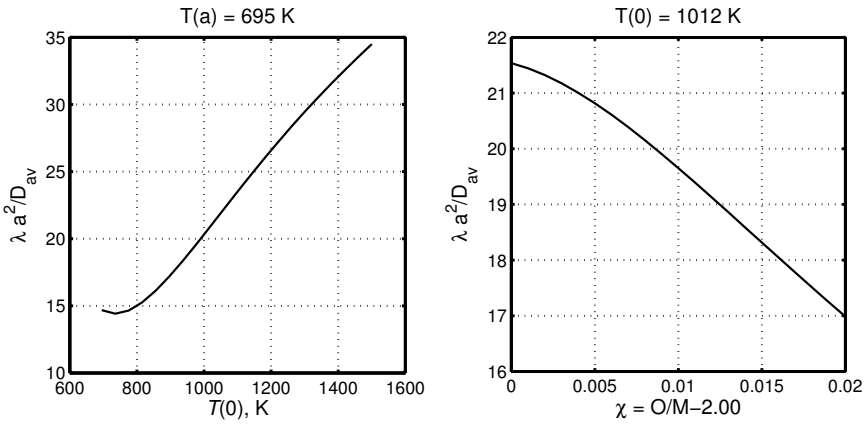

(a) (b)

Figure B.1: Inverse of the dimensionless time constant $\tilde{\tau}^{-1} \equiv \lambda_1 a^2/D_{\rm av}$ versus: (a) Central fuel temperature at a const. surface temperature 695 K. (b) oxygen concentration at a fixed central temperature 1012 K and $\overline{\chi}_0 = 0.0056$.

The imposed Neumann boundary condition on $\tilde{e}_k$ is

$$\frac{d\tilde{f}_k}{dr} = 0, \quad \text{at} \quad r = 0,\ r = a. \tag{B.10}$$

So the problem is to determine the eigenvalues $\tilde{\lambda}_k$ which depend on temperature and the heat of transport through equations (B.8) and (B.10). In particular, one is interested to determine the first nonzero eigenvalue which gives the principal contribution to the oxygen concentration.

In [57] the eigenvalue problem described by Eqs. (B.8) and (B.10) is solved numerically by discretizing Eq. (B.8) in terms of a tridiagonal matrix [97]. The first nonzero eigenvalue can be identified as the inverse of the time constant. In more detail, in the approximate solution given by Eq. (60), the normalized time constant or its inverse is $1/\tilde{\tau} = \lambda_1 a^2/D_{\rm av}$, where $D_{\rm av} \equiv D_x(T_{\rm av})$ and $T_{\rm av}$ is taken as the harmonic average of the center and outer pellet temperatures, i.e. $1/T_{\rm av} = \big(1/T(0) + 1/T(a)\big)/2$.

Figure B.1 depicts $\lambda_1 a^2/D_{\rm av}$ as a function of fuel central temperature at a fixed surface temperature of 695 K (Fig. B.1(a)) and the oxygen concentration $\chi = {\rm O/M} - 1$ at a fixed central temperature of 1012 K (Fig. B.1(b)). It is seen that the eigenvalue increases with the temperature while it decreases with the oxygen concentration. The trend for the time constant is opposite.

C UO_{2+x} fuel thermal conductivity

The thermal diffusivity of unirradiated oxidized UO_{2+x} fuel pellets has been determined experimentally by Amaya, Kubo and Korei or AKK [98] using a laser flash technique from 300 to 1400 K and $0.00 \leq x \leq 0.20$. The corresponding thermal conductivities were evaluated by multiplying the thermal diffusivities by the sample densities and the specific heat capacities derived from the literature. The thermal conductivity of UO_{2+x} decreases with increasing hyperstoichiometry. AKK expressed the thermal conductivity as a function of the hyperstoichiometry variable x using the concentration of U^{5+} formed with the excess interstitial oxygen atoms. In order to evaluate their data, they utilized as a base model Klemens's theory of heat conduction in materials when phonon-phonon (Umklapp process) scattering and phonon-impurity scattering occur simultaneously [99, 100].
Amaya and coworkers validated their model with additional data reported in the literature on unirradiated hyperstoichiometric fuel covering temperatures up to about 1700 K. Beyond this temperature the electronic heat transport becomes dominant, which they did not consider. Here, we add this contribution to the UO_{2+x} thermal conductivity and write $\kappa_{\rm th} \equiv \kappa$ as

$$\kappa = \kappa_{\rm ph} + \kappa_{\rm el}, \tag{C.1}$$

where $\kappa_{\rm ph}$ and $\kappa_{\rm el}$ denote the phonon and the electronic contributions to thermal conductivity, respectively. The phonon contribution to thermal conductivity (in W/m·K), as stated in [98], is expressed as

$$\kappa_{\rm ph} = \kappa_0 \frac{\arctan(\Theta)}{\Theta} + CT^3, \tag{C.2}$$

$$\kappa_0 = (A + BT)^{-1}, \tag{C.3}$$

$$\Theta = D_0 \exp(D_1 T)\sqrt{2x\kappa_0}. \tag{C.4}$$

Here, T is the temperature in kelvin and x is the deviation from the stoichiometry. The numerical values for the constants are listed in Table C.1.

Table C.1: Constants in relations (C.2)-(C.4).

Parameter	unit
$A = 3.24 \times 10^{-2}$	$\mathrm{m{\cdot}K{\cdot}W^{-1}}$
$B = 2.51 \times 10^{-4}$	$\mathrm{m{\cdot}W^{-1}}$
$C = 5.95 \times 10^{-11}$	$\mathrm{W{\cdot}m^{-1}{\cdot}K^{-4}}$
$D_0 = 3.67$	$\mathrm{m^{1/2}{\cdot}K^{1/2}{\cdot}W^{-1/2}}$
$D_1 = -4.73 \times 10^{-4}$	$\mathrm{K^{-1}}$

The values in Table C.1 are for the thermal conductivity of 96.5%TD UO_{2+x}. The Leob formula relates this thermal conductivity to that of a fuel with porosity p, namely

$$\kappa_{96.5} = \frac{1 - 0.035\beta}{1 - p\beta}\kappa_T. \tag{C.5}$$

Here, κ_T is the true thermal conductivity and $\beta = 2.6 - 5 \times 10^{-4}(T - 273.15)$; *cf.* [98].
In the standard treatment of the electronic contribution, UO_2 is considered as a Mott-Hubbard insulator for which the small polaron theory of semiconductors is used to describe

its electrical conductivity, and then the Wiedemann-Franz law (formula) is invoked to relate the electrical conductivity to the thermal conductivity [101, 102, 103, 104]. Hence, the electronic part of the thermal conductivity is [101]

$$\kappa_{\rm el} = C_\kappa \Big(\frac{U}{k_B T}\Big)^2 \frac{np(1-n-p)}{n+p} e^{-E_e/(k_B T)}, \tag{C.6}$$

where $C_\kappa = 2.83$ Wm^{-1}K^{-1}, U is the Mott-Hubbard energy gap $= 4.33 \times 10^{-19}$ J, E_e is the electron mobility activation energy $= 4.81 \times 10^{-20}$ J, and n and p are the molar concentrations of electrons and holes, respectively. They are functions of stoichiometric deviation and are determined from the conditions of electroneutrality and thermodynamic equilibrium, resulting in

$$p = x + \frac{-2K + \sqrt{x^2(1-4K)+K}}{1-4K}, \tag{C.7}$$

$$n = p - 2x, \tag{C.8}$$

where $K = \exp[-F/(k_B T)]$, $F = U - TS$ and $S = 2.62 \times 10^{-23}$ JK^{-1} [101, 103].
A more empirical phonon conductivity correlation (in W/mK) for a fully dense fuel, based on the assessment of measured data by Ellis, Porter and Shaw or EPS [105], over the stoichiometry range from $x = 0$ to $x = 0.2$ with a burnup dependent term, is given as

$$\kappa_{\rm ph} = \frac{1000}{A(x) + B(x)T + \eta(u,T)}, \tag{C.9}$$

where u the burnup (MWd/kgU) and T the temperature (K). The parameters $A(x)$ and $B(x)$ are given by

$$A(x) = 14 - 10.763\sqrt{x} - 2381.4x + 12819.86x^{3/2}, \tag{C.10}$$

$$B(x) = 0.2218 + 0.2562\sqrt{x} - 0.64x - 3.6764x^{3/2} + 17.3x^3. \tag{C.11}$$

Here, we wrote a slight modification of $B(x)$ due to Lewis, Szpunar and Iglesias [32] for ease of numerical implementation. The burnup dependent term is from Lanning, Beyer and Cunningham [106]

$$\eta(u,T) = 1.87u + \frac{38(1-0.9e^{-0.04u})u^{0.28}}{1+396e^{-6380/T}}. \tag{C.12}$$

The polaron thermal conductivity (in W/mK), based on the data analysis of Ronchi, Scheindlin and Musella [107], is given by (here independent of x)

$$\kappa_{\rm el} = \frac{2.024 \times 10^{11} e^{-16350/T}}{T^{5/2}}. \tag{C.13}$$

The photon contribution to thermal conductivity (in W/mK) is

$$\kappa_{\rm rad} = \frac{1.5 \times 10^{-7} n_r^2}{8750 e^{0.75971T/1000}} T^3, \tag{C.14}$$

where n_r is the index of refraction, taken to be independent of temperature and wavelength and is put equal to 2.25 [32]. As an example, at a fuel temperature of 1400 K, $\kappa_{\rm rad} = 0.08$

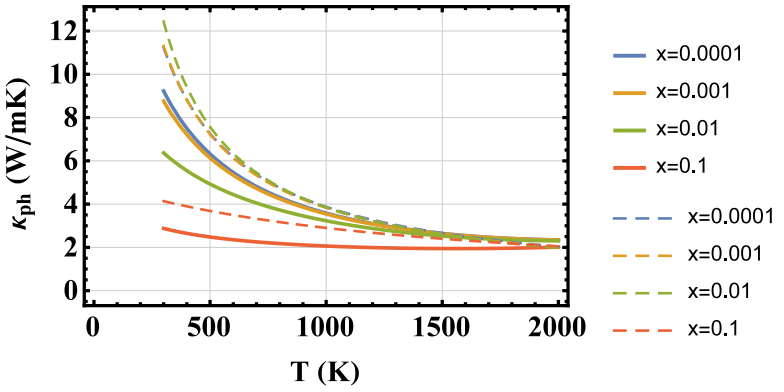

(a)

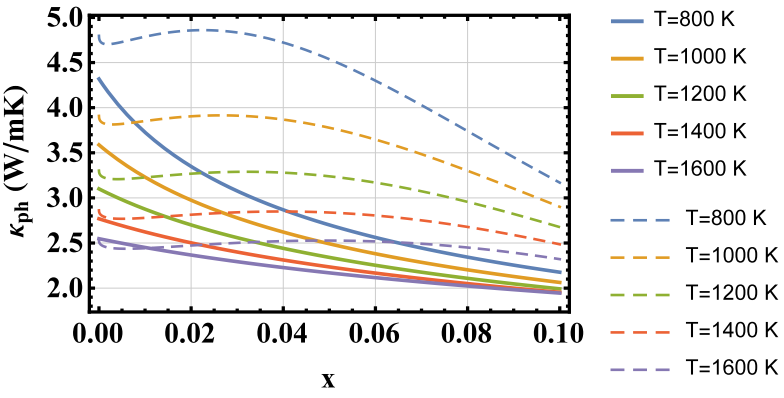

(b)

Figure C.1: Comparison between predictions of the two thermal conductivity (phonon component $\kappa_{\rm ph}$) relations, AKK (solid lines) vs. EPS (dashed) described in the text. (a) $\kappa_{\rm ph}$ versus temperature, (b) $\kappa_{\rm ph}$ vs. x =O/U-2.00. In these computations using Leob's formula (C.5), we have adjusted the EPS's 100%TD conductivity to AKK's 95.6%TD.

W/mK, which is much smaller than the combined contributions of the phonon and the polaron conductivities at this temperature, $\kappa_{\rm ph} + \kappa_{\rm el} \approx 3.5$ W/mK. Hence, the radiative fuel conductivity is neglected in computations.

Figure C.1(a) compares the plots of $\kappa_{\rm ph}$ as a function of temperature for several values of x for the two mentioned correlations, namely AKK versus EPS (with $u = 0$). It is seen that EPS predicts a higher thermal conductivity than AKK. Besides, EPS in not monotonically decreasing function of x as has been observed by AKK [98]; see Fig. C.1(b).

Finally, we should recall that $\kappa_{\rm th}$ enters the heat conduction equation in the fuel, Eq. (59), from which one calculates the radial fuel temperature profile for a prescribed surface temperature T_s .

References

[1] B.T.M. Willis. Crystallographic studies of anion-excess uranium dioxide. *J. Chem. Soc. Faraday Trans. 2*, 83:1073–1081, 1987.

[2] G. C. Allen and N. R. Holmes. A mechanism for the UO_2 to α-U_3O_8. *J. Nucl. Mater.*, 223:231–237, 1995.

[3] L. Desgranges, G. Baldinozzi, G. Rousseau, J.C. Nièpce, and G. Calvarin. Neutron diffraction study of the in situ oxidation of UO_2. *Inorg. Chem.*, 48:7585–7592, 2009.

[4] L. Desgranges, G. Baldinozzi, D. Siméone, and H. E. Fischer. Refinement of the α-U_4O_9 crystalline structure: New insight into the $U_4O_9 \rightarrow U_3O_8$ transformation. *Inorg. Chem.*, 50:6146–6151, 2011.

[5] D. E. Sands. *Introduction to Crystallography*. W. A. Benjamin, New York, 1975. Dover Reprint 1993.

[6] D. R. Olander, W. E. Wang, Y. S. Kim, C. Y. Li, S. Lim, and S. K. Yagnik. Chemical processes in defective LWR fuel rods. *J. Nucl. Mater.*, 248(1):214–219, 1997.

[7] D. R. Olander, Y. S. Kim, W. E. Wang, and S. K. Yagnik. Steam oxidation of fuel in defective LWR rods. *J. Nucl. Mater.*, 270:11–20, 1999.

[8] J. C. Clayton. Internal hydriding in irradiated defected Zircaloy fuel rods. In L. F. P. van Swam C. M. Euken, editor, *Zirconium in the Nuclear Industry: Eighth International Symposium*, ASTM STP 1023, pages 266–288, Philadelphia, 1989. American Society for Testing and Materials.

[9] G. Lysell, V. Grigoriev, and P. Efsing. Axial splits in failed BWR fuel rods. In *Proc. International Topical Meeting on LWR Fuel Performance*, Park City, Utah, April 10-13 2000. American Nuclear Society.

[10] H. Zimmermann. Fission gas release in LWR fuel during loss-of-coolant accidents. *Eur. Appl. Res. Rep. Nucl. Sci. Technol.*, 5:1349–1361, 1984.

[11] J. Y. Colle, J.-P. Hiernaut, D. Papaioannou, C. Ronchi, and A. Sasahara. Fission product release in high-burnup UO_2 oxidized to U_3O_8. *J. Nucl. Mater.*, 348:229–242, 2006.

[12] L. O. Jernkvist and A. R. Massih. Improving the FRAPTRAN program for fuel rod LOCA analyses by novel models and assessment of recent data. Technical Report TR17-006v1, Quantum Technologies AB, Uppsala, Sweden, 2017. To be published by IAEA within the reseach project FUMAC.

[13] D-J. Kim, J. H. Kim, K. S. Kim, et al. Thermodynamic assessment of UO_2 pellet oxidation in mixture atmospheres under spent fuel pool accident. *World J. Nucl. Sci. Tech.*, 5:102–106, 2015.

[14] D. S. Cox, F. C. Iglesias C. E. L. Hunt, N. A. Keller, R. D. Barrand, J. R. Mitchell, and R. F. O'Connor. Oxidation of UO_2 in air and steam with relevance to fission

product releases. In *Proc. Symp. Chemical Phenomena Associated with Radioactivity Releases During Severe Nuclear Plant Accidents*, NUREG/CP-0078, pages 2–35 to 2–49, Anaheim, California, September 9-12 1986. U.S. Nuclear Regulatory Commission.

[15] J. Abrefah, A. de Aguiar Braid, W. Wang, Y. Khalil, and D. R. Olander. High temperature oxidation of UO_2 in steam-hydrogen mixtures. *J. Nucl. Mater.*, 208:98–110, 1994.

[16] K. Une, M. Imamura, M. Amaya, and Y. Korei. Fuel oxidation and irradiation behaviors of defective BWR fuel rods. *J. Nucl. Mater.*, 223:40–50, 1995.

[17] M. Imamura and K. Une. High temperature steam oxidation of UO_2 fuel pellets. *J. Nucl. Mater.*, 247:131–137, 1997.

[18] T. J. Heames, D. A. Williams, N. E. Bixle, et al. VICTORIA: a mechanistic model of radionuclide behavior in the reactor coolant system under severe accident conditions. Technical Report NUREG/CR-5545 Rev. 1, U.S. Nuclear Regulatory Commission, 1992.

[19] R. E. Carter and K. W. Lay. Surface-controlled oxidation-reduction of UO_2. *J. Nucl. Mater.*, 36:77–86, 1970.

[20] D. R. Olander. Mechanistic interpretation of UO_2 oxidation. *J. Nucl. Mater.*, 252:121–130, 1998.

[21] D. R. Olander. Oxidation of UO_2 by high-pressure steam. *Nucl. Technol.*, 74:215–217, 1986.

[22] J. T. Bittel, L. H. Sjodahl, and J. F. White. Steam oxidation kinetics and oxygen diffusion in UO_2 at high temperatures. *J. Amer. Ceram. Soc.*, 52:446–451, 1969.

[23] B. J. Lewis, B. Andre, B. Morel, P. Dehaudt, et al. Modelling the release behviour of cesium during severe fuel degradation. *J. Nucl. Mater.*, 227:83–109, 1995.

[24] B. J. Lewis, D. S. Cox, and F. C. Iglesias. A kinetic model for fission-product release and fuel oxidation behaviour for Zircaloy-clad fuel elements under reactor accident conditions. *J. Nucl. Mater.*, 207:228–241, 1993.

[25] D. S. Cox, R.F. O'Connor, and W. W. Smeltzer. Measurement of oxidation/reduction kinetics to 2100°C using non-contact solid-state electrolytes. *Solid State Ionics*, 53-56:238–254, 1992.

[26] B. V. Dobrov, V. V. Likhanskii, V. D. Ozrin, A. A. Solodov, M. P. Kissane, and H. Manenc. Kinetics of UO_2 oxidation in steam atmosphere. *J. Nucl. Mater.*, 255:59–66, 1998.

[27] B. J. Lewis. Prediction of the oxygen potential in the fuel-to-clad gap of defective fuel rods during severe accident conditions. *J. Nucl. Mater.*, 270:221–232, 1999.

[28] O. Kubaschewski and C. B. Alcock. *Metallurgical Thermochemistry*. Pergamon Press, Oxford, UK, fifth edition, 1979.

[29] A. R. Massih. Gas transport in a defective fuel rod. Technical Report TN17-001, Quantum Technologies AB, Uppsala, Sweden, 2017.

[30] J. D. Higgs, B. J. Lewis, W. T. Thompson, and Z. He. A conceptual model for the fuel oxidation of defective fuel. *J. Nucl. Mater.*, 366:99–128, 2007.

[31] B. J. Lewis. Fuel oxidation behaviour in defective fuel rods. In *Proc. International Topical Meeting on LWR Fuel Performance*, Park City, Utah, April 10-13 2000. American Nuclear Society.

[32] B. J. Lewis, B. Szpunar, and F. C. Iglesias. Fuel oxidation and thermal conductivity model for operating defective fuel rods. *J. Nucl. Mater.*, 306:30–43, 2002.

[33] P. W. Atkins. *Physical Chemistry*. Oxford University Press, Oxford, UK, third edition, 1988.

[34] L. Desgranges, Y. Ma, Ph. Garcia, G. Baldinozzi, D. Siméone, and H. E. Fischer. What is the actual local crystalline structure of uranium dioxide UO_2? a new perspective for the most used nuclear fuel. *Inorg. Chem.*, 56:321–326, 2017.

[35] D. A. Andersson, G. Baldinozzi, L. Desgranges, D. R. Conradson, and S. D. Conradson. Density functional theory calculations of UO_2 oxidation: Evolution of UO_{2+x}, U_4O_{9-y}, U_3O_7, and U_3O_8. *Inorg. Chem.*, 52:2769–2778, 2013.

[36] G. Dolling, R. A. Cowley, and A. D. B. Woods. The crystal dynamics of uranium dioxide. *Can. J. Phys.*, 43:1397–1413, 1965.

[37] H. Blank and C. Ronchi. Electron diffraction of U_3O_8. *Acta Cryst. A*, 24:657–666, 1968.

[38] R. J. Ackermann, A. T. Chang, and C. A. Sorrell. Thermal expansion amd phase transformation of the U_3O_{8-z} phase in air. *J. Inorg. Nucl. Chem.*, 39:75–85, 1977.

[39] B. O. Loopstra. The phase transition in α-U_3O_8 at 210°C. *J. Appl. Cryst.*, 3:94–96, 1995.

[40] R. K. Edwards and A. E. Martin. The uranium-uranium dioxide phase diagram at high temperatures. *J. Phys. Chem.*, 69:1788, 1966.

[41] K. Naito and K. Kamegashira. High temperature chemistry of ceramic nuclear fuels with emphasis on nonstoichiometry. *Adv. Nucl. Sci. Technol.*, 9:99–180, 1976.

[42] Y. S. Kim. A thermodynamic evaluation of the U-O system from UO_2 to U_3O_8. *J. of Nucl. Mater.*, 279:173–180, 2000.

[43] P. Y. Chevalier, E. Fischer, and B. Cheynet. Progress in the thermodynamic modelling of the U-O binary system. *J. Nucl. Mater.*, 303:1–28, 2002.

[44] C. Gueneau, M. Baichi, D. Labroche, C. Chatillon, and B. Sundman. Thermodynamic assessment of the uranium-oxygen system. *J. Nucl. Mater.*, 304:161–175, 2002.

[45] W. T. Thompson, B. J. Lewis, F. Akbari, and D. M. Thompson. Part I: Thermodynamic modeling of uranium oxidation in support of fission product transfer from defective fuel. In *Proc. 2004 International Meeting on LWR Fuel Performance*, pages 823–832. American Nuclear Society, September 19-22 2004. Orlando, Forida.

[46] B. J. Lewis. Application of fission product release studies to fuel failure monitoring. In *Proc. International Topical Meeting on LWR Fuel Performance*, pages 165–179, Williamsburg, Virginia, April 17-20 1988. American Nuclear Society.

[47] B. J. Lewis, R. D. MacDonald, N. V. Ivanoff, and F. C. Iglesias. A review of fuel performance and fission product release studies for defected fuel elements. In *Fuel Failure in Normal Operation of Water Reactors: Experience, Mechanisms amd Management*, IAEA-TECDOC-709, pages 79–99, International Atomic Energy Agency, Vienna, Austria, 1993.

[48] D. R. Olander. *Fundamental Aspects of Nuclear Reactor Fuel Elements*. U.S. Department of Commerce, Springfield, Virginia, 1976.

[49] H. Kleykamp. The chemical state of LWR high-power rods under irradiation. *J. Nucl. Mater.*, 84:109–117, 1979.

[50] C. T. Walker and M. Mogensen. On the rate determining step in fission gas release from high burnup water reactor fuel during power transients. *J. Nucl. Mater.*, 149:121–131, 1987.

[51] J. Spino and P. Peerani. Oxygen stoichiometry shift of irradiated LWR-fuels at high burnups: Review of data and alternative interpretation of recently published results. *J. Nucl. Mater.*, 375:8–25, 2008.

[52] S. K. Evans, E. A. Aitken, and C. N. Craig. Effect of a temperature gradient on the stoichiometry of urania-plutonia fuel. *J. Nucl. Mater.*, 30:57–61, 1969.

[53] E. A. Aitken. Thermal diffusion in closed oxide fuel systems. *J. Nucl. Mater.*, 30:62–73, 1969.

[54] C. Sari and G. Schumacher. Oxygen redistribution in fast reactor fuel. *J. Nucl. Mater.*, 61:192–202, 1976.

[55] F. Ewart, K. Lassmann, Hj. Matzke, L. Manes, and A. Saunders. Oxygen potential measurements in irradiated mixed oxide fuel. *J. Nucl. Mater.*, 124:44–55, 1984.

[56] K. Lassmann. The OXIRED model for redistribution of oxygen in non-stoichiometric uranium-plutonium oxides. *J. Nucl. Mater.*, 150:10–16, 1987.

[57] K. Forsberg, F. Lindström, and A. R. Massih. Modelling of some high burnup phenomena in nuclear fuel. In *Water Reactor Fuel Element Modelling at High Burnup and Experimental Support*, IAEA-TECDOC-957, International Atomic Energy Agency, Vienna, Austria, 1994.

[58] J. C. Ramirez, M. Stan, and P. Cristea. Simulations of heat and oxygen diffusion in UO_2 nuclear fuel rods. *J. Nucl. Mater.*, 359:174–184, 2006.

[59] B. Mihaila, M. Stan, J. Ramirez, A. Zubelewicz, and P. Cristea. Simulations of coupled heat transport, oxygen diffusion, and thermal expansion in UO_2 nuclear fuel elements. *J. Nucl. Mater.*, 394:182–189, 2009.

[60] M. V. Ozrin. A model for evolution of oxygen potential and stoichiometry deviation in irradiated UO_2 fuel. *J. Nucl. Mater.*, 419:371–377, 2011.

[61] S. R. de Groot and P. Mazur. *Non-equilibrium Thermodynamics*. Dover Publications, New York, 1984.

[62] A. R. Allnatt and A. B. Lidiard. *Atomic Transport in Solids*. Cambridge University Press, Cambridge, 1993.

[63] A. B. Lidiard. Mass transfer along temperature gradient. In *Thermodynamics*, volume II, pages 3–22. International Atomic Energy Agency, Vienna, Austria, 1966. IAEA Symposium, Vienna, 22-27 July 1965.

[64] C. M. Bender and S. A. Orszag. *Advanced Mathematical Methods for Scientists and Engineers*. Springer, New York, 1999. chap. 8.

[65] J. A. Meachen. Oxygen diffusion in uranium dioxide: A review. *Nucl. Energy*, 28:221–226, 1989.

[66] H. Kleykamp. The chemical state of the fission products in oxide fuels. *J. Nucl. Mater.*, 131:221–246, 1985.

[67] K. Une, M. Amaya, M. Imamura, and Y. Korei. Fission gas release from defective BWR fuels. *J. Nucl. Mater.*, 226:323–326, 1995.

[68] P. Ruello, G. Chirlesan, G. Petot-Ervas, C. Petot, and L. Desgranges. Chemical diffusion in uranium dioxide - influence of defect interactions. *J. Nucl. Mater.*, 325:202–209, 2004.

[69] J. Wang, R. C. Ewing, and U. Becker. Average structure and local configuration of excess oxygen in UO_{2+x}. *Scientific Reports*, 4(4216):1–5, 2014.

[70] C. Berthinier, C. Rado, C. Chatillon, and F. Hodaj. Thermodynamic assessment of oxygen diffusion in non-stoichiometric $UO_{2\pm x}$ from experimental data and Frenkel pair modeling. *J. Nucl. Mater.*, 433:265–286, 2013.

[71] W. Miekeley and F. W. Felix. Effect of stoichiometry on diffusion of xenon in UO_2. *J. Nucl. Mater.*, 42:297–306, 1972.

[72] L.E. Thomas, R.E. Einsiger, and R.E. Woodley. Microstructural examination of oxidized spent PWR fuel by transmission electron microscopy. *J. Nucl. Mater.*, 166:243–251, 1989.

[73] M. Magnuson, S. M. Butorin, L. Werme, J. Nordgren, et al. Uranium oxides investigated by x-ray absorption and emission spectroscopies. *Applied Surface Science*, 252:5615–5618, 2006.

[74] R.J.M. Konings, T. Wiss, and O. Benes. Predicting material release during a nuclear reactor accident (commentary). *Nature Materials*, 14:247–252, 2015.

[75] J.-P. Hiernaut, T. Wiss, D. Papaioannou, R.J.M. Konings, and V.V. Rondinella. Volatile fission product behaviour during thermal annealing of irradiated UO_2 fuel oxidised up to U_3O_8. *J. Nucl. Mater.*, 372:215–225, 2008.

[76] V. V. Rondinella, , and T. Wiss. The high burnup structure in nuclear fuel. *Materials Today*, 13:24–32, 2010.

[77] L. O. Jernkvist and A. R. Massih. Fission gas release under loss-of-coolant accident conditions: Data and models. Memo PM16-003v1, Quantum Technologies AB, Uppsala, Sweden, 2016. cf. refs. therein.

[78] K. Forsberg and A. R. Massih. Diffusion theory of fission gas migration in irradiated nuclear fuel. *J. Nucl. Mater.*, 135:140–148, 1985.

[79] P. Hermansson and A. R. Massih. An effective method for calculation of diffusive flow in spherical grains. *J. Nucl. Mater.*, 304:204–211, 2002.

[80] M. V. Speight. A calculation on the migration of fission gas in material exhibiting precipitation and re-solution of gas atoms under irradiation. *Nucl. Sci. Eng.*, 37:180–185, 1969.

[81] H. S. Carslaw and J.C. Jaeger. *Conduction of Heat in Solids*. Oxford University Press, Oxford, UK, 2nd edition, 1959.

[82] A. H. Booth. A method of calculating gas diffusion from UO_2 fuel and its application to the X-2-f test. Technical Report AECL 496 CRDC-721, Atomic Energy of Canada Limited, 1957.

[83] R. Lindner and Hj. Matzke. Diffusion von Xe-133 in Uranoxyd verschiedenen Sauerstoffgehaltes. *Z. Naturforschung A*, 14:582–584, 1959.

[84] H. Matzke. Atomic transport properties in UO_2 and mixed oxides $(U,Pu)O_2$. *J. Chem. Soc. Faraday Trans.*, 83:1121–1142, 1987.

[85] H. Matzke. Atomic mechanisms of mass transport in ceramic nuclear fuel. *J. Chem. Soc. Faraday Trans.*, 86:1243–1256, 1990.

[86] H. Matzke. In R. P. Agarwala, editor, *Diffusion Processes in Nuclear Fuel*, chapter 2, pages 9–69. North-Holland, Amsterdam, 1992.

[87] Y. S. Kim. Fission gas release from UO_{2+x} in defective light water reactor fuel rods. In *Proc. International Topical Meeting on LWR Fuel Performance*, Park City, Utah, April 10-13 2000. American Nuclear Society. cf. *Nucl. Tech.*, 130:9-17, 2000.

[88] K. Shiba. Fission iodine and xenon release from the UO_2-U_3O_8 system with emphasis on radiation damage. *J. Nucl. Mater.*, 57:271–279, 1975.

[89] R. G. Ball and R. W. Grimes. A comparison of the behaviour of fission gases in $UO_{2\pm x}$ and $\alpha-U_3O_{8-z}$. *J. Nucl. Mater.*, 188:216–221, 1992.

[90] J. C. Killeen and J. A. Turnbull. An experimental and theoretical treatment of the release of ^{85}Kr from hyperstoichiometric uranium dioxide. In *Proc. Workshop on Chemical Reactivity of Oxide Fuel and Fission Product Release*, volume 2, pages 387–404, Berkeley Nuclear Laboratories, Gloucestershire, UK, April 7-9 1987. Central Electricity Generating Board.

[91] D. Davies and G. Long. The emission of xenon-133 from lightly irradiated uranium dioxide spheroids and powders. Technical Report AERE-R-4347, AERE Harwell, Didcot, U.K., 1963.

[92] H. Matzke. Diffusion processes and surface effects in non-stoichiometric nuclear fuel UO_{2+x} and (U,Pu)$O_{2\pm x}$. *J. Nucl. Mater.*, 114:121–135, 1983.

[93] D. A. Andersson, B. P. Uberuaga, P. V. Nerikar, C. Unal, and C. R. Stanek. U and Xe transport in $UO_{2\pm x}$: Density functional theory calculations. *Phys. Rev. B*, 84:054105, 2011.

[94] S. Kashibe and K. Une. Effect of additives (Cr_2O_3, Al_2O_3, SiO_2, MgO) on diffusion release of Xe-133 from UO_2 fuel. *J. Nucl. Mater.*, 254:234–242, 1998.

[95] P. E. Blackburn. Oxygen pressures over fast breeder reactor fuel: (I) a model for UO_{2+x}. *J. Nucl. Mater.*, 46:244–252, 1973.

[96] T. B. Lindemer and T. M. Besmann. Chemical thermodynamic representation of UO_{2+x}. *J. Nucl. Mater.*, 130:473–488, 1985.

[97] J. Stoer and R. Bulirsch. *Introduction to Numerical Analysis*, volume 12 of *Texts in Applied Mathematics*. Springer, New York, third edition, 2013.

[98] M. Amaya, T. Kubo, and Y. Korei. Thermal conductivity measurements on UO_{2+x} from 300 to 1400 K. *J. Nucl. Sci. Technol.*, 33:636–640, 1996.

[99] P. G. Klemens. The scattering of low-frequency lattice waves by static imperfections. *Proc. Phys. Soc. A*, 68:1113–1129, 1955.

[100] P. G. Klemens. Thermal resistance due to point defects at high temperatures. *Phys. Rev.*, 119:507–509, 1960.

[101] P. W. Winter. The electronic transport properties of UO_2. *J. Nucl. Mater.*, 161:38–43, 1989.

[102] J. M. Casado, J. H. Harding, and G. J. Hyland. Small-polaron hopping in Mott-insulating UO_2. *J. Phys.: Condens. Matter*, 6:4685–4698, 1994.

[103] P. J. Reid, M. J. Richards, F. C. Iglesias, and A. C. Brito. In *Proc. 5th International Conference on CANDU Fuel*, volume 1, pages 321–341. Canadian Nuclear Society, September 21-25 1997.

[104] A. R. Massih. Electronic transport in pure and doped UO_2. *J. Nucl. Mater.*, 497:166–182, 2017.

[105] W. E. Ellis, J. D. Porter, and T. L. Shaw. The effect of oxidation, burnup, and poisoning on the thermal conductivity of UO_2 fuel: a comparison of data with theory. In *Proc. International Topical Meeting on LWR Fuel Performance*, Park City, Utah, April 10-13 2000. American Nuclear Society.

[106] D. D. Lanning, C. E. Beyer, and M. E. Cunningham. FRAPCON-3 fuel rod temperature predictions with fuel conductiviy degradation caused by fission products and gadolinia additions. In *Proc. International Topical Meeting on LWR Fuel Performance*, Park City, Utah, April 10-13 2000. American Nuclear Society.

[107] C. Ronchi, M. Scheindlin, and M. Musella. The thermal conductivity of uranium oxide up to 2900 K from simulataneous measurement of the heat capacity and thermal diffusivity. *J. Appl. Phys.*, 85:776–789, 1999.

2018:25

The Swedish Radiation Safety Authority has a comprehensive responsibility to ensure that society is safe from the effects of radiation. The Authority works to achieve radiation safety in a number of areas: nuclear power, medical care as well as commercial products and services. The Authority also works to achieve protection from natural radiation and to increase the level of radiation safety internationally.

The Swedish Radiation Safety Authority works proactively and preventively to protect people and the environment from the harmful effects of radiation, now and in the future. The Authority issues regulations and supervises compliance, while also supporting research, providing training and information, and issuing advice. Often, activities involving radiation require licences issued by the Authority. The Swedish Radiation Safety Authority maintains emergency preparedness around the clock with the aim of limiting the aftermath of radiation accidents and the unintentional spreading of radioactive substances. The Authority participates in international co-operation in order to promote radiation safety and finances projects aiming to raise the level of radiation safety in certain Eastern European countries.

The Authority reports to the Ministry of the Environment and has around 300 employees with competencies in the fields of engineering, natural and behavioural sciences, law, economics and communications. We have received quality, environmental and working environment certification.

Strålsäkerhetsmyndigheten
Swedish Radiation Safety Authority

SE-171 16 Stockholm
Solna strandväg 96

Tel: +46 8 799 40 00
Fax: +46 8 799 40 10

E-mail: registrator@ssm.se
Web: stralsakerhetsmyndigheten.se

Ale Tryckteam AB, Bohus, 2018